DESIGN OPTIONS FOR ULTRA-COMPACT NUCLEAR DRIVEN POWER SOURCES FOR FIELD APPLICATIONS

A Thesis

by

DEAN AARON MATHIS

Submitted to the Office of Graduate and Professional Studies of
Texas A&M University
in partial fulfillment of the requirements for the degree of

MASTER OF SCIENCE

Chair of Committee,	Pavel V. Tsvetkov
Committee Members,	William S. Charlton
	Richard R. Schultz
	Roger E. Smith
Head of Department,	Yassin Hassan

May 2014

Major Subject: Nuclear Engineering

ABSTRACT

In the future, there will be demand for transportable power generation systems that can provide electricity and heating to remote, austere regions, for industrial, scientific, and military purposes. This thesis proposes that such a system should be compact, able to discharge its waste heat into the environment without a local water source, and have low logistical overhead. An air-cooled fast-spectrum nuclear reactor coupled to a direct Brayton cycle would be a viable and suitable design concept to fill this role. In order to support this claim, this thesis presents neutronics, thermal hydraulics, and thermodynamics of such a system.

As modeled in this thesis, a fast spectrum core 50 cm tall, with air as the working fluid, is able to drive a closed Brayton cycle core with a thermal efficiency of 37.5%, while the same core is unable to drive an open Brayton cycle with more than approximately 10% efficiency. This core could reach a burnup of 39 $\frac{GWd}{tHM}$, while remaining critical, controllable, and neutronically safe throughout the core lifetime.

Assuming heat is only removed via active cooling, this reactor would require 24 kW of pumping power in the first minutes of a Depressurization Loss of Coolant Accident scenario.

For both the open and closed Brayton cycle models, Argon-41 production is significant. However, in an open cycle mode, Argon-41 is unlikely to provide a harmful dose. In a closed cycle mode, Argon-41 may require some shielding of the primary coolant loop.

ACKNOWLEDGEMENTS

I thank my committee chair, Dr. Tsvetkov, and my committee members, Dr. Charlton and Dr. Smith, for their instruction, support, and mentorship throughout the course of this research.

Thanks also to my professors for providing me with the education to begin performing this research, as well as my research group and classmates who have helped me understand some of the fine points of nuclear engineering. I also want to extend my gratitude to US Army, which funded my attendance at Texas A&M University.

NOMENCLATURE

A_{Ar41}	Activity of Argon-41
a_{Ar41}	Specific Activity of Argon-41
A_{ch}	Cross Sectional Area of a Coolant Channel
$A_{ch,tot}$	Cross Sectional area of All Coolant Channels
A_{core}	Active Core Cross Sectional Area
AGFR	Air-Cooled Gas Fast Reactor
α_F	Fuel Temperature Coefficient of Reactivity
α_b	Bulk Coolant Temperature Coefficient of Reactivity
α_{void}	Void Coefficient of Reactivity
BOL	Beginning of Life
β_{eff}	Effective Delayed Neutron Fraction
CO_2	Carbon dioxide
c_p	Specific Heat at Constant Pressure
D_{ch}	Effective Coolant Channel Diameter
DLOCA	Depressurization Loss-of-Coolant Accident
$\Delta P_{friction}$	Pressure Drop Across Fuel Rods Due to Friction
ΔP_{pump}	Pressure Drop Across Heat Exchanger Pump
Δt	Time Step Size
ΔT_{hs}	Temperature Change of Heat Sink Air in Heat Exchanger
EOL	End of Life

ξ_{Recup}	Recuperator Efficiency
f_{DW}	Darcy-Weisbach Friction Factor
f_{ff}	Fast Flux Fraction
F_q	Power Peaking Factor
$F_{\emptyset}$	Flux Peaking Factor
Φ	Fluence
$\emptyset$	Scalar Flux
G	Mass Flux of Coolant
GFR	Gas-Cooled Fast Reactor
GT-MHR	Gas Turbine-Modular High Temperature Reactor
γ	Ratio of Specific Heat at Constant Pressure to Constant Volume
H	Active Core Height
h_b	Bulk Convective Heat Transfer Coefficient
HEU	Highly Enriched Uranium
HLW	High Level Waste
HTR	High Temperature Reactor
k_b	Thermal Conductivity of the Bulk
k_c	Thermal Conductivity of Fuel Element Cladding
k_{eff}	Effective Neutron Multiplication Factor
k_f	Thermal Conductivity of Fuel
k_g	Thermal Conductivity of Fuel Element Gap
k_{inf}	Effective Neutron Multiplication Factor in an Infinite Medium

LOCA	Loss-of-Coolant Accident
l_p	Prompt Neutron Lifetime
LMFR	Liquid Metal Fast Reactor
LWR	Light Water Reactor
Λ	Mean Generation Time
λ_{Ar41}	Decay Constant for Argon-41
MA	Minor Actinides
MCNP	Monte Carlo N-Particle Transport Code
μ	Dynamic Viscosity
N_{Ar40}	Number Density of Argon-40 in Air
N_{fe}	Number of Fuel Elements
N_{rings}	Number of Rings Beyond the Center in a Hexagonal Lattice
η_x	Isentropic Efficiency of Component 'X'
P	Pressure
p	Pitch between Fuel Elements
PD	Power Density
P_{fric}	Pumping Power Needed to Overcome Friction
P_{hs}	Power Required by Heat Exchanger
p_{sa}	Pitch between Sub-Assemblies
p/d	Pitch-to-Diameter Ratio
Pr	Prandtl Number
P_w	Wetted Perimeter of a Fuel Rod

$P_{w,tot}$	Wetted Perimeter of all Fuel Rods
PWR	Pressurized Water Reactor
Q	Thermal Power Production in Core
Q_{out}	Rate of Heat Removal by Heat Exchanger
q'_{avg}	Average Linear Heat Production Rate in Core
q'_{max}	Maximum Linear Heat Production Rate in Core
R_{Ar41}	Production Rate of Argon-41
r_f	Radius of Fuel in a Fuel Element
r_{ci}	Radius to the Inside of the Fuel Element Cladding
r_{co}	Radius to the Outside of the Fuel Element Cladding
r_c	Compression Ratio
Re	Reynolds Number
R_{spec}	Specific Ideal Gas Constant
ρ	Reactivity
ρ_{amb}	Density of Ambient Air
ρ_b	Density of Bulk Fluid
s	Entropy
SFR	Sodium-Cooled Fast Reactor
SCRAM	Safety-Control-Rod-Ax-Man (rapid shut-down of a reactor via dropping control rods into the reactor)
SMR	Small Modular Reactor
$\sigma_{\gamma,Ar40}$	Neutron Capture Cross Section for Argon-40

t	Time
T_b	Temperature of the Bulk Fluid
T_{ci}	Temperature at the Inside of the Fuel Element Cladding
T_{co}	Temperature at the Outside of the Fuel Element Cladding
T_{fo}	Temperature at the Outside of the Fuel
T_f	Temperature at the Centerline of the Fuel
TRU	Transuranic
UOX	Uranium Oxide
v	Velocity
v_{sound}	Speed of Sound
V_f	Volume of Fuel in One Fuel Element
V_{core}	Active Core Volume
$V_{f,core}$	Total Volume of Fuel in the Core
V_{fe}	Volume of a Fuel Element
VHTR	Very High Temperature Reactor
w	Mass Flow Rate
Z	Compressibility Factor
z	Axial Position
ζ	Gross Thermodynamic Cycle Efficiency
ζ_{net}	Net Thermodynamic Cycle Efficiency

TABLE OF CONTENTS

Page

LIST OF FIGURES

Page

LIST OF TABLES

1. INTRODUCTION

1.1 Status of Deployable SMRs

Small modular reactors (SMR) are desirable for a variety of reasons. If transportable, then they could be used to bring power to remote and austere locations far removed from any electrical grid or fuel source. This application could support scientific, industrial, civil, or military purposes.

International Atomic Energy Agency (IAEA) member states have already designed, built, and operated a significant number of SMRs for a diverse range of purposes. There are over 131 reactors in operation or under construction which fit the description of a SMR[1]. While a SMR is defined as a reactor that produces less than 300 MWe[1], SMRs with a power rating of tens of MW are of greatest interest in this study.

One of the prominent advantages of SMRs is their potential to provide reliable power to remote locations where there may be little or no supporting infrastructure. From the earliest years of the nuclear industry, SMRs have provided propulsion and electrical power for ships as they traversed the oceans. It was easier to advance SMR technology on maritime vessels, because large ships could support large SMRs, they would always have a supply of water, and water does not restrict the travel of ships in the same way terrain restricts land vehicles. Future generations of SMRs, however, will attempt to bring these benefits onto dry land, where routes are far narrower than the ocean, vehicles are much smaller than ships, and where there are unmet energy needs.

Deployment of SMRs to remote, land-based locations will require both logistical and technical developments. One precursor to land-transportable SMRs would logically be the deployment of smaller stationary reactors to power remote, but inhabited locations that demand less power than those areas served by large commercial power plants. If a SMR is to be made truly ground-transportable for deployments to temporary austere environments, it should be able to fit on a truck, or a convoy of trucks, or travel by rail or air, and be operable without continuous logistical support. It should rely on the surrounding environmental resources, or be fully self-contained. The thermal footprint may also need to be minimized, especially if the reactor is for military use.

The ground deployable SMR must be able to reject the heat it produces. Power stations typically reject their waste-heat ultimately into a combination of the atmosphere and a nearby water source. For a transportable reactor to be useful in an unpredictably austere and remote environment, it should be designed to reject its heat entirely without the aid of a water source. This requirement leads to the need for reactor designs that are cooled either directly and solely by air, or indirectly by heat exchange with a reliable closed-loop of primary coolant. For military applications, it may even be important to limit the observable heat signature of the reactor. Examples of indirect heat exchange with the atmosphere are designs that employ a gas such as helium as the primary coolant and working fluid in a closed, direct Brayton cycle, or that employ heat pipes to convect and conduct heat to the working fluid and heat sink[2]. In some scenarios, it may be best to minimize the need for any fluid other than air, if for no other reason than that air can be found everywhere on the earth, alleviating the logistical burden of maintaining liquid or gas coolant inventories.

The current state-of-the-art features mainly the stationary SMRs, most of them liquid-cooled, with power ratings ranging from 10 to 300 MWe[1]. It is not necessary that SMRs compete directly with large commercial plants, since a SMR could provide power to locations not serviced by larger power stations, but it is notable that larger plants have the advantage of the economy of scale. Capital investment in a small scale reactor is typically greater, per unit power rating, than capital investment in a larger reactor[3]. The inclusion of heat pipes or gas-cooling in a SMR design further compounds the lack of economy of scale, because such reactors must typically be operated at lower power densities than a liquid-cooled reactor[2].

1.2 Thesis Objectives

In order to support the design of an air-cooled SMR, it will be necessary to develop this concept through design and analysis efforts. By assuming a combination of reference parameters based on reference designs, and then analyzing and adjusting the model iteratively, it is possible to meet performance objectives and confirm its feasibility.

The overall objective of this thesis is to evaluate the feasibility of a concept for a SMR that is transportable and suitable for deployment in remote and austere environments. The thesis will first survey design options, assessing how each might allow for a compact reactor design with low logistical overhead, focusing on items such as the elimination of multiple coolant loops, and the need to resupply the coolant itself.

This survey will support the selection of one design concept (e.g.: an air-cooled GFR with a Brayton cycle) over others. It is necessary to develop and analyze the design concept to demonstrate its feasibility quantitatively. Among the goals for the selection, development, and analysis of this SMR design concept are the following:

- Survey several aspects of previous work on the subject of deployable SMRs and justify the selection of specific design features for a recommended concept.
- Select a suitable fuel that can achieve a reasonable burnup without producing excessive amounts of High Level Waste (HLW).
- Select materials that resist corrosion in the presence of air as needed. Comment also on their long term durability when exposed to a neutron flux, as well as their impact on reactor core performance.
- Design a viable configuration that is compact, coolable, controllable, and operable for the desired period of time at a power level of interest.
- Analyze the performance (power density, burnup, thermal efficiency, safety, etc.) of the reactor.
- Assess the feasibility of the use of air as a primary coolant.
- Assess the transportability of the modular system.

1.3 Thesis Overview

This thesis briefly discusses the history and status of deployable nuclear reactors, positing that deployable reactors may eventually compete to occupy a yet unfilled economic niche by providing temporary power to remote, austere, land-based outposts. Examples of the terrain where power may be needed are desert, tundra, or ice cap, and the purposes may be for scientific, industrial, or military expeditions. The ideal reactor for such a purpose would need little logistical support, would be transportable, and would not need access to local water sources. This means the atmosphere must be the only ultimate heat sink. While a myriad of self-contained reactor designs may be proposed, these all contain a coolant which must be recycled and maintained throughout the lifetime of the reactor. Minor losses of the coolant must be replaced, adding to logistical overhead. Major losses of the irreplaceable coolant could result in core damage due to overheating, as well as various problems with air-ingress. Therefore, it is proposed in this thesis that a viable design option may be to cool the reactor directly with air.

Next, this thesis proposes that a fast-spectrum reactor would couple well with an air-cooling regime. To support this proposal, a series of simulations are performed, in order to compose a design concept that supports the claim that a fast spectrum system can provide sufficient power for a sufficient length of time, and that it can be cooled using only air. Additionally, these simulations support the claims that the reactor can be controlled during normal operations, that workers could operate the reactor without accumulating an unsafe radiation dose, and that the reactor's decay heat can be removed in the event of an emergency. Finally, the transportability of the reactor is assessed.

Neutronics, thermal hydraulics, and thermodynamics are the three main aspects into which this design and analysis are divided. This is in order to make use of computational methods and tools that are suited to these aspects separately. The Monte Carlo N-Particle transport code (MCNP) is used to design and analyze a critical, controllable, compact core. Microsoft Excel is used to automate calculations using Fourier's law of conduction[2] and the Gnielinski heat transfer correlation[4], in order to ensure that all material temperatures are kept within their safe operating limits. Microsoft Excel is also used to optimize the efficiency of the reactor system. These neutronic, thermal hydraulic, and thermodynamic calculations are coupled with each other and/or iterated upon in order to optimize or identify acceptable design parameters.

2. CONCEPT SELECTION

2.1 Introduction

In this section, several existing reactor designs and concepts are introduced and evaluated with respect to the possibility that they could be adapted for the purpose of deploying to remote locations. Features conducive to transportability, logistical self-sufficiency, or atmospheric-only heat deposition are of particular interest in each concept considered. Qualitative comparison of these features among the designs will help identify a narrower range of designs to be discussed quantitatively in this thesis.

2.2 Survey of Deployable SMR Concepts

A distinct transportability advantage of a miniature Boiling Water Reactor (BWR) over a miniature Pressurized Water Reactor (PWR) is the elimination of the large heat exchanger between the primary and secondary loop of a PWR. However, Light Water Reactors in general are designed to operate at a power density high enough that they must ultimately consume water for cooling, even if their primary and/or secondary loops are well sealed and self-contained[2].

The use of heat pipes to cool a SMR is possible, and has advantages. From logistical and environmental perspectives, it makes the core a more self-contained system, reducing the necessity of replacing lost primary coolant as well as the likelihood of ventilation of fission products and neutron activation products with the coolant[5]. But the nearly isothermal removal of heat by the primary coolant hinders achieving efficient power extraction. Because heat-pipe designs typically reject heat ultimately to an ambient gas, the performance of such a reactor has limitations similar to those of a gas-cooled reactor, since its low thermal inertia (relative to a liquid-cooled reactor) necessitates a low power density[6]. One serious detractor of the heat-pipe design is the little-studied possibility of a heat-pipe failure cascade, whereby the burden of a single failed heat pipe is placed upon the surrounding heat pipes, possibly leading to additional heat pipe failures. Furthermore, even barring the outright failure of a heat pipe, the mechanism by which the working fluid transfers heat requires the continuous cycling of the fluid between its liquid and vapor phases, restricting the operation of the reactor to a narrow range of power modes, lest the working fluid completely vaporize[6]. The natural circulation inherent in heat pipes may therefore be seen as a constraint on the cooling modes for the reactor's operation, making a forced-convection, gas-cooled regime more desirable for its flexibility.

The Gas-cooled Fast Reactor (GFR) has features that may enable it to be adapted for a small, transportable design. Because the primary coolant is a gas instead of a liquid, its power density is not so great that its ultimate heat sink must be a liquid. Helium is the typical primary coolant of choice for a GFR design[2]. Replacing the helium with air would clearly provide the benefit of eliminating the need for helium storage and resupply. Also, in the event of a depressurization-loss-of-coolant-accident (DLOCA), assuming that the system can indeed be designed to use air as its coolant, there would be no complications resulting from inability to maintain helium circulation, even at atmospheric pressure. There would also be no complications from an air-ingress, since the GFR, unlike the High Temperature Reactor, would not contain graphite[2].

The problems created by replacing the helium in the reactor core with air stem from air's relative deficiencies in heat capacity, thermal conductivity, chemical inertia, and neutron transparency. The low heat capacity and thermal conductivity are not technically prohibitive, but may be uneconomical. The chemical reactivity of the oxygen component of air, especially at high temperatures, necessitates that the fuel cladding and other structures in the core be oxidation resistant in addition to neutron-transparent. This obstacle can likely be overcome, since the nuclear industry already routinely subjects metals to highly corrosive environments in LWRs[7], and the development of superalloys is an ongoing interest of many more industries. While hot air corrodes Zircaloy (the typical LWR cladding) faster than hot water[8], the corrosion resistant properties of Inconel[9] and silicon carbide[10] appear promising, even in air. Finally, although the argon in the air would capture neutrons, forming the gamma-emitting Ar-41, the half-life of Ar-41 is short enough, and the amounts produced are small enough, that it would decay away within hours after shutdown. The worst case scenario for the Ar-41 problem is that it may prohibit open-cycle operation of the reactor, and possibly even require the shielding of the whole primary loop in the closed-cycle case.

A typical Light Water Reactor (LWR) has a core power density of about 100 MWth/m^3, while a power density of approximately 350 MWth/m^3 is expected in a Sodium-Cooled Fast Reactor (SFR)[3,2]. The proposed 2400 MWth, helium-cooled, French CEA reactor[11] is designed to operate near 100 MWth/m^3, while another proposed GFR design[12] calls for a core power density of over 250 MWth/m^3. Studies by the

Generation IV International Forum (GIF) have concluded that a GFR could not achieve a reasonable degree of cost effectiveness if it were subject to the constraint that it be fully passively safe, because this would necessitate such a low power density that it would prohibit the recovery of the high cost of fuel fabrication for a fast reactor[3,13]. Complete passive safety requires that the reactor be capable of dissipating its decay heat during a Loss-of-Coolant Accident (LOCA), without relying on forced convection[14]. However, several alternative quasi-passive and highly reliable active safety measures have been proposed that may sufficiently mitigate the risk incurred by designing a GFR not subject to such a rigorous passive safety constraint[15]. While this thesis does not fully investigate all possible engineered safety systems that could be included in a GFR design, this thesis does demonstrate the degree to which active cooling is necessary under simulated accident conditions.

Helium is the typical coolant choice for GFR designs[2], however, for a small, deployable GFR, the advantages of air for use in a GFR begin to become evident. Air has many of the same advantages of helium, compared to liquid coolants. Air, like helium, does not have a violent chemical reaction in the event of a leak (unlike sodium, which reacts with air and water)[16]. Air and helium are optically transparent, enabling easier inspection and repairs[16]. Air and helium also remove the complexities of two-phase flow. While air's neutron transparency is not as desirable as helium's, it is still far better than sodium (as evidenced by void coefficients in Table 1), the activation of which has a fission-spectrum average cross section of 225.8 μb and results in the emission of two gamma rays: 2.754 MeV and 1.393 MeV, with a half-life of 14.959 hours[17]. The trace argon (0.933% by volume[18]) in the air activates with a microscopic cross section of 1.013 mb and usually emits a 1.294 MeV gamma ray with a 109.34 minute half-life[17]. Therefore, even at air pressures up to 17 MPa, the argon concentration is so small that the activity of sodium-24 may be expected to be roughly 300 times that of argon-41 during normal reactor operation.

Table 1. Properties of Coolants at Atmospheric Pressure[17,19]

	Helium Properties (273K)	**Air Properties (273K)**	**Sodium Properties (723K)**
Thermal conductivity [W/m K]	0.149	0.0257	66.1
Density [g/cm^3]	0.00018	0.00128	0.842
Specific heat capacity [J/kg K]	5188	1005	1272
Heat capacity per unit volume [J/cm^3 K]	0.000934	0.001286	1.07
Dynamic viscosity [kg/m s]	2.00E-05	1.18047E-05	3.46E-05
Prandtl number	0.69638	0.46162	0.00067
Reynolds number relative to Helium (for a given channel diameter and velocity)	1	12	2704
Radiative capture (n,γ) cross section of interest*, σ_γ [b] (fission spectrum average)	N/A	1.01E-03	2.26E-04
Half-life**	7.6E-23 [s]	1.822 [hr]	14.9590 [hr]
% yield of γ decay mode**	N/A	99.16%	100%
decay γ energy** [MeV]	N/A	1.294	2.754, 1.393

* Cross sections for He-4, Ar-40, and Na-23, respectively.

** Data for He-5, Ar-41, and Na-24, respectively. He-5 exists only insofar as He-4 accepts and quickly re-emits a neutron.

Because the activation of nuclei in the air is not as serious a problem as activation of sodium, air may be able to imitate another benefit of helium, which is the possibility of operating the reactor in a direct cycle, as opposed to the two, or even three loops characteristic of a SFR[20]. Furthermore, the lower void coefficient for gas coolants, which was cited as evidence of a lower rate of neutron capture, is also a significant safety benefit, in and of itself[16]. For the same reasons there is less radiative neutron capture in gasses than in sodium (i.e.: the gasses' relatively low density), gasses can allow the design of a reactor with a far smaller void coefficient than that of a SFR. As indicated by the data above, helium has advantages over air in its ability to accept and transfer heat, and its light weight enables it to be circulated with minimal pumping power; however, it is worth observing that air's heat transfer capabilities per unit volume are more comparable to those of helium than its capabilities per unit mass. This means that a given volume of air has a more similar heat capacity to the same volume of helium than a given mass of air has to the same mass of helium. This is important, because a reactor is typically characterized by a fixed volume of coolant space, while the mass of coolant within the reactor varies with pressure. Therefore, one focus of the research proposed here is to investigate the merits of air in terms of pumping power and cost, as well as heat transfer.

2.3 Selection of Air as Primary Coolant

A gas-cooled regime has several of the same drawbacks as heat-pipe cooling. In addition to limiting the performance and efficiency of the reactor during normal operations, the low thermal inertia of a gas-cooled reactor raises the question of how to ensure the safe dissipation of decay heat during an accident scenario. Helium's high specific heat and thermal conductivity are often touted as making it a good coolant choice[2]; however, as shown in Table 1, the higher density of air goes a long way toward making its cooling capability competitive with that of helium. By no means does this study purport to challenge the economic dynamics that make helium the leading gas coolant choice; however, it will establish that there exists a niche for a deployable air-cooled fast reactor (intermediate spectrum), and that it is possible to design a safe and economically viable reactor to occupy this niche, even if it is not economically competitive for general power production.

One of the greatest advantages of air over helium is that it better enables the introduction of the direct Brayton cycle, because there is relatively little industrial experience with helium-driven turbomachinery. In fact, there are only three historical examples of helium turbines, and only two of these were coupled to nuclear reactors[21]. All other historical helium-cooled reactors have transferred their heat to a secondary working fluid. The difficulties with helium turbomachinery arise mostly because of two factors. First, helium's low molecular weight allows it to travel along undesirable pathways, including via diffusion through heavy materials, leakage from the system, and leakage within the system causing certain components to receive less than optimal coolant flow[21]. Second, achieving a high compression ratio with helium requires a very long and multi-stage compressor-turbine assembly, resulting in unpredictable harmonic disturbances along the axis of the assembly[21]. Air-driven turbomachinery, however, could easily be derived from experience in the natural gas industry[22].

2.4 Selection of Fast Spectrum

While noble gasses can be used to cool either a thermal or fast spectrum reactor, the choice of air as a coolant is best combined with the choice of a fast-spectrum reactor. This is due to a combination of the following factors. Air, like other gasses, is not dense enough to serve as a neutron moderator. Air is also not a suitable coolant for use in a graphite-moderated thermal reactor, because of the corrosive, possibly even combustible effects of oxygen on graphite at high temperatures[23]. In fact, the development of the thermal, helium-cooled, graphite-moderated Very High Temperature Reactor (VHTR) has necessitated the study and mitigation of its own type of accident, the air-ingress accident[23]. Because a fast reactor design deliberately excludes extensive use of neutron moderating materials such as graphite, this problem is easy to avoid; however, each material to be exposed to air still must be scrutinized for its chemical behavior in the presence of oxygen[7].

A fast reactor has the advantages of enabling the design of a smaller core, as well as the long term (arguably on the order of thousands of years) benefits of closing the fuel cycle and facilitating waste management. A chief disadvantage of a fast reactor is the immediate cost of fuel fabrication, because a fast reactor requires a much higher initial fissile inventory than a thermal reactor[3]. Because of the marginally increasing cost of each incremental stage of enrichment, it is incumbent on the designer to minimize the enrichment required to operate the reactor. This disadvantage is magnified as the core design becomes small. The U.S.-European GFR demonstration plant program featured a 1500 MWe design that called for an average enrichment of 13.3%, while its 300 MWe design required 17.0% enrichment[12]. It is therefore conceivable that a design as small as 10 MWth, with the aim of minimizing size for ground transport, could require an initial fissile inventory several times higher than these values. While liquid-cooled SMRs routinely make use of fuel enriched well beyond these examples, it is a more difficult task for a GFR to extract the energy over the course of the reactor's lifetime to justify the initial cost. Failure to optimize in this regard would significantly reduce the size of the economic niche for the proposed design.

3. APPLIED CODE SYSTEM AND ANALYSIS METHODOLOGY

3.1 Introduction

Once having justified the selection of several design features for use in a deployable SMR, the procedure for meeting the design goals in support of the selected concept is to identify iteratively a suitable combination of geometry and materials, so that the reactor's neutronic, thermal-hydraulic, and thermodynamic requirements are satisfied simultaneously. The design approach is divided into these three main technical aspects in order to exploit the natural physical "seams" in a nuclear system where coupling and feedback can be characterized using a few parameters and reasonable assumptions. The scheme of the design approach is depicted in Figure 1.

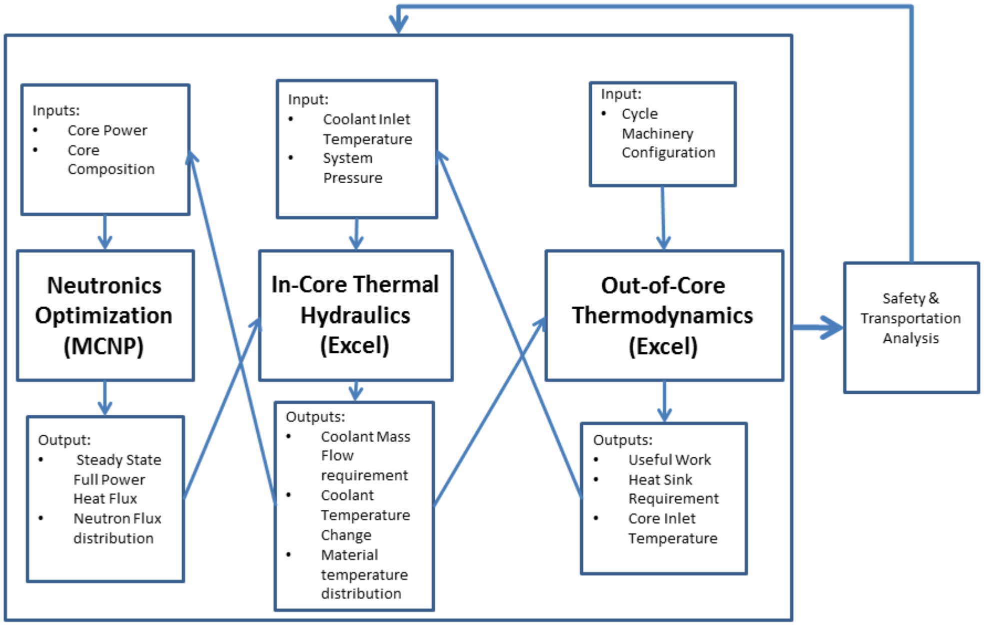

Figure 1. Design approach.

The desired power output and the transportability requirement drive the initial sizing of the reactor, which in turn drives the initial selection of the fuel composition. The fuel composition must be such that the reactor can produce the desired power for an acceptable length of lifecycle.

3.2 Computational Tools

The division of effort into the realms of neutronics, core thermal-hydraulics, and cycle thermodynamics is also suitable for the set of analytical tools available for such a design task.

The Monte Carlo N-Particle (MCNP) transport code[24,25] was used to analyze the neutronics (the criticality, spectrum, flux distribution, controllability, feedback parameters, etc.) at each iteration of the design.

The 1-D thermal-hydraulics of the system were analyzed using Microsoft Excel to automate calculations, and using Fourier's law and the Gnielinski correlation as the foundation of this analysis. The most significant outputs from the thermal-hydraulic analysis are the average and maximum temperatures of the core materials and coolant. The design goal is to maintain safe temperatures while maximizing the temperature change in the coolant.

The thermodynamic efficiency of the system, as well as the necessary heat exchange regime for the ultimate heat sink are also calculated using Excel, based on a set of equations that serve as an energy and mass balance for the reactor system[2].

A human, iterative interface among these three tools was necessary, and resulted in the optimization of some parameters, while other parameters received little scrutiny if they were simply deemed acceptable.

3.3 Methodology

In the thermal-hydraulic analysis, the assumption of uniform radial flow distribution, combined with an assumed cosine-shaped axial power distribution (as if the reactor were bare, and not reflected)[2], provide conservative estimates of the maximum cladding and fuel temperatures. However, the mesh-tally function of the Monte Carlo N-Particle transport code[24] (MCNP) enables a more accurate characterization of the normalized flux distribution, both radially and axially. For the steady-state reactor, an identical spatial dependence may be inferred for the heat generation distribution in order to obtain a more realistic value for the maximum cladding and fuel temperatures[2]. Beginning with the assumption of a steady power output, the key task is to verify that this heat (as well as a roughly 7% initial decay heat[26] in the event of a LOCA and SCRAM) can be dissipated with a reasonable, achievable flow regime. This is done in Microsoft Excel. MCNP can then be used to verify that the reactor can remain critical while producing the material temperatures (identified using the Gnielinski correlation[4]) corresponding to the power output.

Next, while this method identifies the cooling regime necessary for safe material temperatures, the efficiency of power extraction can simultaneously be judged at all times by the temperature change of the coolant as it passes over the core. This is done by means of a loose coupling of the calculated flow regime with a thermodynamic cycle that can be optimized using yet another set of automated calculations.

Finally, all of these linked analyses are viewed through the lenses of safety, environmental, economic, and licensing considerations. This justifies an approach that does not start too generally, and precludes design solutions that are too exotic.

3.3.1 Modeling of Core Neutronics

There are several steps taken, and MCNP files built, run, and analyzed before arriving (or settling upon) a final full-core model. In addition to being analyzed with respect to neutronic norms of the industry, thermal hydraulic considerations also drive the revision and optimization of these calculations, in accordance with the design approach outlined in Figure 1. Then there are many additional simulations to perform using MCNP in order to analyze the full core model. The following is a list of these steps:

1. For a transportable system, estimate a core height conducive to ground transportation. Given a standard bridge clearance of 14 feet, and assuming that the reactor unit can rest on a vehicle platform 3 feet from the ground, the total height of the unit is limited to 11 feet or 4.3 m in this study[27]. Since reflection and shielding alone can require several feet of material, and this is not knowable at this point in the design process, let the active core height be limited to 0.5 m. Assume a small reference diameter for a fuel pin. Since air is anticipated to be a relatively poor coolant, a small pin diameter is an important advantage. Since a fast reactor is not optimized by maximizing criticality, there is no use in

conducting an infinite-lattice or pin-cell optimization. Propose a fuel type, with the desired enrichment. Assume the average coolant temperature, pressure and density. This assumption will only apply for MCNP simulations, since MCNP does not provide a continuous temperature dependent cross-section library, and the code treats materials as having uniform temperature and density. Estimate the operating temperature and density of the fuel. Propose a cladding material and thickness.

2. Assume a finite hexagonal lattice of fuel pins. Bound the lattice within the vessel proposed in step 1. Run a KCODE[24] calculation. Run the calculation several times, adjusting the number of pins and/or the composition of the fuel until k_{eff} is slightly supercritical, in order to provide enough excess reactivity for a desirable core lifetime.
3. Assume a control rod material and geometry that will fit into a slot for a fuel pin. Select slots in which to place control rods by running several MCNP simulations.
    a. First, run a MCNP input deck with no control rods, using the FMESH[24] card to conduct a mesh-tally of the total flux in a radial slice of the core. Use the mesh tally output to identify the location(s) where the flux is highest. Assume that this location is also where the steady-state heat generation rate is highest.
    b. Remove the fuel pin(s) where the flux is highest, and place a control rod fully inserted into its place. Re-run the mesh-tally to identify the new

    location(s) of the highest flux. Replace the fuel pins at these locations with control rods, and repeat the process.

    c. Repeat this process until k_{eff} is at a sufficiently sub-critical value. It is sufficiently subcritical when later burnup calculations demonstrate that the control rods have enough reactivity to shut down the reactor at all points in the core lifetime.

4. Place all control rods fully inserted into those slots. Reduce the fuel temperature to room temperature, or its coldest anticipated temperature; increase its density to reflect the temperature change, but preserve the fuel mass. Run a KCODE calculation with a BURN card[25] for the fuel. Ensure that the reactor remains sufficiently subcritical when control rods are inserted throughout the desired lifetime of the fuel. Adjust the size, number, placement, and composition of the control rods to ensure this.
5. Place all control rods in the fully removed position. Specify that the fuel is at its operating temperature and density. Run a KCODE file with a BURN card for the fuel. Ensure the reactor remains critical when the rods are removed, for the entire desired lifetime of the fuel. Adjust the size, number, placement, and composition of the control rods to ensure this. The fuel pitch or composition may also be adjusted to include burnable poisons[28], which reduces control rod reactivity necessary to control or shut down the reactor.
6. Steps 4 and 5 ensure that there is enough reactivity available in both the fuel and the control rods to keep the core operating throughout its lifetime, while also

maintaining the ability to shut down the reactor at any time, and keep it shut down. Once this is verified, it is necessary to identify its operating, critical configuration. Perhaps several rods are fully removed, while some are fully inserted as burnable poison rods, and perhaps just one rod is partially inserted to fine tune the reactor to a steady power level. Run several KCODE calculations to identify this critical configuration with high precision. Take note of the fission yield and the prompt neutron lifetime.

7. Run an axial mesh-tally in the hot channel / fuel rod to identify the axial peaking factor.
8. Run a radial mesh-tally to identify the radial peaking factor in a slice at the axial center of the reactor.
9. Run several F4 tallies (i.e.: calculations within MCNP to count the neutron flux in a particular simulated volume[24]) to identify the spectrum of the reactor at several points within the reactor.
10. Run a KCODE file for the critical configuration using the TOTNU card to calculate the reactor's multiplication factor with only prompt neutrons[24]. The TOTNU card instructs MCNP whether or not to consider delayed neutrons along with prompt neutrons in a simulation[24]. Use this result and the result from step 6 to calculate the reactor's delayed neutron fraction.
11. Model the reactor's behavior in the event of a LOCA, or depressurization accident. To do this, take the critical configuration, and reduce the coolant

density to reflect atmospheric pressure. Run a KCODE calculation, and use it to calculate α_{void} , the void coefficient of reactivity[3].

12. Find the reactor's fuel temperature coefficient of reactivity. Take the critical configuration, and adjust the fuel temperature to room temperature.
13. Find the reactor's fuel temperature coefficient of reactivity, this time changing both the temperature and density of the fuel.
14. Find the reactor's coolant temperature coefficient of reactivity. Assume pressure remains the same as in the critical configuration, but let the coolant be at room temperature.
15. Identify the lifetime neutron fluence in structural materials. Adjust cladding thickness, and/or vessel thickness as needed.

3.3.2 Thermal-Hydraulic Assumptions

For the purposes of transportability and neutron economy, the active core height in this design is fixed at 0.5 m. Limiting the height of the active core leaves room for axial reflector and shielding materials, inlet and outlet gas plena and plumbing, control rods and drives, and other structures, while still enabling the system to fit on a vehicle with a reasonable height, as mentioned in step 1 above. Since this system is a fast reactor, limiting the height also helps to improve the neutron economy by reducing leakage. However, a shorter core height means the coolant has a shorter distance in which to achieve a large temperature difference.

Next, let us begin with a goal of 30 MW of thermal power production, Q, under normal full-power operating conditions. This is justified in section 4.3 in order to make the reactor economically competitive with other GFR designs.

The starting pitch-to-diameter ratio was inferred from a reference design[12].

All heat is assumed to be produced in the fuel itself. The core in these calculations is assumed to be insulated so that all heat produced in the fuel must be dissipated only by the coolant flowing in the channels adjacent to the fuel. This results in a conservatively high estimate of the coolant flow rate required to remove heat from the core.

3.3.3 Use of Fourier's Law and Gnielinski Correlation

The core geometry and composition from the neutronics model, and the equations shown in this section are compiled, linked, and automatically updated in a spreadsheet for easy analysis of the core cooling capabilities.

Using reference values for the radial dimensions of a fuel element, along with the self-imposed maximum core height H, the volume of fuel in a single cylindrical fuel pin[28] is given as

$$V_f = \pi r_f^2 H \tag{1}$$

Here, r_f is the radius of the fuel material itself.

Then, from the core geometry produced during the initial core-size optimization via the neutronics modeling, the number of fuel elements enables the calculation of the total volume of fuel in the core:

$$V_{f,core} = V_f N_{fe} \tag{2}$$

The volume of one entire fuel element[28] in the active core is calculated via Eq. 3, where r_{co} is the radius to the outside of the fuel element cladding.

$$V_{fe} = \pi r_{co}^2 H \tag{3}$$

A pitch-to-diameter ratio is specified, starting with a reference range for fast reactors. A p/d ratio of 1.5 is considered the upper limit in this study[12], while the theoretical lower limit is 1.0. Given the fixed fuel element dimensions described above, the p/d ratio yields the fuel pin pitch, p. The lattice size of a hexagonal sub-assembly, being characterized by N_{rings} , the number of fuel pin rings beyond the central pin, enables the calculation of the sub-assembly pitch, p_{sa}.

$$p_{sa} = \left(\frac{p}{2} + pN_{rings} + \frac{p}{6}\right)\sqrt{3} = p\sqrt{3}\left(\frac{2}{3} + N_{rings}\right) \tag{4}$$

The total cross sectional area of the active core is given by

$$A_{core} = \frac{p^2 N_{fe}\sqrt{3}}{2} \tag{5}$$

Neglecting control rod sub-assemblies, the total volume of the active core is given by

$$V_{core} = A_{core} H \tag{6}$$

The average core power density is then given by Eq. 7, where Q is the total heat production rate in the core.

$$PD = \frac{Q}{V_{core}} \tag{7}$$

The total area of all fuel element coolant channels in the core is given by

$$A_{ch,tot} = A_{core} - (N_{fe}\pi r_{co}^2) \tag{8}$$

The total wetted perimeter of all fuel element cladding in the core is given by

$$P_{w,tot} = 2\pi r_{co} H \tag{9}$$

The effective diameter of a single coolant channel is given[2] by

$$D_{ch} = \frac{4A_{ch}}{P_w} = \frac{4A_{ch,tot}}{P_{w,tot}} \tag{10}$$

The average linear heat production rate is defined as the total thermal power production in the core, divided by the total length of all fuel rods in the core, and is given[2] by

$$q'_{avg} = \frac{Q}{N_{fe}H} \tag{11}$$

The maximum linear heat production rate in the core is found by multiplying the average rate by the power peaking factor inferred from the neutron flux profile, as in Eq. 12.

$$q'_{max} = q'_{avg} F_q \tag{12}$$

Then, using the sinusoidal power distribution in the axial direction found using the MCNP mesh tally function, the bulk coolant temperature in the hot channel, T_b, is given as a function of the axial position in Eq. 13[28]. Other portions of this analysis assume that the mass flow rate, w, is the same in all coolant channels. This is a conservative assumption, because in reality, the mass flow rate is likely to be higher in the central channels, where the power density is greatest[4].

$$T_b(z) = T_{b,in} + \frac{q'_{max}}{wc_{p,b}} \left(\frac{H}{\pi} \left(\sin\left(\frac{\pi z}{H}\right) + \sin\left(\frac{\pi}{2}\right) \right) \right) \tag{13}$$

This is the ideal steady state temperature profile of the coolant in the hot channel. It is used to calculate the average coolant temperature in the hot channel. This also enables the calculation of the hot channel linear heat rate, as a function of axial position. Again, assuming a sinusoidal power profile with a maximum given by Eq. 12, the hot channel linear heat rate is given by Eq. 14.

$$q'(z) = q'_{max} \cos\left(\frac{\pi z}{H}\right) \tag{14}$$

The next step is to calculate the average Reynolds number[4], Re, of the coolant flow in the hot channel. Here, the Reynolds number is given as

$$Re = \frac{GD_{ch}}{\mu} \tag{15}$$

Here, μ is the dynamic viscosity of the coolant, and G is the coolant mass flux, which must be constant, if both the channel diameter and mass flow rate are also to remain constant. The viscosity is taken at the reference inlet temperature and system pressure, though the viscosity exhibits little dependence on pressure[29]. G is given[4] by

$$G = \frac{w}{A_{ch}} = \rho_b v \tag{16}$$

Therefore, if G is a constant, then ρ and v, the coolant density and velocity, must be inversely related everywhere in the channel. The coolant density may be calculated using a modified ideal gas equation, the system pressure (neglecting the core pressure drop), and the coolant temperature profile from Eq. 13, The axial density profile of the coolant is given by Eq. 17[30].

$$\rho_b(z) = \frac{ZP}{R_{spec}T_b(z)} \tag{17}$$

In this equation, R_{spec} is the specific ideal gas constant for the coolant. The compressibility factor, Z, is an empirical correction factor that is tabulated for state points at which the behavior of a gas departs from the ideal gas law[30].

The velocity in an individual channel is considered 1-dimensional. For simplicity, the velocity profile of the channel cross section is considered uniform. The velocity profile along the channel axis, however, is calculated simply by inserting the density profile into Eq. 16.

Next, the Prandtl number, Pr, is calculated using Eq. 18, where k_b is the thermal conductivity[29] of the coolant at the inlet temperature and pressure (assumed to be the system pressure).

$$Pr = \frac{\mu c_{p,b}}{k_b} \tag{18}$$

The Reynolds number and Prandtl number are used in the Gnielinski correlation for convective heat transfer in smooth pipes with turbulent flow[4], Eq. 19. The Gnielinski correlation gives the Nusselt number, the definition of which is given by Eq. 20. The Darcy-Weisbach friction factor, f_{DW}, can be found using Eq. 21 for turbulent flow in smooth pipes[4].

$$Nu = \frac{\left(\frac{f_{DW}}{8}\right)(Re-1000)Pr}{1+12.7\left(\frac{f_{DW}}{8}\right)^{0.5}(Pr^{2/3}-1)} \tag{19}$$

$$Nu = \frac{h_b D_{ch}}{k_b} \tag{20}$$

$$f_{DW} = (0.7904\ln(Re) - 1.64)^{-2} \tag{21}$$

In the case of laminar flow (considered Re<3000 here), the Nusselt number is held constant at a value of 3.66, which assumes that the flow regime holds the cladding at a steady state temperature[31].

By combining Eqs. 19 and 20 , one can solve for h_b, the convective heat transfer coefficient of the bulk. This initial calculation may be taken as the value at the inlet, because again, the component of the Reynolds number, ρv, must be a constant in order for the channel diameter and mass flow rate also to be constant. Knowing h_b enables the calculation of the outer cladding temperature, T_{co}. However, h_b does not remain constant along the channel axis. Its dependence upon position in the channel can be characterized by solving Eqs.[2] 22 and 23 numerically along an axial mesh, the fineness of which determines the resolution of the functions $h_b(z)$ and $T_{co}(z)$.

$$h_b(z) = \frac{q'(z)}{2\pi r_{co}(T_{co}(z) - T_b(z))} \tag{22}$$

$$T_{co}(z) = T_b(z) + \left(\frac{q'_{max}}{2\pi r_{co} h_b(z)}\right) \cos\left(\frac{\pi z}{H}\right) \tag{23}$$

From this point forward, the problem of identifying the radial temperature profile in the hottest fuel pin is a matter of characterizing the thermal resistance offered by each material in the fuel pin as heat is conducted outward toward the coolant.

The inner cladding surface temperature is given as

$$T_{ci}(z) = T_{co}(z) + \frac{q'_{max}}{2\pi k_c} \ln\left(\frac{r_{co}}{r_f}\right) \cos\left(\frac{\pi z}{H}\right) \tag{24}$$

Solving for the temperature at the surface of the fuel is done by Eq. 25, but it requires knowledge of the effective thermal conductivity of the gap, which is typically filled with helium during manufacturing. Although this composition changes over the course of a fuel element's life, the effective thermal conductance is well approximated as the thermal conductivity of helium, which is given in Eq. 26[32].

$$T_{fo}(z) = T_{ci}(z) + \frac{q'_{max}}{2\pi k_g} \ln\left(\frac{r_{ci}}{r_f}\right) \cos\left(\frac{\pi z}{H}\right) \tag{25}$$

$$k_g = 0.04679 + 3.81 \times 10^{-4}\, T_g - 6.786 \times 10^{-8}\, T_g^2 \tag{26}$$

Finally, the centerline fuel temperature is given by Eq. 27, where k_f is considered constant throughout the fuel element after being taken at the temperature at the outside of the fuel.

$$T_f(z) = T_{fo}(z) + \frac{q'_{max}}{4\pi k_f}\cos\left(\frac{\pi z}{H}\right) \tag{27}$$

The coolant velocity is limited by the pumping power available, the vibrational tolerance of core structures, and the speed of sound[6]. While helium flow is typically 70 to 120 m/s in GFR designs[11,33], assuming the reactor can be built to withstand whatever coolant velocity is found to be necessary for temporary transient conditions, the speed of sound is considered the true physical limitation. The speed of sound in dry air at 600K is given[34] by

$$v_{sound} \approx 331.4 + 0.6T_b \tag{28}$$

The coolant velocity will be greatest at the exit of the hot channel, as will the speed of sound (as predicted by Eqs. 16 and 17, given constant *G*). It is useful, therefore, to calculate the speed of sound at all locations in the hot channel, to ensure that the fluid velocity is below the speed of sound at all locations. This is a simple task, given Eq. 28, which correlates the sound speed solely to the fluid temperature. If this velocity is lower than the speed of sound at that location and its associated air temperature, then the flow velocity is considered attainable with respect to the sound barrier, for the purpose of this study. Under normal operating conditions, the coolant will not approach the sound barrier, but it is of greater concern in the case of a DLOCA, where the fluid density is greatly reduced, and the velocity must increase dramatically to maintain cooling, as per the Gnielinski correlation.

The pumping power may also be considered a practical limitation because of both the pressure-drop due to surface friction and the power requirement to overcome it, which increases as the square of the coolant's superficial velocity[2]. The needed pumping power may become prohibitively large even at an appreciable fraction of the speed of sound. The pressure loss due to cladding surface friction is determined for this design by the use of the Darcy-Weisbach correlation[2], given by Eq. 29.

$$\Delta P_{friction} = f_{DW}\frac{H}{D_{ch}}\left(\frac{\rho_b v^2}{2}\right) \tag{29}$$

The pumping power required to overcome this pressure drop is given by Eq. 30, in which the pumping efficiency η_{pump} is assumed to be 95%[2].

$$P_{fric} = \frac{1}{\eta_{pump}}\Delta P_{friction}\left(\frac{w}{\rho_b}\right) \tag{30}$$

3.3.4 Accident Modeling and Safety

It is not enough to demonstrate that an air cooled fast reactor can remain critical at some operating power and fuel temperature while being cooled adequately so that all material temperatures are safe under operating conditions. This is because of the problem of decay heat removal in the event of degraded cooling. The term for the rapid shut-down of a reactor is a historical acronym for Safety-Control-Rod-Ax-Man (SCRAM), which implies that control rods are inserted into the reactor passively after a trigger. After a successful SCRAM, a fission reactor can be assumed to drop instantly to approximately 7% of its steady state power prior to the SCRAM[26]. This decay heat then decreases exponentially with time[26]. For a gas cooled reactor, a likely cause of degraded cooling is a Depressurization Loss of Coolant Accident (DLOCA). This is a more serious problem for a GFR than for a LWR or HTR, because a LWR can be cooled in an emergency just by keeping liquid water in the pressure vessel at atmospheric pressure, while a HTR's graphite moderator is designed to serve as a heat sink until marginal decay heat production can be dissipated by natural convection and radiation[26]. Therefore, it is important to model the core's capability to reject heat into coolant at atmospheric pressure, and it is important that the coolant mass flow rate for this scenario not require significant pumping power. The maximum amount of decay heat able to be removed from a reactor configuration in a DLOCA and SCRAM scenario will therefore determine the maximum thermal power rating for normal operations. This requirement is conservative in that the power drops rapidly from 7% of full power, and it does not account for emergency cooling systems, both passive and active, which may be included in the design.

3.3.5 Thermodynamic Cycle Modeling

One of the chief advantages of gas cooling in a reactor is the possibility that the coolant gas may be used directly as the working fluid in the thermodynamic cycle. The direct Brayton cycle can eliminate the need for multiple coolant loops, and is generally capable of higher efficiency than the Rankine cycle[2]. In this thesis, two forms of the direct Brayton cycle are considered. The first cycle is an open cycle, in which the compressor takes air directly from the atmosphere, then heats it in the reactor, expands it across the turbine, and then exhausts it into the atmosphere. The second is a closed cycle, in which the primary coolant is contained and recirculated through the compressor, reactor, and turbine, and a heat exchanger where excess heat is transferred to the ambient atmosphere. These two cycles also include recuperation of some of the exhaust heat. Figures 2 and 3 show these two schemes.

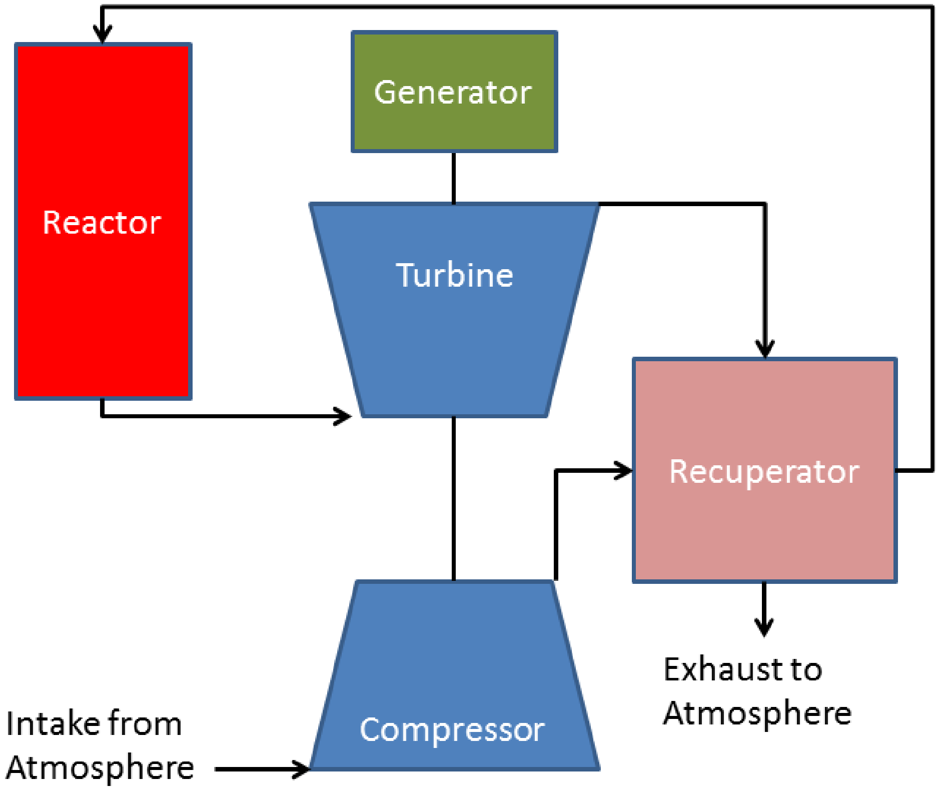

Figure 2. Open, direct Brayton cycle with recuperation[2].

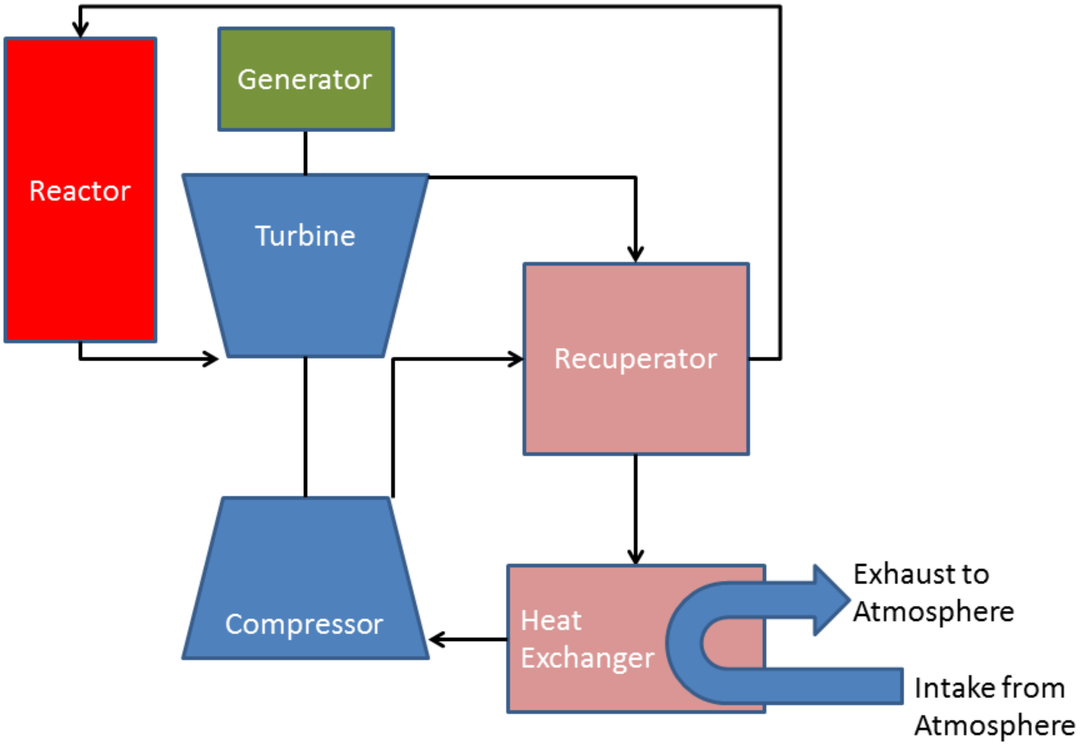

Figure 3. Closed, direct Brayton cycle with recuperation[2].

The open cycle has the advantage of eliminating the heat exchanger, along with its maintenance costs, capital investment, and power consumption, and recovering the space it would occupy on a vehicle. The closed cycle also has the advantages of a lower release of fission products and the activation product Ar-41. This study attempts to optimize both of these cycles with respect to thermodynamic efficiency, given the constraints of the core geometry, as well as the temperature limits of the fuel, cladding, and turbine blades. If the heat exchanger consumes a large amount of power in the closed cycle, and if the Ar-41 production rate can be demonstrated to be acceptable in the open cycle, then the open cycle would have a clear advantage. Figure 4 serves as a general temperature vs. entropy diagram for both of these cycles, except that state-point number 6 is eliminated in the case of the open cycle, because the heat exchanger is eliminated in favor of expelling the exhaust directly into the atmosphere while the compressor takes in fresh air directly from the atmosphere.

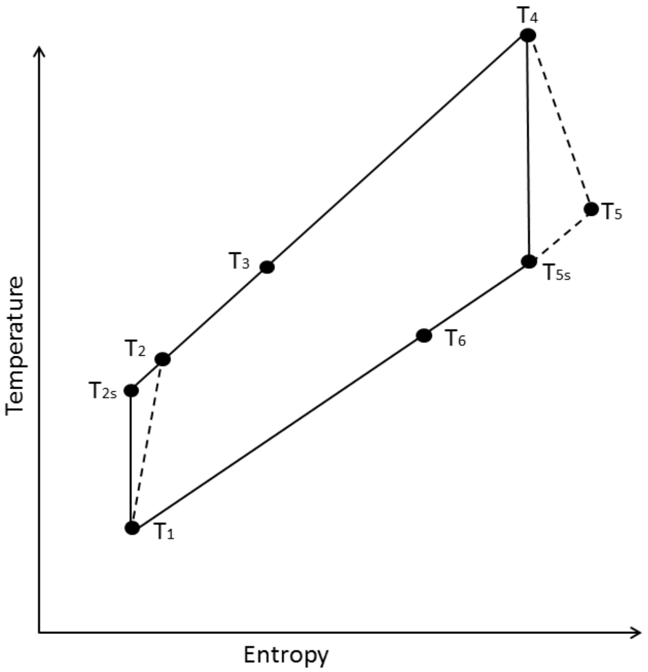

Figure 4. Temperature-entropy diagram of a direct Brayton cycle with recuperation.

The gross thermodynamic efficiency[2] is defined by Eq. 31, where W_T is the work done on the turbine, W_C is the work required to operate the compressor, and Q is the head added by the reactor.

$$\zeta = \frac{W_T - W_C}{Q} \tag{31}$$

Since the work done on or by any component is equal to the mass flow rate times the enthalpy change in the fluid in that component[2], Eq. 31 is rewritten as Eq. 32, where i_n is the enthalpy at state point *n*, as identified in Figure 4.

$$\zeta = \frac{w(i_4 - i_5) - w(i_2 - i_1)}{w(i_4 - i_3)} \tag{32}$$

Since these cycles have equal flow rates in all components, this simplifies to Eq. 33.

$$\zeta = \frac{(i_4 - i_5) - (i_2 - i_1)}{i_4 - i_3} \tag{33}$$

Because air can be approximated as an ideal gas[30], the enthalpies can be rewritten as the product of the temperature at each state-point, and the constant-pressure heat capacity, which has little temperature dependence[2], as in Eq. 34.

$$\zeta = \frac{c_p(T_4 - T_5) - c_p(T_2 - T_1)}{c_p(T_4 - T_3)} \tag{34}$$

Equation 34 then simplifies to Eq. 35, which states that the cycle efficiency can be determined if the temperatures are known at all state-points.

$$\zeta = \frac{(T_4 - T_5) - (T_2 - T_1)}{(T_4 - T_3)} \tag{35}$$

In order to identify the inlet and outlet temperatures of the reactor component, it is logical to begin with the compressor inlet temperature. This value can be assumed to be the ambient temperature for the open cycle system. It can be assumed as any value equal to or greater than the ambient temperature for the closed cycle system, provided that the heat exchanger is eventually designed to return the gas to the compressor at that assumed temperature. For this study, let the ambient temperature, T_1, be set at 296 K.

The compressor is characterized by Eq. 36, in which T_2 is the compressor outlet temperature, T_{2s} is the isentropic compressor outlet temperature, and η_C is the isentropic efficiency of the compressor[2]. The compressor efficiency can reasonably be assumed to be 90%[35].

$$T_2 - T_1 = \frac{1}{\eta_C}(T_{2s} - T_1) \tag{36}$$

For an ideal gas, the turbine isentropic efficiency is given[2] by

$$T_{2s} = T_1 \left(\frac{P_2}{P_1}\right)^{\frac{\gamma-1}{\gamma}} \tag{37}$$

The specific heat ratio, γ, is the ratio of the specific heat at constant pressure to the specific heat at constant volume[2].

$$\gamma = \frac{c_p}{c_v} \tag{38}$$

For an ideal gas, this value is constant, and is assumed so for the remainder of this study. The constant value of γ that is assumed for this study is taken at a temperature of 600 K, and is calculated[29] as

$$\gamma = \frac{1110 \left[\frac{J}{kg\ K}\right]}{823 \left[\frac{J}{kg\ K}\right]} = 1.35$$

The ratio of the outlet pressure to inlet pressure is also known as the compression ratio[2], and is an engineered property of the compressor. Compression ratios up to 16 are typical in gas turbine designs[36].

$$r_c = \frac{P_2}{P_1} \tag{39}$$

The turbine is characterized by Eq. 40[2], where η_T is the turbine isentropic efficiency, reasonably assumed to be 90%[35]. The turbine inlet temperature, T_4, is equal to the reactor outlet temperature, and has an upper limit of approximately 1025 K[35], which is the maximum operating temperature of the turbine. T_4 may be limited to an even lower temperature if maintaining core temperatures requires an increased mass flow rate. The value of T_4 is taken from the result of applying the Gnielinski correlation as described in section 3.3.3. This requires an initial value of T_3 to have been used in the Gnielinski correlation, but both T_3 and T_4 are subject to refinement by numerical iteration as described further in the remainder of this section.

$$T_4 - T_5 = \eta_T (T_4 - T_{5s}) \tag{40}$$

Similarly to the compressor, the temperature at the isentropic state point is given by

$$T_{5s} = \frac{T_4}{\left(\frac{P_4}{P_5}\right)^{\frac{\gamma-1}{\gamma}}} \tag{41}$$

For an ideal gas in a Brayton cycle, the inlet to outlet pressure ratio for the turbine is equal to the compression ratio.

$$r_c = \frac{P_2}{P_1} = \frac{P_4}{P_5} \tag{42}$$

The recuperator efficiency is given by Eq. 43, but is held constant in this study at 90%, although some recuperators have achieved up to 95% efficiency[35].

$$\xi_{Recup} = \frac{T_3 - T_2}{T_5 - T_2} \tag{43}$$

With the above information, it is possible to calculate the gross thermodynamic efficiency using Eq. 35. The gross thermodynamic efficiency accounts for the work required by the compressor, and the heat rejected to the environment. The following equations enable the calculation of the net thermodynamic efficiency, meaning that they also account for friction losses in the core as well as the power required by the heat exchanger.

The recuperator outlet temperature, T_6, represents the temperature of the air to be exhausted into the atmosphere in an open Brayton cycle, or cooled further in a heat exchanger for recycling to the compressor. For both cases, it is calculated by Eq. 44[2].

$$T_6 = T_5 + T_2 - T_3 \tag{44}$$

In the case of a closed Brayton cycle, it is necessary to identify the amount of additional heat, Q_{out}, to be removed from the primary coolant by the heat exchanger in order to return it to the compressor at the initially assumed temperature T_1. This value is calculated using Eq. 45[2].

$$Q_{out} = (T_6 - T_1)c_p w \tag{45}$$

It is then necessary to specify the change in temperature, ΔT_{hs}, of the heat sink air used to cool the primary coolant. In this study, two cases are presented. The first assumes that the heat exchanger can return the primary coolant to the compressor at the ambient air temperature of T_1=296 K. This is not an unrealistic assumption[37], especially if the ambient temperature is less than 296 K. The second case assumes that it can return the air to the compressor at T_1=350 K. ΔT_{hs} is calculated using these two values in Eq. 46.

$$\Delta T_{hs} = (T_6 - T_1) \tag{46}$$

Then the necessary mass flow rate of ambient air through the heat exchanger is calculated using Eq. 47.

$$w_{hs} = \frac{Q_{out}}{c_p \Delta T_{hs}} \tag{47}$$

Next, the pumping power required to operate the heat exchanger is calculated by Eq. 48[2]. In this equation, η_{pump} is the efficiency of the heat exchanger pump, and is assumed to be 95%[2]. ΔP_{pump} is the pressure drop across the pump, and is set equal to the typical value of 0.0035 MPa, as advertised for commercial air-to-air heat exchangers[38]. ρ_{amb} is the ambient air density, and is calculated as 1.19249 $\frac{kg}{m^3}$ via a modified Eq. 17.

$$P_{hs} = \frac{1}{\eta_{pump}} \Delta P_{pump} \frac{w_{hs}}{\rho_{amb}} \tag{48}$$

The net thermodynamic efficiency is then calculated as

$$\zeta_{net} = \frac{Q - Q_{out} - P_{fric} - P_{hs}}{Q} \tag{49}$$

To summarize, the gross thermal efficiency is calculated using Eq. 35. T_1 is an assumed value. T_2 is calculated using Eq. 36, combined with Eqs. 37 and 38, where the compressor efficiency is an assumed value, the heat capacity ratio is assumed temperature-independent, and the compression ratio remains a variable to be optimized. T_3 is the subject of a numerical convergence scheme; it is first specified by the user in order to obtain T_4 via the Gnielinski correlation (as explained in section 3.3.3). T_4 is then used to calculate the remaining temperatures in sequence, including an updated value of T_3, which is then re-inserted into the Gnielinski correlation. This iteration continues until T_3 converges to within one tenth of one Kelvin for purposes of this study. T_5 is calculated using Eq. 40 combined with Eqs. 41 and 42, where again, the specific heat ratio has remained constant, the compression ratio is the same variable used in Eq.

36, and the turbine efficiency is an assumed value. The updated value of T_3, referred to above, is calculated via Eq. 43, using an assumed value of the recuperator efficiency. This suffices for the calculation of the gross thermodynamic efficiency. For the net thermodynamic efficiency, a mass and energy balance is established via Eqs. 44-49. Since the compression ratio remains a variable, this calculation must be repeated for a range of values of the compression ratio. This process yields a collection of data in which to identify the compression ratios for the open and closed cycle that yield maximum efficiency. The maximum efficiencies of the open and closed cycle may then be compared, and weighed against other factors (radiation release rates, DLOCA considerations, equipment required, etc.) to determine, if possible, which cycle is superior to the other.

4. CONCEPT DEVELOPMENT AND DESIGN

4.1 Thermal Properties and Selection of Materials

The thermal properties of the materials involved are necessary for the system of calculations described in chapter 3. The materials involved are the coolant, the gap-fill gas (helium), the cladding, and the fuel.

The coolant air must be characterized by its density, viscosity, heat capacity, and thermal conductivity. The density of the air is given as a function of temperature and pressure by Eq. 17. For the purposes of the calculations completed in this study, the density is recalculated instantaneously whenever the air temperature or pressure changes. The air's density is also calculated as a function of the axial position in the hot channel. A tabulated value of the air's dynamic viscosity, μ, is taken at 600 K and a pressure of 9 MPa, and is assumed to remain constant throughout the study[29]. The value of the viscosity at this temperature and pressure is $3.1472E-5\ \frac{kg}{m\,s}$. The constant-pressure heat capacity, c_p, for air is also taken at 600 K, and assumed to remain constant at $1110\frac{J}{kg\ K}$, while the constant volume heat capacity is assumed to remain constant at $823\frac{J}{kg\ K}$[22]. Finally, the thermal conductivity, k_b, is also set at a constant value of $0.0476\ \frac{W}{m\,K}$, which is an experimentally derived value for 600 K and 9 MPa[29].

The only thermal property of the fill gas that significantly affects the thermal hydraulic calculations is its thermal conductivity, k_g, which for helium, is given as a function of the cladding temperature in Eq. 26. For the operating modes analyzed in this study, k_g ranged in value from 0.30 to 0.34 $\frac{W}{m\,K}$.

Although SiC has been chosen in this study as the best cladding for an air-cooled GFR, the three alternative cladding materials initially proposed were also analyzed for their effects on the temperature distribution in the core. The thermal properties of the cladding materials that were used for the thermal hydraulic calculations are tabulated in Table 2. Also tabulated in Table 2 are the relevant thermal properties of the UOX fuel. The fuel density and thermal conductivity were assumed to be constant throughout this study.

Table 2. Thermophysical Properties of Nuclear Fuel and Cladding Materials

Material Property	**Zircaloy**[2]	**SiC**[39]	**Inconel**[2,7]	**Stainless Steel**[40,41]	**UOX**[2]
Melting / phase change point [K]	2040	2727.7	1666.15	1780	~3000
Maximum irradiation temperature, steady[7] [K]	673.15	1173	773.15	873.15	N/A
Maximum irradiation temperature, transient[2] [K]	1477.6	1773	1206.8	1061.15	2173.15
Thermal conductivity, *k* [W/m K]	13	116.21	27.22	30	4.5
Density, ρ [kg/m^3]	6500	3210	8280	7899.76	10000

4.2 Core Structural Materials

Corrosion resistance is an important quality to analyze when choosing the fuel element cladding material. A zirconium alloy is usually chosen for a thermal reactor, because zirconium is relatively transparent to thermal neutrons compared to stainless steel[7]. In a fast reactor, there is no need to accommodate thermal neutrons, and stainless steel is a typical choice. However, since in this proposed GFR, the cladding will be in contact with high temperature air (as opposed to non-oxidizing helium), it becomes necessary to consider the relative thermal and oxidation behaviors of the cladding materials. Stainless steel corrodes quickly in such an environment, and is generally not suitable for prolonged exposure to air at high temperatures[42]. Zirconium also corrodes in the presence of oxygen, but in a Light Water Reactor (LWR) at steady state, the rate of corrosion plateaus after the initial buildup of a self-shielding oxidation layer, without an unacceptable impact on the heat transfer properties of the cladding[43]. If the zirconium cladding is exposed to water at higher temperatures, however, the oxidation rate is increased, as is the hydrogenation rate of the zirconium[7]. The hydrogen freed by the zirconium oxidation reaction diffuses into the zirconium alloy and forms zirconium hydrides, which are mechanically weaker than both the zirconium alloy and the zirconium dioxide patina[8]. This hydrogenation may contribute to the embrittlement and failure of fuel elements following a loss-of-coolant accident (LOCA) in a LWR. However, in an air-cooled reactor, even if the oxidation rate is similar to that of zirconium exposed to steam, the reaction clearly could not result in hydrogenation as in a LWR, because oxidation via air does not produce free hydrogen gas. These facts may indicate that zirconium is a more acceptable choice than steel with respect to its oxidation properties. Yet another alternative to consider is a nickel-based superalloy, which resists oxidation even at high temperatures, but its long term performance under neutron bombardment is questionable[7].

4.3 Initial Core Configuration

A typical PWR achieves a burnup of 45 $\frac{GWd}{tHM}$, while simulations[13] of a helium cooled GFR have achieved 48 $\frac{GWd}{tHM}$. A 30 MW reactor with 1 metric ton of heavy metal could achieve 48 $\frac{GWd}{tHM}$ with a core lifetime of 4.38 years, while maintaining a specific power of approximately 30 $\frac{W}{g}$ (compared to a specific power of approximately 69 $\frac{W}{g}$ for the GCFR[12]). A core lifetime of several years is justifiable given the expeditionary purpose of this reactor concept. One key task for the development of an initial core model is to identify the fissile fraction required in the fuel to attain this burnup.

Using a fixed fuel element radius of 3.6 mm, as well as a cladding thickness of 0.572 mm, and a gap thickness of 0.082 mm[12], one deduces a fuel pin radius of 2.946 mm. The volume of the fuel itself in a cylindrical fuel element, therefore, is given by Eq. 1, yielding:

$$V_f = \pi \times (0.002946\ [m])^2 \times 0.5\ [m] = 1.36E-5\ [m^3]$$

Assuming an oxide fuel density of 10 $\frac{g}{cm^3}$, and a total fuel weight of 1 ton, such a core would be composed of 100,000 cm^3 of fuel, which would fit into approximately 7335 fuel elements, each 0.5 m in length.

If the reactor is to fit into a cylindrical pressure vessel, it would be fitting for a fast reactor core assembly to be composed of hexagonally prismatic subassemblies of fuel rods, which are likewise arranged hexagonally[2]. A hexagonal lattice that can fit in a cylindrical vessel is achievable with a practical distribution of 127 subassemblies. Reserving 13 of these for control rods preserves hexagonal symmetry. Placing 61 fuel rods in each fuel subassembly and 24 fuel rods in each control rod assembly gives 7266 fuel elements, which amounts to 0.99 tons of fuel.

The control rod placement and their reactivity contribution to the system are explained further in section 4.11. Figure 5 below shows the final core configuration modeled. These diagrams were produced using the MCNP visual editor.

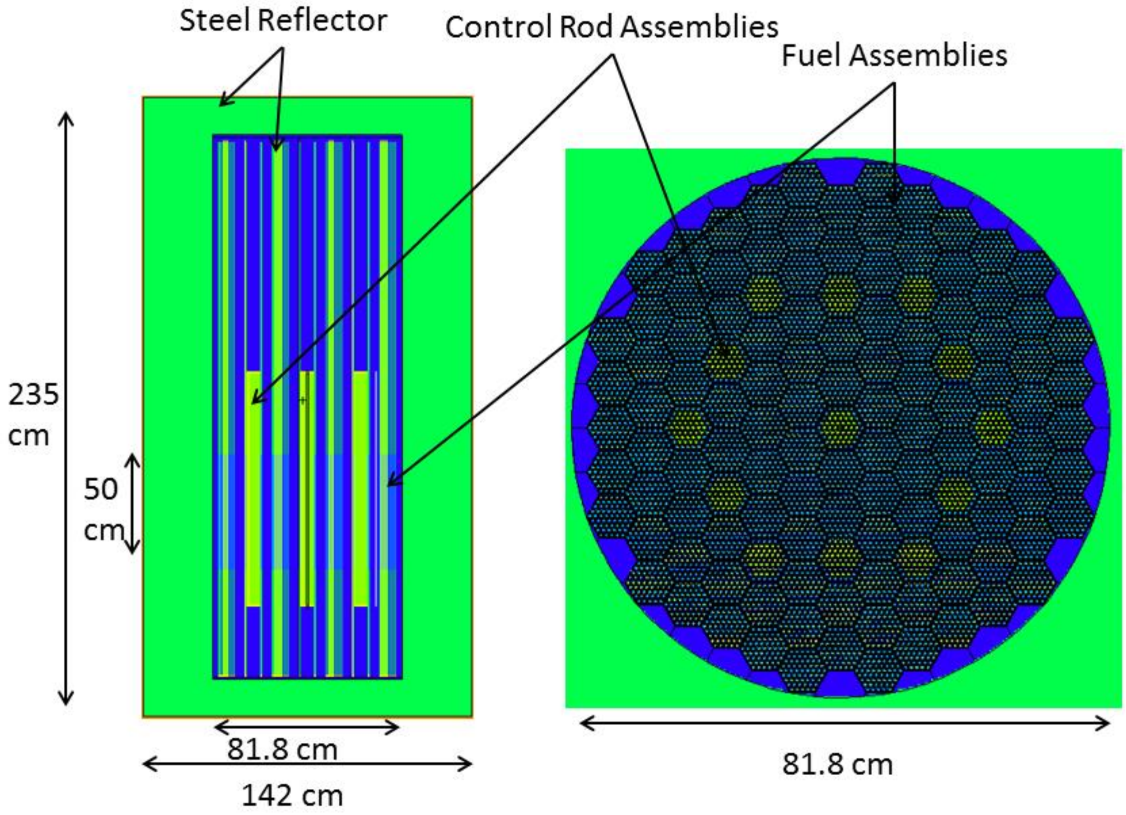

Figure 5. Side and top cross section views of an air-cooled fast reactor core.

4.4 Neutron Energy Spectrum

The neutron energy spectrum in this reactor is fast, and only slightly dependent upon the lattice spacing, according to Figure 6, which shows the spectra of the reactor with the smallest and largest p/d ratios considered. This figure is the result of MCNP simulations discussed in section 3.3.1. The p/d ratios between 1.01 and 1.4 are not shown here, but they portray a predictable, gradual shifting of the spectrum between the two shown here. This simplifies the remainder of the study, which varies p/d as well as the coolant mass flow rate, by validating the assumption that the spectrum remains relatively inflexible despite these changes.

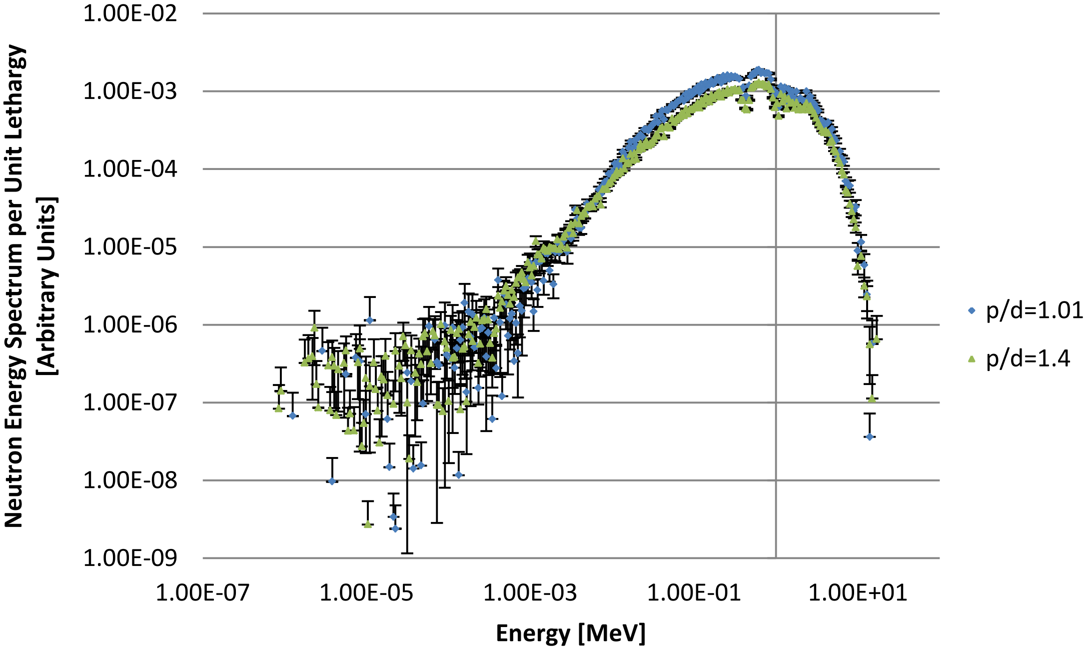

Figure 6. Neutron energy spectrum in the air-cooled fast reactor core.

While this spectrum indeed appears to be a very fast spectrum, there is a prominent and well-defined resonance at 0.4 MeV due mainly to the presence of oxygen in the fuel. It also features a noticeable depression in the flux above 1 MeV, also due to resonances in the cross section of O-16 in the fuel. Appendix B contains this spectral plot overlaid with the cross section of O-16, which serves to illuminate these spectral anomalies.

4.5 Fuel Burnup

The pitch-to-diameter ratio is of interest for any reactor, but optimizing this parameter is not as simple in a fast reactor as in a thermal reactor. In a thermal reactor, the design goal is typically to space the fuel so as to achieve a reactivity slightly below (remaining undermoderated for safety reasons) an easily identifiable maximum available reactivity, which occurs at a specific pitch that neither over-moderates nor under-moderates neutrons. That said, thermal reactors are typically designed to be slightly under-moderated for safety reasons. For a fast reactor, since the neutrons are not moderated, the maximum reactivity would occur when the core is densest and most reflected. Therefore, this metric cannot be approached without accepting unrealistic thermal hydraulic consequences. Instead, the core must be optimized with respect to multiple parameters, the weighting of which may be somewhat subjective. This means, barring any exotic fuel element shape or size, it is typically economical in a thermal reactor to let thermal hydraulic concerns conform to the most neutron-efficient configuration, whereas for a fast reactor, the two must be considered simultaneously[3].

The metric that indicates fuel economy is the burnup. The maximum achievable burnup is calculated here for several p/d ratios in a range of interest. In the MCNP burnup calculations performed here, a simplified approach was used in which the code does not account for the fact that fuel burnup occurs faster in high-flux regions of the core (usually the center)[25]. The depletion calculation simply removes the portions of the nuclides necessary to produce a specified amount of energy, while calculating the necessary spectrum for this necessary reaction rate. Therefore, since the Beginning of Life (BOL) core is assumed to be fueled by a single material (no enrichment zones, breeding blankets, etc.), the code computes burnup levels that are higher than actually achievable in a batch-mode core. The core lifetime provided by these calculations may be thought of as attainable only via an efficient intra-batch fuel-shuffling scheme.

First, it is useful to establish a reference range for the p/d ratio. The GCFR Demonstration Plant[12] design had a p/d ratio of approximately 1.5, while LMFRs have p/d ratios as low as 1.12[44].

Next, choosing a p/d ratio of 1.3, or about the midpoint of the range of interest, a fuel composition is identified that approaches the reference burnup of 48 $\frac{GWd}{tHM}$ discussed in section 4.3. After compiling in MCNP the geometry described in section 4.3, and testing as the fuel material uranium dioxide (UOX) of diverse enrichments, the initial fuel was settled upon for use in comparing other p/d ratios. It was discovered that UOX enriched 50 w/o in U235, fueling a core with a p/d ratio of 1.3, enables a burnup of 30.8 $\frac{GWd}{tHM}$, which is, for the moment, satisfactorily comparable to that achieved in the reference simulation[13], because it allows further testing of other p/d ratios in the range of interest.

Testing the lifetime of this fuel in depletion calculations with other p/d ratios in the range of interest yielded Figure 7 and Figure 8. The core's End of Life (EOL) is considered to be when the effective neutron multiplication factor, k_{eff}, is reduced to 1.

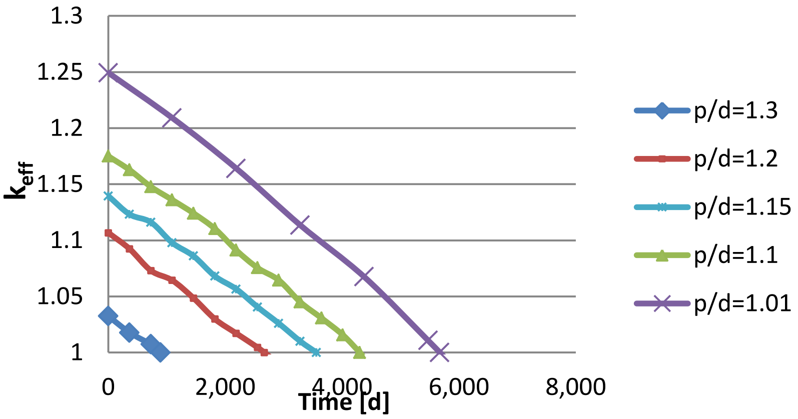

Figure 7. Depletion calculations given a finite mass and volume of UOX fuel (50 w/o U235), arranged in hexagonal lattices with varied spacing.

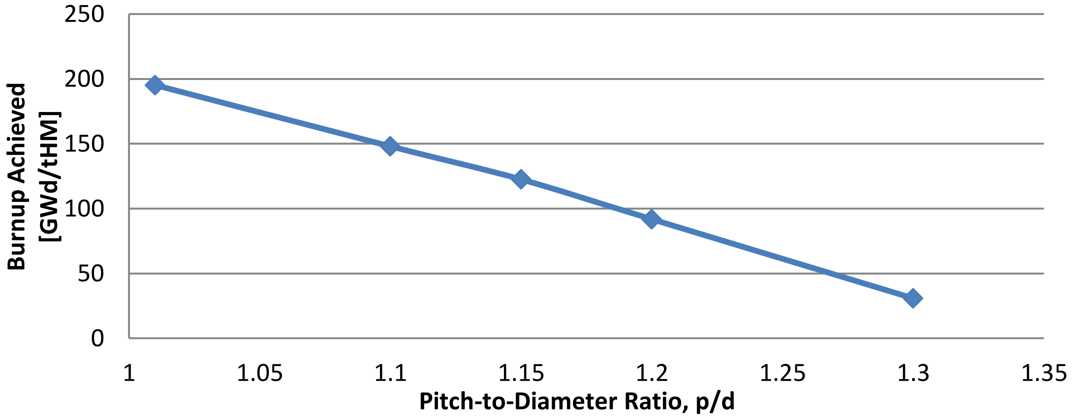

Figure 8. Fuel burnup achieved with a fixed fuel mass and composition, while varying the lattice spacing.

These figures show no diminishing marginal benefit to shrinking the p/d ratio, with respect to criticality, assuming that any initial excess reactivity can be controlled with burnable poisons and control rods. The achievable burnup simply decreases linearly as p/d increases, so it appears that the optimal configuration is one that is as compact as possible. Therefore, the achievable fuel burnup cannot single handedly determine the optimal p/d ratio in this fast reactor. The depletion calculations do, however, incidentally provide a measurement of the average total neutron fluence throughout the reactor's lifetime. The fluence is discussed in section 4.7. The neutron fluence is a limiting factor in the lifetime of components in the core, particularly the cladding[42]. This may provide a clue as to the most practical p/d ratio, since it would be unnecessary and uneconomical to configure the fuel to achieve a burnup beyond what is tolerable by the component with the lowest fluence tolerance.

4.6 Peaking Factors

Using the mesh tally feature of MCNP, the distribution of the BOL total neutron flux was characterized for the three dimensional core. The flux was tallied in a thin radial slice at the axial midpoint of the core. Two additional tallies are conducted in long, thin mesh tally volumes established in fuel subassemblies: one in the centermost fuel subassembly, and one in an outermost fuel subassembly. These three tallies are repeated for several values of the p/d ratio within the range of interest.

The results of the radial mesh tallies are plotted in Figure 9. The color coding indicates the relative magnitude of the total neutron flux in units of $\frac{n}{cm^2 s}$ at each location in the plane sampled. Red denotes the high flux region of the core, which is upward of approximately $7 \times 10^{14} \frac{n}{cm^2 s}$, while blue areas denote approximately $3 \times 10^{14} \frac{n}{cm^2 s}$ and lower. It is noticeable by close visible comparison of the flux maps in Figure 9 that the flux peaking is steepest when the p/d ratio is smallest.

The data from the mesh tallies were also used to estimate the radial power peaking factor, $Fq_{,R}$. $Fq_{,R}$ is assumed to be the same as the radial flux peaking factor, $F_{\emptyset,R}$, if the reactor is at steady state[28], and only when calculated using the fueled region of the core. Excluding the reflector and the central control assembly's slot (which is a flux trap, a high flux region that does not proportionally contribute to heat production) from the peaking factor calculation still provides a conservative estimate, since it only excludes the central control rod assembly slot.

$$F_{q,R} \approx F_{\emptyset,R} = \frac{\emptyset_{max,R}}{\emptyset_{avg,R}} \tag{50}$$

Similarly, the axial power peaking factor can reasonably be inferred from the flux peaking factor, which was calculated using a mesh tally of a thin cylindrical element of the core. In this case, Eq. 51 is adapted from Eq. 50 to be used to calculate the axial peaking factor.

$$F_{q,A} \approx F_{\emptyset,A} = \frac{\emptyset_{max,A}}{\emptyset_{avg,A}} \tag{51}$$

The results of the axial mesh tallies, taken at the radial center and the radial periphery of the core, are plotted in Figure 10.

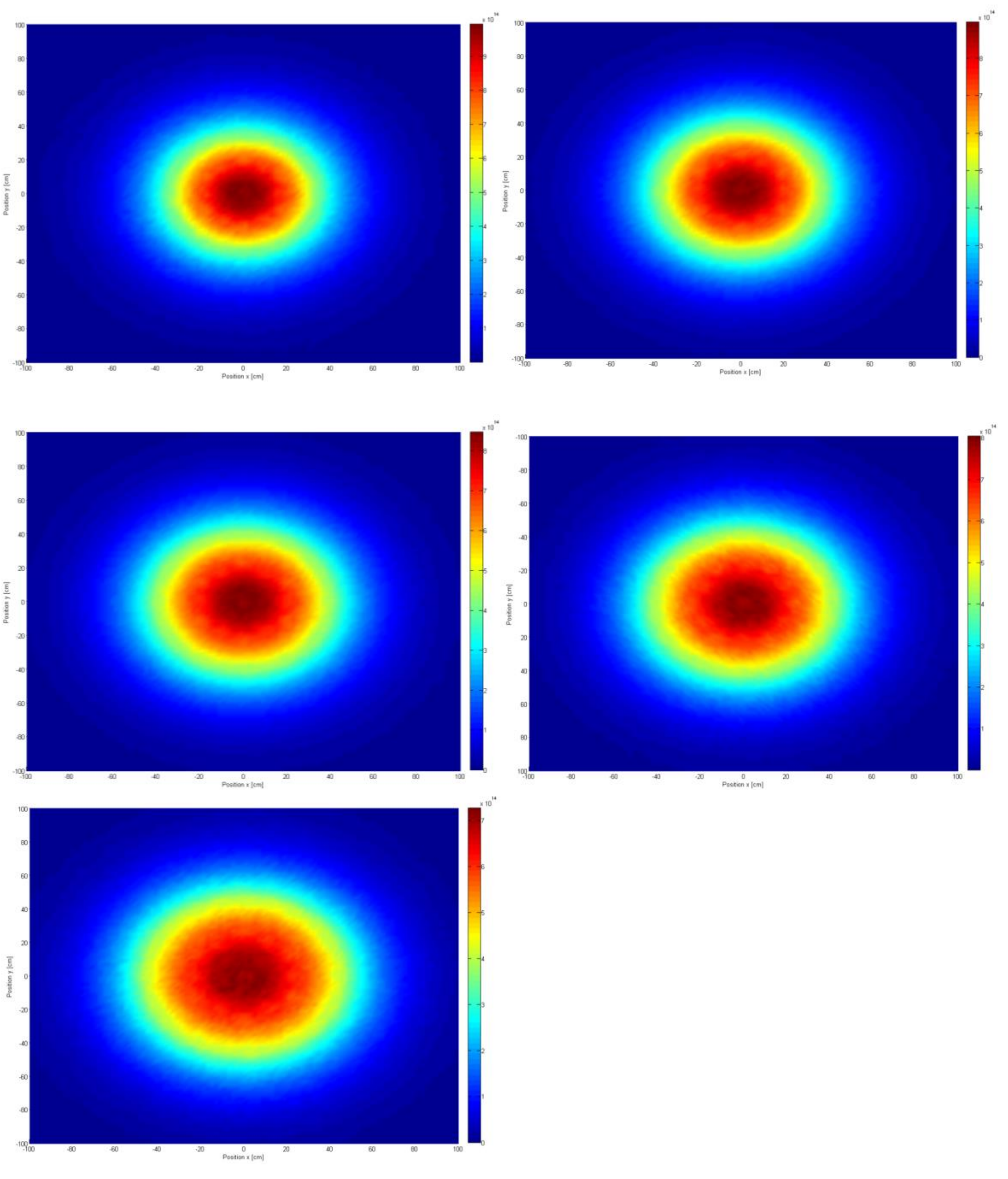

Figure 9. Radial flux profiles of the air-cooled fast reactor with varying pitch-to-diameter ratios. Top left: p/d=1.01. Top right: p/d=1.1. Middle left: p/d=1.15. Middle right: p/d=1.2. Bottom: p/d=1.3.

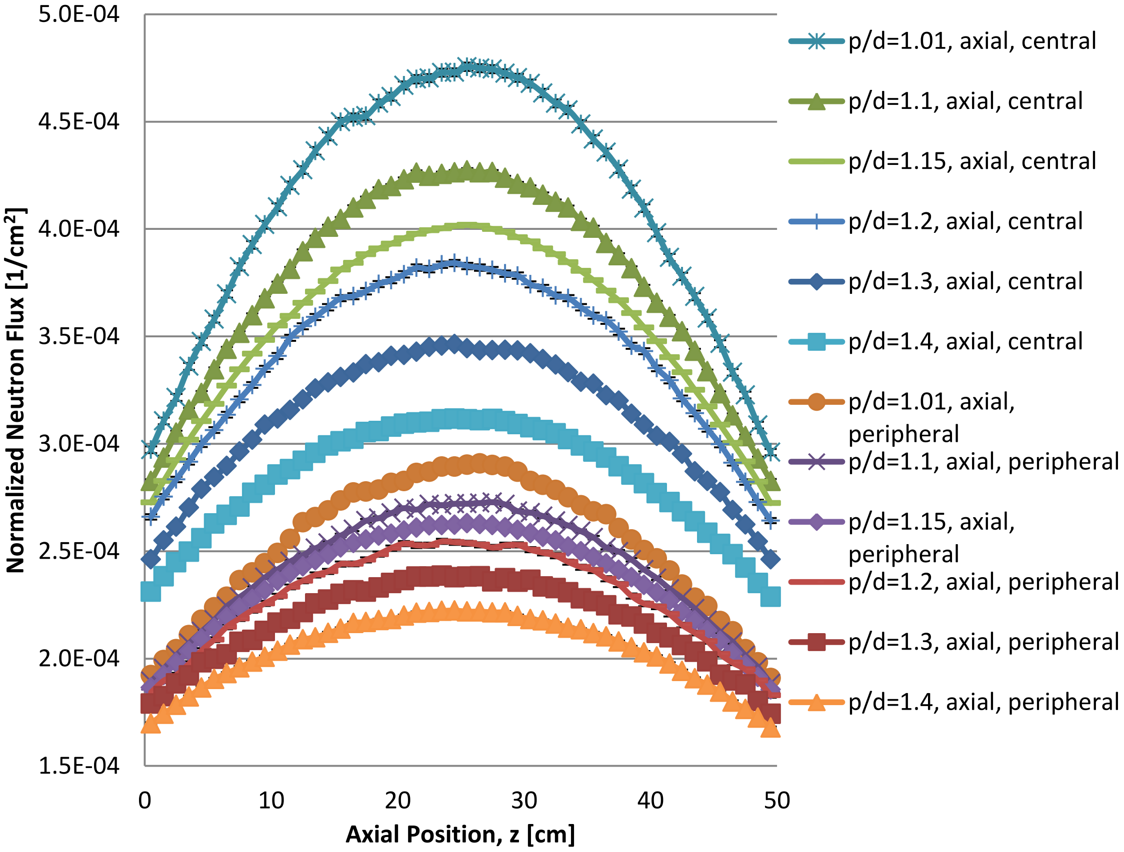

Figure 10. BOL axial flux profiles as tallied at the radial center and periphery of the core, with varied lattice spacing.

Now with a complete collection of radial and axial power peaking factors for the p/d range of interest, Eq. 52 can be used to estimate the total power peaking factor. The agreement between the central and peripheral measurements of the axial peaking factors legitimizes the use of this equation, as does the agreement between calculations of the radial peaking factor at the axial midpoint and the axial top of the core.

$$F_q = F_{q,R} F_{q,A} \tag{52}$$

Figure 11 is a plot of the total peaking factor as a function of the p/d ratio. It shows that the power peaking can be lowered by enlarging the lattice. It also shows that there is a slightly decreasing marginal benefit to enlarging the lattice.

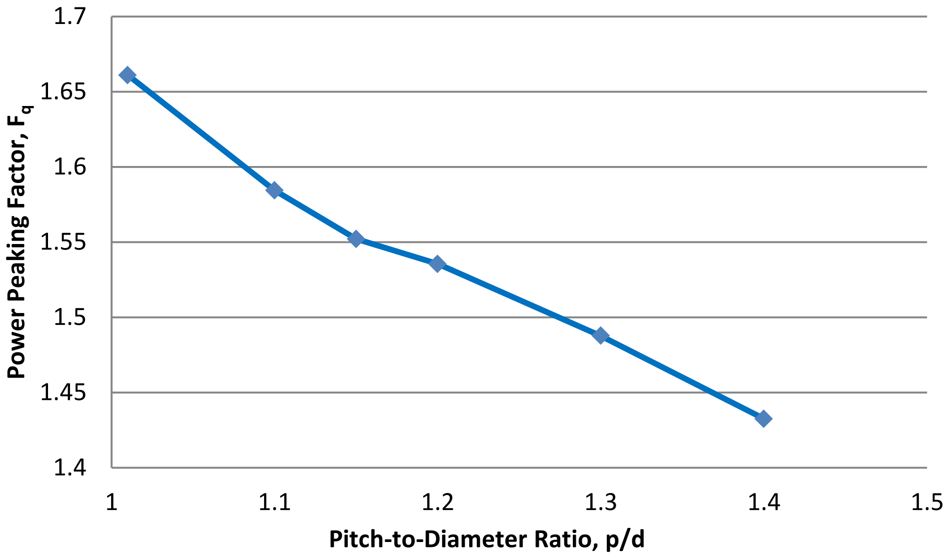

Figure 11. BOL power peaking factor as a function of p/d.

The radial, axial, and total peaking factors calculated using this method are tabulated in Table 3.

Table 3. Variation of BOL Peaking Factors with Lattice Spacing

p/d		Radial at Midpoint	Radial at Top	Central Axial	Peripheral Axial	Total Peaking Factor
1.4	Max Normalized Flux [1/cm^2]	3.17E-04	2.33E-04	3.12E-04	2.22E-04	1.43248
	Average Normalized Flux [1/cm^2]	2.43E-04	1.83E-04	2.84E-04	2.04E-04	
	Peaking Factor	1.3034609	1.270722	1.098978	1.0924956	
1.3	Max Normalized Flux [1/cm^2]	3.53E-04	2.56E-04	3.46E-04	2.39E-04	1.48766
	Average Normalized Flux [1/cm^2]	2.64E-04	1.94E-04	3.11E-04	2.17E-04	
	Peaking Factor	1.3374238	1.318208	1.112333	1.1006258	
1.2	Max Normalized Flux [1/cm^2]	3.91E-04	2.72E-04	3.84E-04	2.55E-04	1.53537
	Average Normalized Flux [1/cm^2]	2.86E-04	2.04E-04	3.42E-04	2.29E-04	
	Peaking Factor	1.3651877	1.334433	1.124655	1.11116	
1.15	Max Normalized Flux [1/cm^2]	4.12E-04	2.82E-04	4.02E-04	2.63E-04	1.55198
	Average Normalized Flux [1/cm^2]	3.00E-04	2.09E-04	3.55E-04	2.36E-04	
	Peaking Factor	1.3728914	1.344279	1.130447	1.1158455	
1.1	Max Normalized Flux [1/cm^2]	4.36E-04	2.87E-04	4.27E-04	2.73E-04	1.58431
	Average Normalized Flux [1/cm^2]	3.13E-04	2.14E-04	3.76E-04	2.43E-04	
	Peaking Factor	1.3947408	1.343909	1.135916	1.1248242	
1.01	Max Normalized Flux [1/cm^2]	4.83E-04	3.06E-04	4.76E-04	2.91E-04	1.66096
	Average Normalized Flux [1/cm^2]	3.36E-04	2.20E-04	4.12E-04	2.53E-04	
	Peaking Factor	1.4373352	1.386786	1.155583	1.1487149	

4.7 Neutron Fluence

Estimation of the lifetime fast fluence in the reactor in this design includes two significant assumptions. The first is that the fast fluence percentage remains constant throughout the core lifetime; i.e.: the shape of the spectrum remains constant, and only the magnitude increases to maintain the rated power level. This is a liberal assumption, since the spectrum actually changes over the core lifetime to accommodate plutonium production and U235 depletion[3], as indicated by Figure 12.

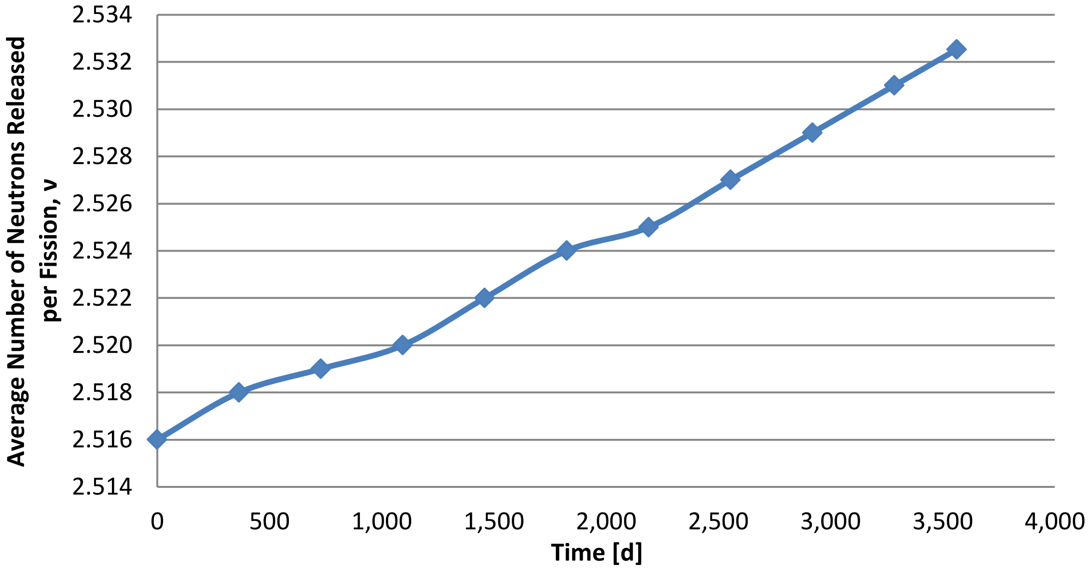

Figure 12. Change in the number of fission neutrons released per fission throughout the core lifetime, via MCNP depletion calculation.

This assumption is only justified if this calculation demonstrates that the fuel burnout determines the EOL of the core while the fluence is still up to an order of magnitude below the cladding fluence limit, which outweighs any spectral shifting that occurs in the core's lifetime. The second assumption is that the cladding itself has negligible bearing on the lifetime fluence of the reactor. This assumption is validated by a MCNP simulation demonstrating that only a slight spectral shift occurs when Zircaloy is replaced with SiC, as shown in Figure 13.

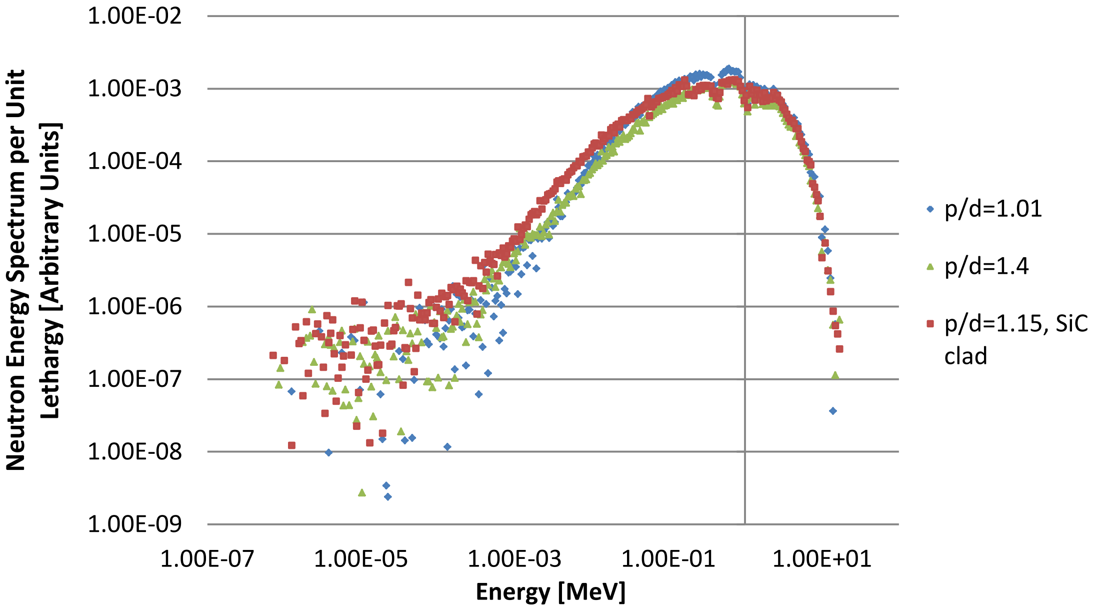

Figure 13. Comparison of neutron spectra of the core with Zircaloy and SiC cladding.

The magnitude of the total flux was calculated by MCNP at each time step in the depletion calculations described in section 4.5, and these are used to calculate the neutron fluence. The average total fluence is calculated using Eq. 53, in which the fluence at any point in the core's lifetime is the summation of the fluences at each time step up to the current, *i*th, time step.

$$\Phi_{avg,tot} = \sum_{i}^{EOL} \emptyset_i \, \Delta t_i \tag{53}$$

Clearly, smaller, more numerous time steps would provide greater precision, since this equation is a discretization of the true integral relationship between fluence and the continuous changing of the flux over time. The use of as few as 3 to 12 time steps (of 365 to 1095 days each) for this calculation is necessary because of the long computational time for MCNP depletion calculations and is justified in that the magnitude of the flux only changes by a factor of 1.54 or less throughout the core lifetime.

While Eq. 53 can be used to identify the average neutron fluence over the lifetime of the reactor, it is truly the fast fluence that limits the useful lifetime of the cladding, since thermal and epithermal neutrons cause negligible damage to the molecular structures of the cladding[45]. Additionally, if the core is operated in batch mode with no fuel shuffling, it is not the average fast fluence that limits the core's structural integrity, but the peak fast fluence, which occurs near the center of the core. The peak fast fluence for a batch-mode core is given by

$$\Phi_{pk,fast} = \Phi_{avg,tot}\, f_{ff}\, F_q \tag{54}$$

The peak fast fluence of a core with a highly effective radial fuel shuffling scheme is given by

$$\Phi_{pk,fast} = \Phi_{avg,tot}\, f_{ff}\, F_{q,A} \tag{55}$$

The peak fast fluence is calculated using the total power peaking factor, given by Eq. 52[46], which uses the radial and axial peaking factors calculated in section 4.6.

The fast fluence fraction, f_{ff}, was calculated for each p/d ratio case using the spectral data that produced Figure 6. Useful values of f_{ff} are compiled in Table 4.

Table 4. BOL Fast Fluence Fractions for Several p/d Ratios

p/d	**Flux fraction >0.1MeV**	**Flux fraction >1MeV**
1.01	0.799833	0.227338
1.1	0.803729	0.232912
1.15	0.803858	0.235466
1.2	0.805931	0.23705
1.3	0.808327	0.244744

The fluence limits for the cladding choices considered here are subjects of ongoing study[45,10,47]. For the purpose of this design, values are taken from scholarly accounts of experimental research, although there are few claims made that any specific value of fluence should be taken as the absolute upper limit for any specific cladding materials. The neutron fluence limit for Zircaloy is taken as $1.2 \times 10^{22} \frac{n}{cm^2}$, for neutron energies above 1 MeV[45]. For Inconel, it is taken as $1.8 \times 10^{23} \frac{n}{cm^2}$, for energies above 0.1 MeV[47]. For H9 Steel, it is taken as $4.0 \times 10^{23} \frac{n}{cm^2}$, for energies above 1 MeV[42]. For silicon carbide (SiC), the fluence limit is taken as $3.2 \times 10^{24} \frac{n}{cm^2}$ for energies above 0.1 MeV[42]. To be conservative, in this design, all of these limits are considered the limits for neutron energies above 0.1 MeV, as opposed to 1 MeV. This is because these values are likely to have been determined with a thermal spectrum in mind. In a thermal spectrum, a small portion of the spectrum exists between 0.1 MeV and 1 MeV, whereas in a fast spectrum, nearly half of the spectrum exists in this range, as evidenced by Table 4.

Performing these lifetime fluence calculations using Eq. 55 and the flux data from the MCNP depletion calculation led to Figure 14. This assumes that the burnup achieved in the MCNP calculation is achievable using only a radial fuel shuffling scheme.

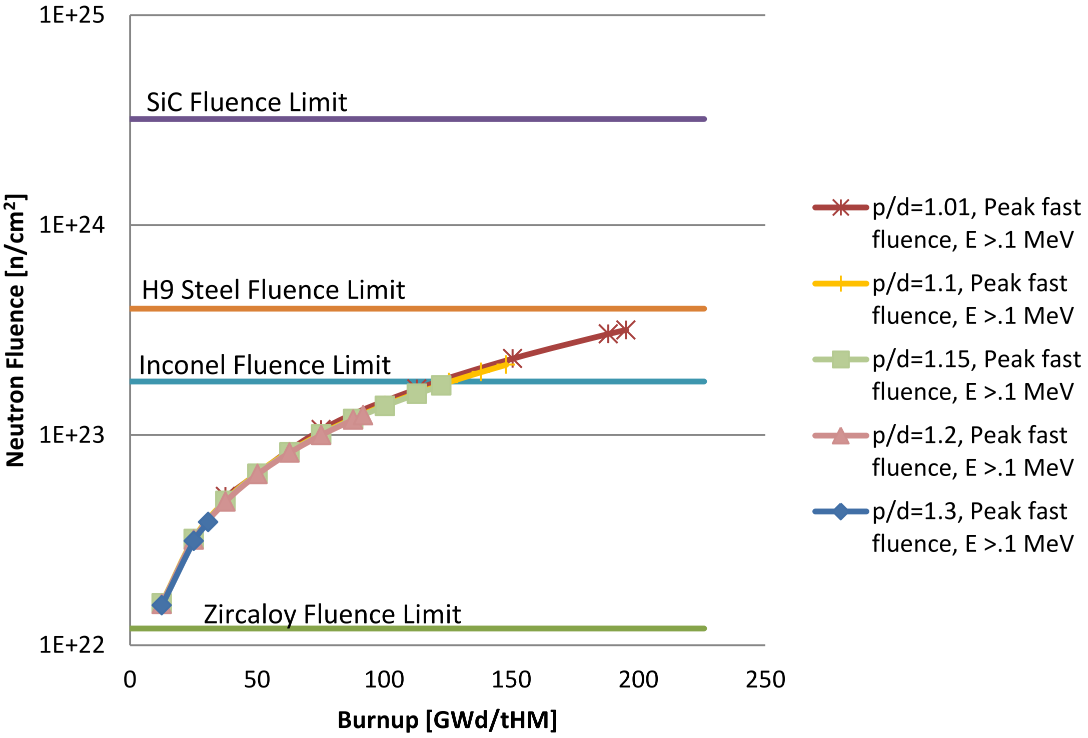

Figure 14. Neutron fluence over the core lifetime of the air cooled fast reactor.

An alternate way of viewing the fluence of the reactor is in terms of the neutron multiplication factor, k_{eff}, as shown in Figure 15.

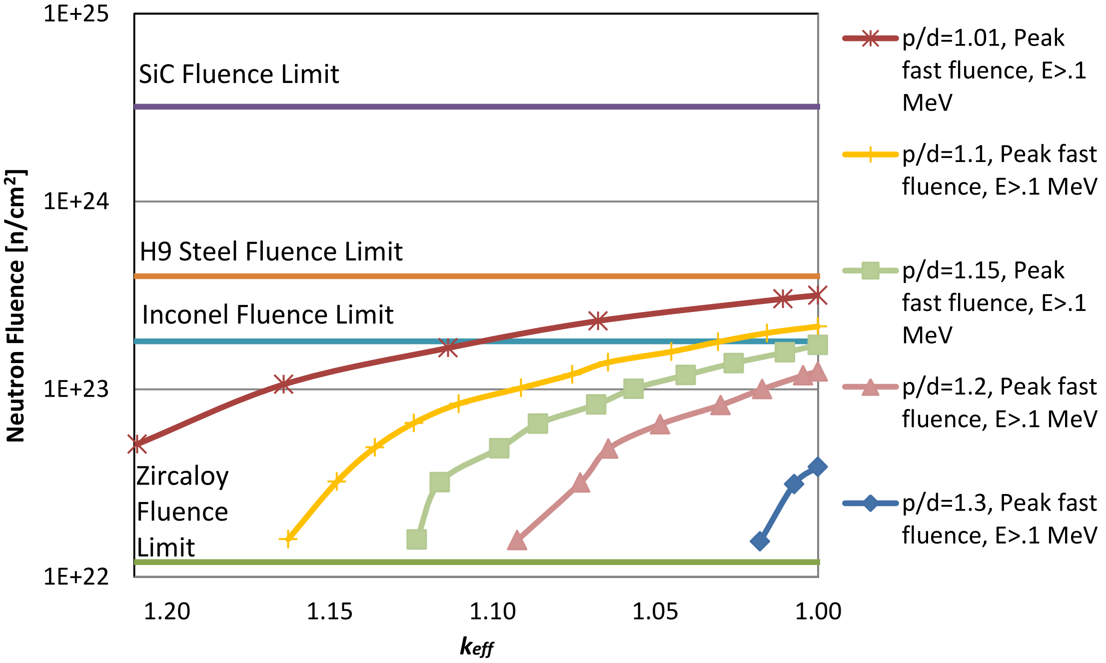

Figure 15. Neutron fluence as a function of k_{eff}.

Clearly, Zircaloy must be eliminated as a choice of cladding, since it cannot tolerate even the minimal neutron fluences considered in this design. Both steel and SiC are able to withstand the neutron fluence regardless of the p/d ratio considered. A combination of Inconel cladding and p/d=1.15 would be economical in that the fuel burnout would occur when the cladding at the axial midpoint has reached approximately 96% of its fluence limit.

4.8 Direct, Open Cycle and the Argon-41 Problem

One of the chief benefits of an air-driven Brayton cycle is the possibility of a direct, open cycle. Obviously, when the working fluid in a Brayton cycle is helium, the loop must be closed in order to preserve the finite supply of helium. This necessitates the pumping of the heat sink fluid through a heat exchanger in order to cool the helium for recycling through the reactor. This limits the thermodynamic efficiency of the system, because the heat exchanger requires some amount of power in order for the heat sink fluid to move through it. If a system were to use air, which is essentially in infinite supply, and is already at a low ambient temperature, and then exhaust the heated air after it is used to drive the turbine, there would be no need for the pumping of the heat-sink air. The atmosphere would supply abundant coolant at a low temperature, while simultaneously serving as an infinite heat sink in which to diffuse and dissipate the exhaust air.

The environmental impact of the exhaust is a concern that must be addressed, especially when the exhaust has been used to cool nuclear fuel. First, the heat sink must be able to accept the heat of the exhaust without changing the overall heat sink temperature to the detriment of surrounding ecosystems. This is a reasonable assumption, since the entire atmosphere is available to dissipate heat. Next, a reactor with such a cooling scheme must exhibit reliably high retention of fission products. Experiments have been conducted demonstrating fuel element designs that retain all but a negligible portion of their fission products[48]; however, this report does not claim to simulate accurately the composition or geometry of these fuel element designs. In order to maintain a narrow focus on the feasibility of using air as a coolant in a direct, open cycle, it is assumed here that the exhaust has negligible fission product content. Finally, since the exhaust is subjected to a neutron flux, the effects of activation products in the coolant must be analyzed. Not modeled here, but easily conceivable, is a scheme in which particulates and moisture are removed from the air both before and after irradiation. This is assumed here because otherwise, additional concerns arise from the possible neutron interactions with impurities in the air. Even with filtering, certain nuclides in the air will become activated when exposed to a neutron flux.

The main activation product of interest for the case of an air-cooled reactor is Argon-41[49]. Because Ar-41 decays with a half-life of 1.822 hours, it does not pose a persistent environmental concern, especially if the reactor is located long distances from population centers. But the constant production of Ar-41 poses a health and safety concern for people living and working around this reactor. The half-life is too long to devise a scheme of detaining the air until the Ar-41 has decayed before exhausting it. It should be noted that there exists no suitable industrial process for removing argon from the air either before or after irradiation. Current processes for isolating argon from the air are both energy intensive and space intensive[50].

The production rate of Ar-41 is assumed to be equal to the neutron capture rate of Ar-40 in the reactor, and is estimated as follows[2].

$$R_{Ar41}\left[\frac{Bq}{s}\right] = \frac{w}{\rho_b}\left(N_{Ar40}\sigma_{\gamma,Ar40}\emptyset\right)\left(\frac{H}{v_b}\right)a_{Ar41} \tag{56}$$

Here, N_{Ar40}, is the number density of Argon-40 in the air, which is calculated using the natural Ar-40 mass fraction in air, which is taken as 1.28%[18]. The neutron capture cross section, $\sigma_{\gamma,Ar40}$, for Ar-40 is taken as the fission spectrum average cross section listed in Table 1. The specific activity of Ar-41, a_{Ar41}, is taken as 1.591×10^{18} Becquerels per gram[51]. The average scalar flux, $\emptyset$, used in this calculation is that determined via MCNP for the EOL core. This provides a conservatively high estimate of the Ar-41 production rate, since the flux increases from BOL to EOL.

The equilibrium activity, A_{Ar41}, of the Ar-41 exhausted from the reactor is found by solving the following ordinary differential equation[28], in which λ_{Ar41} is the decay constant for Ar-41, which is $1.0566\text{E}-4\ s^{-1}$.

$$\frac{dA_{Ar41}}{dt} = R_{Ar41} - \lambda_{Ar41}A_{Ar41} \qquad (57)$$

The solution to this equation is as follows.

$$A_{Ar41} = \frac{R_{Ar41}}{\lambda_{Ar41}}\left(1 - e^{-\lambda_{Ar41}t}\right) \qquad (58)$$

The equilibrium activity of the Ar-41 in the exhaust may then be used in combination with a normalized dose equivalent tallied in a MCNP calculation, in order to find the dose rate a person would receive in various situations. In this case, a flux tally is modified using the ANSI/ANS 6.1.1-1977 dose function for photons[25].

One of the simplest, albeit unrealistic, situations to model is that of the Ar-41 accumulating as a point source at the exhaust point. Approximating an average human being as a cylinder of water with a height of 1.69 m and a mass of 62 kg, one can tally in MCNP the normalized dose equivalent received by a person at any distance from the point source. Then, linking this to the thermal-hydraulic model (discussed in sections 3.3.2 above and 4.9 below), this normalized dose equivalent can be used to estimate the true dose equivalent due to Ar-41, given the point-source assumption.

The results were calculated using the most efficient open cycle parameters modeled in section 4.10 of this thesis. In this calculation, the p/d ratio is 1.15; the core inlet temperature is assumed to be 296 K; the inlet pressure is 6.5 atm; and the limiting temperature[7] is the peak SiC cladding temperature of 1173 K. The system of equations that was explained in section 3.3.3 yielded that these conditions necessitate a mass flow rate of 100.8 $\frac{\text{kg}}{s}$ through the core. When this mass flow rate of air is subjected to a fast neutron flux of $6.889E14\ \frac{n}{cm^2 s}$ (the EOL flux for the case of p/d=1.15), per Eq. 56, the Argon-41 production rate is $2.00\text{E}11\ \frac{atoms\ Ar-41}{s}$. Then, per Eq. 58, the equilibrium activity for Ar-41 in the exhaust cloud is $2.00\text{E}11$ Bq. This activity, being used to de-normalize dose rates calculated in MCNP for a point source emitting gamma rays at 1.284 MeV (the average energy of Ar-41's characteristic decay photons), results in the dose rates plotted in Figure 16. This figure assumes that the Ar-41 accumulates at waist level, and that the human subject is exposed to the source for one whole year with only atmospheric air to shield the gamma radiation. According to this plot, the person would have to stand approximately 100 m away from the Ar-41 source in order to remain below 0.05 $\frac{Sv}{yr}$, which is the total dose limit imposed by the Nuclear Regulatory Commission[52]. This assumes that the person's entire annual dose is solely due to Ar-41. If this were a realistic model, it could not be considered acceptable, because people must be permitted to work in close proximity to the reactor system.

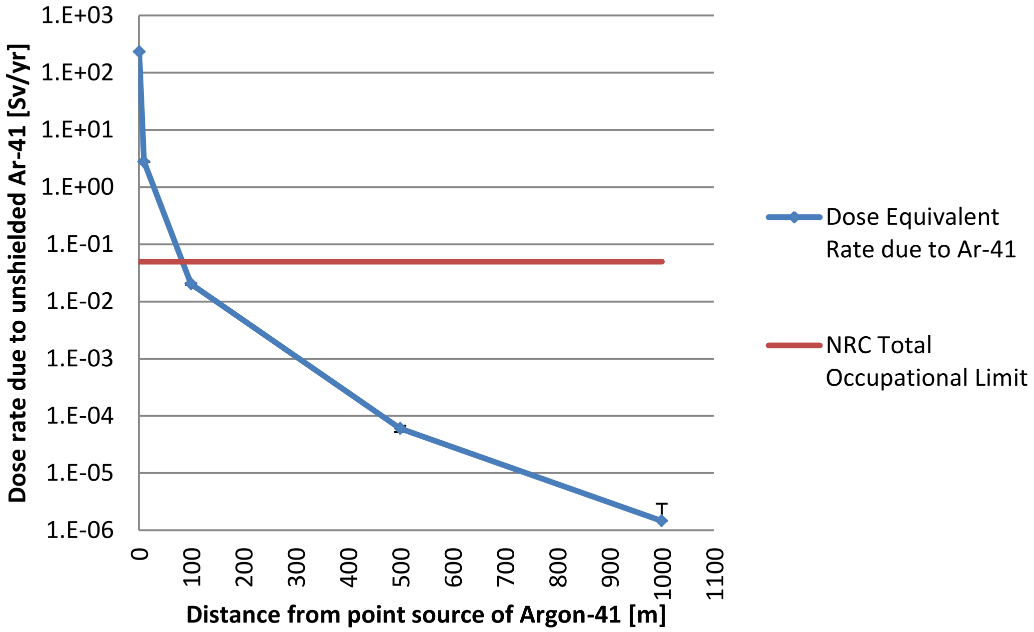

Figure 16. Dose rate to a person standing exposed to a hypothetical point source consisting of all Ar-41 produced by an air-cooled fast reactor.

Another model has the Ar-41 being driven linearly away from the exhaust point, with a wind speed of 2 $\frac{m}{s}$, so that the steady state activity is 1.80E6 Bq per meter distance from the exhaust point. For this problem, it is assumed that the concentration of Ar-41 does not diminish with distance due to decay. This is reasonable when coupled with the assumption that a person at the reactor site receives negligible dose from Ar-41 that has travelled a certain distance away from the reactor. In this case, given the low dose rate received from a concentrated point source 1000 m away, it is assumed that a person receives no dose from a linearly distributed source beyond 1000 m. The result after de-normalizing the MCNP tally is that a person standing at the exhaust point, while the wind carries the exhaust away at a constant 2 $\frac{m}{s}$, receives $0.00959 \pm 6.71E-6\ \frac{Sv}{yr}$

due to Ar-41 alone. This is less than 20% of the total occupational dose limit. The Ar-41 dose rate would be brought to 0.05 $\frac{Sv}{yr}$ if the wind speed were as low as 0.39 $\frac{m}{s}$.

Yet a third way to characterize the Argon-41 activity due to the open cycle AGFR is to make the liberal assumption that Ar-41, once it leaves the exhaust point, dissipates so quickly that it does not contribute to the dose rate. The assumption might then be that only the activity at the exhaust point itself contributes to the dose rate. As evidenced by Eq. 58, Argon-41 does not achieve equilibrium activity inside the reactor. Equilibrium activity can only be described for the exhaust cloud as it accumulates several hours after the startup of the reactor. However, since there is a constant production rate of Ar-41, the instantaneous activity of Ar-41 at the exhaust point can be known by simply solving Eq. 58, where time, t, is equal to the exposure duration of the air to the neutron flux. That is, the Ar-41 activity at the exhaust point is given by Eq. 58, where $t = \frac{H}{v_b}$. In this case, for the open cycle described above, the exposure duration is 0.015 seconds, which corresponds to an activity of $3.08E5\ Bq$ at the exhaust point. As evidenced by Figure 17, a person could stand arbitrarily close to such a point, and receive a dose within regulatory limits.

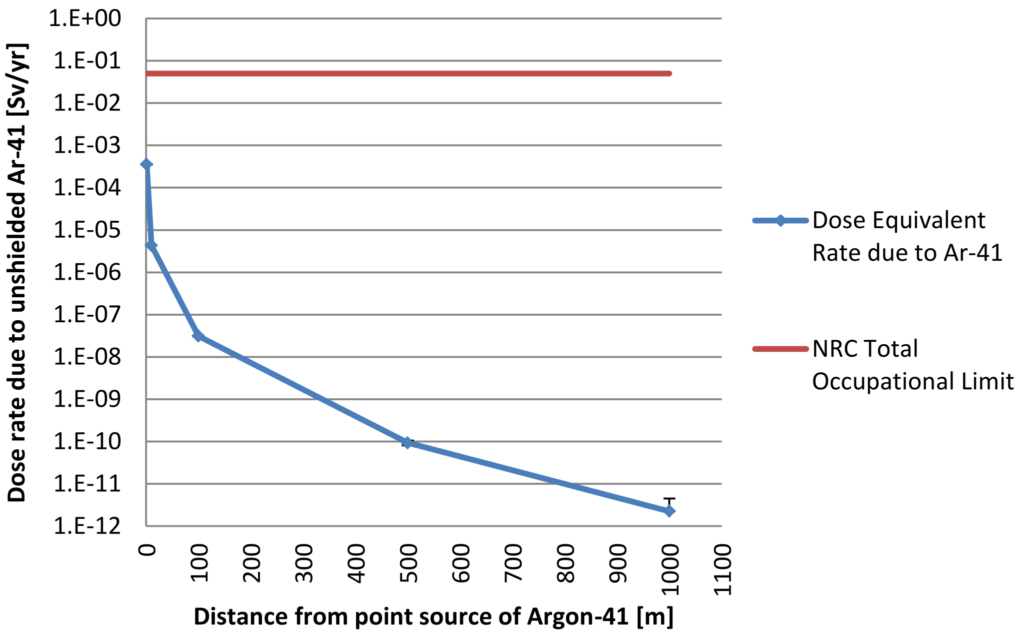

Figure 17. Dose rate to a person due to Ar-41 at the exhaust point only, assuming no contribution from the exhaust cloud.

Although the hypothetical scenario of the entire open cycle exhaust cloud aggregating as a point source is extremely conservative, it may in fact be more realistic for the closed cycle, assuming that the primary coolant circuit can be treated as a point source. Eqs. 56-58 contain the assumption of a constant rate of exposure of Ar-40 to the neutron flux, because in an open cycle, fresh air flows continuously into the reactor with its natural abundance of Ar-40. In a closed cycle, however, Ar-40 would be subject to depletion. Modifying Eqs. 56-58 to account for such depletion, however, produced Figure 18, which shows that the effect of Ar-40 depletion would have little bearing on the total activity of Ar-41 until several orders of magnitude of time beyond the reactor's core lifetime. Since an equilibrium Ar-41 activity is reached within one day of operation, it may indeed be appropriate to consider the closed-cycle AGFR a constant source of gamma radiation due to Ar-41. This poses a significant radiation concern similar to that described for the hypothetical point-source exhaust cloud for the open cycle. When modeled with the closed cycle design parameters recommended in section 5 of this thesis, the equilibrium activity of Ar-41 is 7.11E9 Bq for every multiple of the irradiated coolant volume contained within the primary loop. This means that if the primary coolant loop is, for example, effectively 30 times as long as the active core, then the equilibrium activity of Ar-41 would be 30 times 7.11E9 Bq.

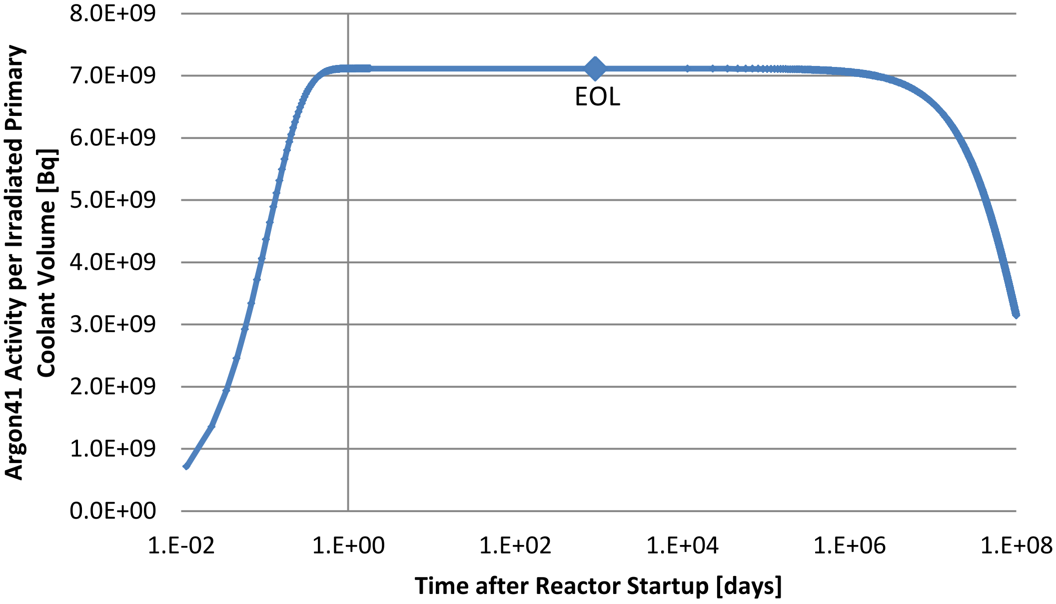

Figure 18. Argon-41 activity in the closed-cycle AGFR.

While these calculations demonstrate that people could potentially operate an open-cycle air-cooled fast reactor while receiving a survivable (albeit unauthorized) dose via Argon-41 production, there is some literature regarding the release of radioactive noble gasses from nuclear facilities. The historical statutory limit, or Derived Release Limit, for the Pickering Nuclear Generation Station[53] in Canada was 191,000 $\frac{TBq-MeV}{yr}$. Although this power plant typically released less than 1% of this annual limit, the Derived Release Limit had been the result of a study showing that a member of the public nearest to the facility would receive a dose equal to the occupational exposure limit. That a single nuclear generation station could release 191,000 $\frac{TBq-MeV}{yr}$ of radioactive noble gasses before the public receives the statutory dose limit for nuclear workers seems to corroborate the above assessment that the AGFR would not provide a harmful dose. If the AGFR produces Ar-41 at a rate of 2.16E7 $\frac{Bq}{s}$, and the average decay gamma has an energy of 1.284 MeV, then it produces 877 $\frac{TBq-MeV}{yr}$.

The comparison between the AGFR's 877 $\frac{TBq-MeV}{yr}$ of Ar-41 with Pickering's 191,000 $\frac{TBq-MeV}{yr}$ limit for noble gasses is not a direct comparison. Pickering's noble gas release occurs at the tops of tall, permanent stacks. Pickering's actual releases were never higher than 17% of the DRL, and were steadily measured at approximately 0.2% of DRL from 1974 to 1986. Pickering also had a power rating of 4336 MWe, compared to the AGFR's 30 MWth. If the AGFR were 40% efficient, it would produce Ar-41 at a rate of 73.1 $\frac{TBq-MeV}{yr-MWe}$, compared to Pickering's normalized DRL of 44.05 $\frac{TBq-MeV}{yr-MWe}$, and Pickering's average actual release rate of 0.0458 $\frac{TBq-MeV}{yr-MWe}$. Therefore, in normalized terms, the AGFR produces far more radioactive noble gasses than a typical power plant, although the levels are still arguably to remain safe and within regulatory limits. The stated purpose of this reactor for use in remote locations may help the case for accepting higher rates of noble gas release.

4.9 In-Core Heat Transfer

After developing the analysis package described in section 3.3.3, it was used to analyze the performance of the coolant air at various combinations of power output and flow regime. The p/d ratio was also varied, as was the inlet temperature for a comparison of the open and closed cooling regimes for steady operation as well as the DLOCA scenario. Table 5 and Table 6, on the following pages, show the resulting data sets for post-DLOCA decay heat removal for closed and open thermodynamic cycles respectively. The closed post-DLOCA cycle has the advantage of retaining a greater portion of the fission products, while the open post-DLOCA cycle has the advantage of using the low-temperature ambient air to cool the endangered core. Note that for both the open and closed Brayton cycles considered for this design concept, an emergency bypass system would be required in order to pump ambient air directly from the compressor to the core, bypassing the recuperator. For this calculation, the closed cycle is assumed to maintain a core inlet temperature of 596 K, the Gen-IV GFR reference value[12], except the pressure is reduced to 1 atm. These data sets are for the case of SiC cladding, although the code also solves for the cases of Zircaloy, stainless steel, and Inconel simultaneously. These data are useful in determining an acceptable, if not optimal, combination of p/d ratio and thermodynamic cycle. The choice must also be balanced with burnup estimates from the neutronics section, although the reasons for stopping short of an arbitrarily small p/d ratio are purely related to the thermal hydraulics of the system.

These data contain the conservative assumption of zero thermal inertia in the system, both at operating conditions and DLOCA conditions. This means that the coolant velocities and pumping powers shown are those absolutely required to maintain safe material temperatures. For every data point here, the peak cladding temperature is the limiting parameter. The peak cladding temperature for each case was determined using the peaking factors calculated in section 4.8.

There are many noteworthy trends in these data. One is the counterintuitive observation that smaller coolant channels enable a greater heat removal rate than larger coolant channels, even if the mass flow rate is the same. Given that a greater fuel burnup is achieved with a smaller p/d ratio, one may wish to minimize the pitch-diameter ratio. However, there are several factors preventing this. As the p/d ratio shrinks, the superficial fluid velocity needed becomes large. While the necessary coolant velocity does not appear to approach its limit (i.e.: Mach-1) when the DLOCA is followed immediately by a proper SCRAM, the power required to pump the coolant even at an appreciable fraction of the sound speed may become prohibitive, or at least not conducive to any semblance of passive safety. Figure 19 demonstrates this. Notice that a p/d ratio of 1.01 requires between 12 and 2000 kW in the first 2.4 hours after the SCRAM. Additionally, as the p/d ratio becomes small, the assumption that treats the channel as a heated cylindrical pipe loses validity, because local hot spots would be created in the channel where the fuel elements are nearly touching each other.

Table 5. DLOCA Modeling Results of Closed, Direct Cooling

p/d	Pressure [atm]	Heat Production [W]	Fraction of original steady state power	Time after SCRAM [d]	w per channel [kg/s]	max coolant velocity [m/s]	Pumping Power required to overcome friction in core [W]	Avg. ΔT_b [K]	Avg. $T_{b,out}$ [K]
1.01	1	3.00E+04	0.001	50	5.647E-06	4	8.270E+01	659	1255
1.01	1	1.50E+05	0.005	1	2.846E-05	20	2.229E+03	653	1250
1.01	1	3.00E+05	0.01	0.1	5.751E-05	40	1.198E+04	647	1243
1.01	1	2.10E+06	0.07	0	4.626E-04	296	2.315E+06	563	1159
1.01	1	3.00E+07	1	0	6.233E-03	4105	2.805E+09	597	1193
1.01	90	3.00E+07	1	n/a	6.233E-03	46	3.466E+05	597	1193
1.1	1	3.00E+04	0.001	50	5.403E-06	1	4.200E+00	688	1284
1.1	1	1.50E+05	0.005	1	2.760E-05	7	1.080E+02	674	1270
1.1	1	3.00E+05	0.01	0.1	5.670E-05	14	5.900E+02	656	1252
1.1	1	2.10E+06	0.07	0	5.340E-04	117	1.569E+05	488	1084
1.1	1	3.00E+07	1	0	6.980E-03	1586	1.799E+08	533	1129
1.1	90	3.00E+07	1	n/a	6.980E-03	18	2.248E+04	533	1129
1.15	1	3.00E+04	0.001	50	5.301E-06	1	1.707E+00	702	1298
1.15	1	1.50E+05	0.005	1	2.727E-05	5	4.105E+01	682	1278
1.15	1	3.00E+05	0.01	0.1	5.663E-05	10	2.265E+02	657	1253
1.15	1	2.10E+06	0.07	0	5.340E-04	84	6.012E+04	488	1084
1.15	1	3.00E+07	1	0	7.499E-03	1191	8.047E+07	496	1092
1.15	90	3.00E+07	1	n/a	7.499E-03	13	1.022E+04	496	1092
1.2	1	3.00E+04	0.001	50	5.250E-06	1	9.015E-01	708	1304
1.2	1	1.50E+05	0.005	1	2.725E-05	4	1.980E+01	683	1279
1.2	1	3.00E+05	0.01	0.1	5.723E-05	8	1.100E+02	650	1246
1.2	1	2.10E+06	0.07	0	5.340E-04	65	2.832E+04	487	1083
1.2	1	3.00E+07	1	0	8.150E-03	968	4.550E+07	457	1053
1.2	90	3.00E+07	1	n/a	8.150E-03	11	5923	457	1053
1.3	1	3.00E+04	0.001	50	5.110E-06	1	4.046E-01	728	1324
1.3	1	1.50E+05	0.005	1	2.694E-05	3	6.700E+00	690	1286
1.3	1	3.00E+05	0.01	0.1	5.797E-05	5	3.610E+01	642	1238
1.3	1	2.10E+06	0.07	0	5.392E-04	44	8.973E+03	483	1079
1.3	1	3.00E+07	1	0	9.500E-03	7.130E+02	2.002E+07	391	987
1.3	90	3.00E+07	1	n/a	9.500E-03	8	2.828E+03	391	987
1.4	1	3.00E+04	0.001	50	4.939E-06	0	2.685E-01	753	1349
1.4	1	1.50E+05	0.005	1	2.648E-05	2	3.210E+00	702	1298
1.4	1	3.00E+05	0.01	0.1	5.852E-05	4	1.604E+01	636	1232
1.4	1	2.10E+06	0.07	0	5.844E-04	34	4.306E+03	446	1042
1.4	1	3.00E+07	1	0	1.096E-02	573	1.128E+07	339	935
1.4	90	3.00E+07	1	n/a	1.096E-02	6	1.804E+03	339	935

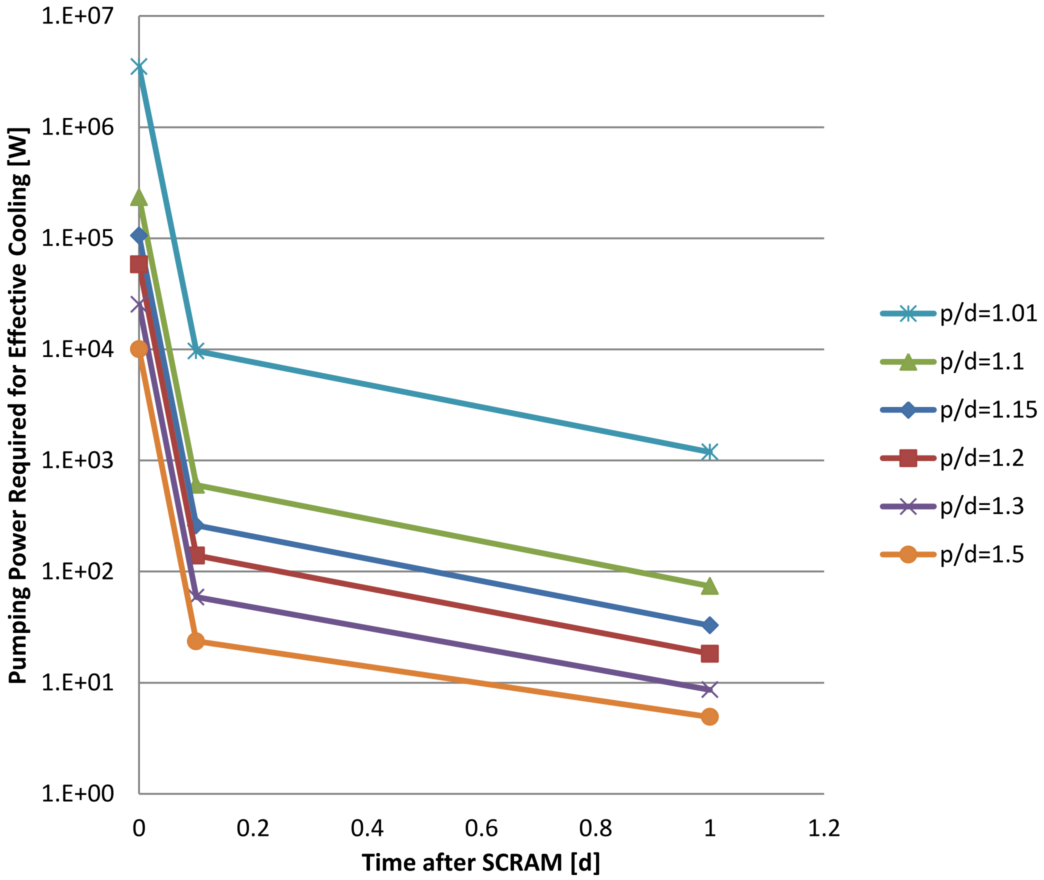

Figure 19. Effect of p/d ratio on short term closed-cooling after SCRAM from 30 MW.

This is informative about the relationship between coolant flow and the effective channel size, but it does not present an obvious optimal channel size. This becomes more evident when comparing the cooling capability of each channel size for a fixed power output. Figure 20 compares the pumping burden for each channel size for the case of normal full-power operation at 30 MW and a system pressure[12] of 90 atm, as well as the case of a DLOCA, when decay heat has reached 1% of the original 30 MW, which takes approximately 2.4 hours after the SCRAM[26]. Comparing these two cases separately, and on linear scales, produces Figures 21 and 22.

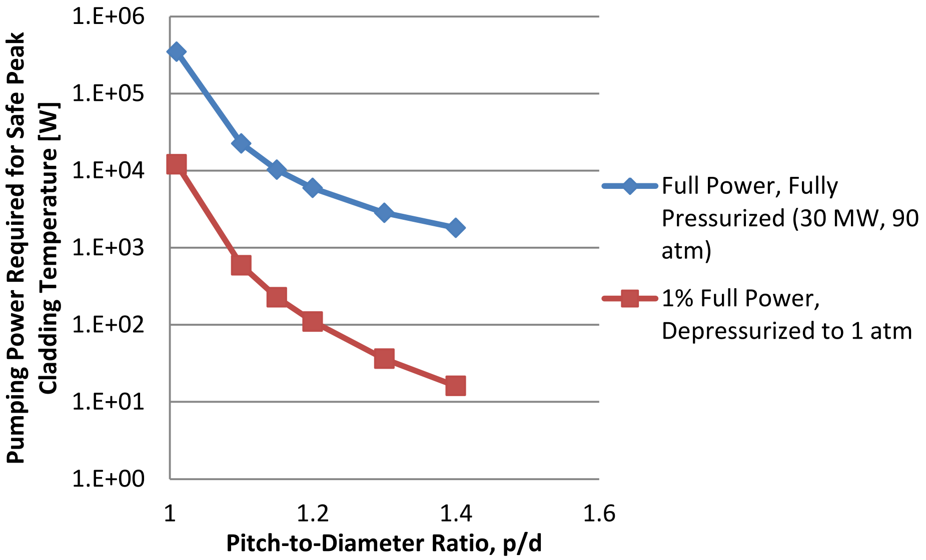

Figure 20. Pumping power required for closed-cycle operation.

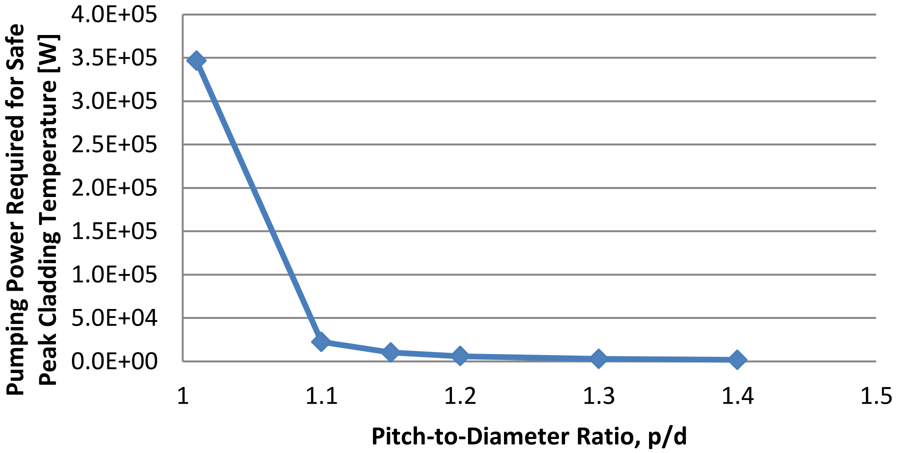

Figure 21. Pumping power required for normal closed-cycle operation.

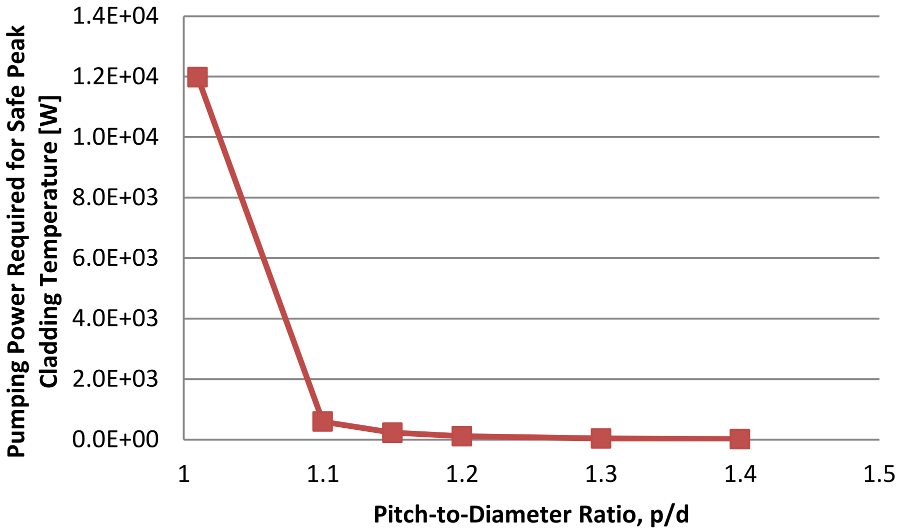

Figure 22. Pumping power required for 1% full power decay heat, following DLOCA, closed-cycle operation.

This does begin to assist with choosing an optimal p/d ratio. It would be economical to reduce the p/d ratio to between 1.1 and 1.2, just before the required pumping power begins to increase dramatically with marginal decreasing of the coolant channel size. That is, as long as that pumping power can be guaranteed for the case of a DLOCA.

These calculations are repeated for the case of open cooling, which is intended to model the capability of the system to maintain safe cladding and fuel temperatures using ambient air directly, in the case of a DLOCA. The sole difference in the calculations is that the inlet air temperature is reduced to 296 K for every case studied. The data are summarized in Table 6 and Figures 23-26.

Table 6. DLOCA Modeling Results of Open, Direct Cooling

p/d	Pressure [atm]	Heat Production [W]	Fraction of original steady state power	Time after SCRAM [d]	w per channel [kg/s]	max coolant velocity [m/s]	Pumping Power required to overcome friction in core [W]	Avg. ΔT_b [K]	Avg. $T_{b,out}$ [K]
1.01	1	3.00E+04	0.001	50	4.498E-06	2.83E+00	3.617E+01	827	1123
1.01	1	1.50E+05	0.005	1	2.263E-05	1.42E+01	7.916E+02	822	1118
1.01	1	3.00E+05	0.01	0.1	4.564E-05	2.84E+01	4.091E+03	815	1111
1.01	1	2.10E+06	0.07	0	3.556E-03	2.04E+02	6.745E+05	732	1028
1.01	1	3.00E+07	1	0	4.940E-03	2.90E+03	8.558E+08	753	1049
1.01	90	3.00E+07	1	n/a	4.940E-03	3.22E+01	1.058E+05	753	1049
1.1	1	3.00E+04	0.001	50	4.301E-06	1.01E+00	1.930E+00	865	1161
1.1	1	1.50E+05	0.005	1	2.187E-05	5.06E+00	3.834E+01	850	1147
1.1	1	3.00E+05	0.01	0.1	4.467E-05	1.02E+01	1.979E+02	833	1129
1.1	1	2.10E+06	0.07	0	4.378E-04	7.86E+01	4.637E+04	595	891
1.1	1	3.00E+07	1	0	5.487E-03	1.08E+03	5.035E+07	678	974
1.1	90	3.00E+07	1	n/a	5.487E-03	1.20E+01	6.422E+03	678	974
1.15	1	3.00E+04	0.001	50	4.220E-06	7.20E-01	8.281E-01	882	1178
1.15	1	1.50E+05	0.005	1	2.157E-05	3.62E+00	1.481E+01	862	1158
1.15	1	3.00E+05	0.01	0.1	4.444E-05	7.30E+00	7.547E+01	837	1133
1.15	1	2.10E+06	0.07	0	5.234E-04	6.03E+01	2.390E+04	497	794
1.15	1	3.00E+07	1	0	5.868E-03	7.91E+02	2.144E+07	634	930
1.15	90	3.00E+07	1	n/a	5.868E-03	8.79E+00	2.867E+03	634	930
1.2	1	3.00E+04	0.001	50	4.180E-06	5.60E-01	4.702E-01	890	1186
1.2	1	1.50E+05	0.005	1	2.151E-05	2.80E+00	7.330E+00	865	1161
1.2	1	3.00E+05	0.01	0.1	4.469E-05	5.65E+00	3.645E+01	832	1129
1.2	1	2.10E+06	0.07	0	5.340E-04	4.70E+01	1.163E+04	488	784
1.2	1	3.00E+07	1	0	6.350E-03	6.29E+02	1.154E+07	586	882
1.2	90	3.00E+07	1	n/a	6.350E-03	6.98E+00	1662	586	882
1.3	1	3.00E+04	0.001	50	4.063E-06	3.70E-01	2.478E-01	916	1212
1.3	1	1.50E+05	0.005	1	2.118E-05	1.85E+00	2.746E+00	878	1174
1.3	1	3.00E+05	0.01	0.1	4.480E-05	3.76E+00	1.229E+01	830	1126
1.3	1	2.10E+06	0.07	0	5.340E-04	3.14E+01	3.582E+03	488	784
1.3	1	3.00E+07	1	0	7.350E-03	4.42E+02	4.620E+06	506	802
1.3	90	3.00E+07	1	n/a	7.350E-03	4.91E+00	8.463E+02	506	802
1.4	1	3.00E+04	1.00E-03	50	3.924E-06	2.60E-01	1.849E-01	948	1244
1.4	1	1.50E+05	0.005	1	2.072E-05	1.33E+00	1.527E+00	898	1194
1.4	1	3.00E+05	0.01	0.1	4.701E-05	2.72E+00	5.847E+00	832	1128
1.4	1	2.10E+06	0.07	0	5.340E-04	2.28E+01	1.437E+03	488	784
1.4	1	3.00E+07	1	0	8.430E-03	3.40E+02	2.390E+06	441	737
1.4	90	3.00E+07	1	n/a	8.430E-03	3.77E+00	6.113E+02	441	737

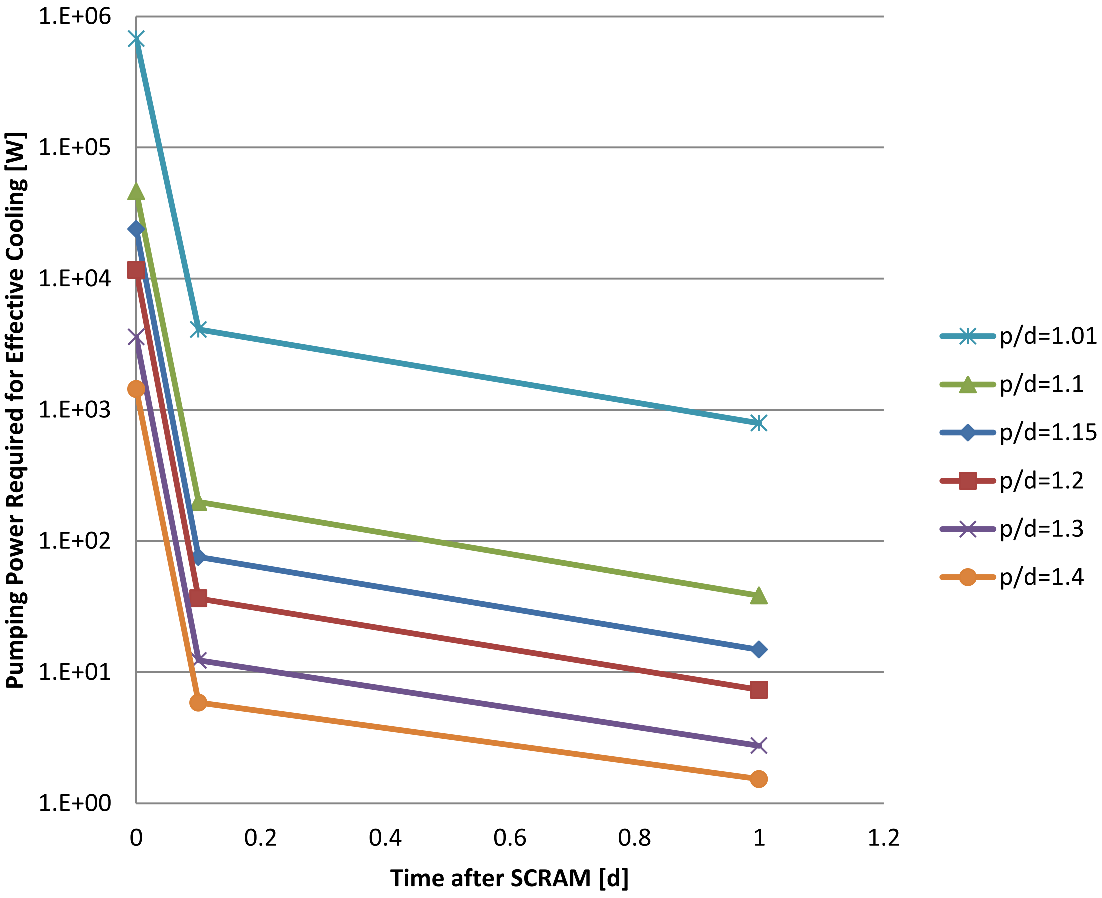

Figure 23. Effect of p/d ratio on short term open-cooling after SCRAM from 30 MW.

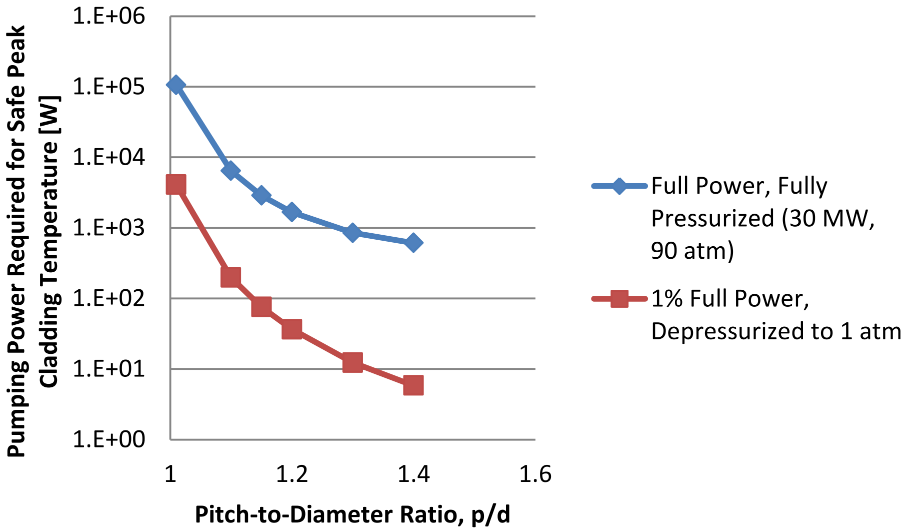

Figure 24. Pumping power required when core is cooled directly by ambient air.

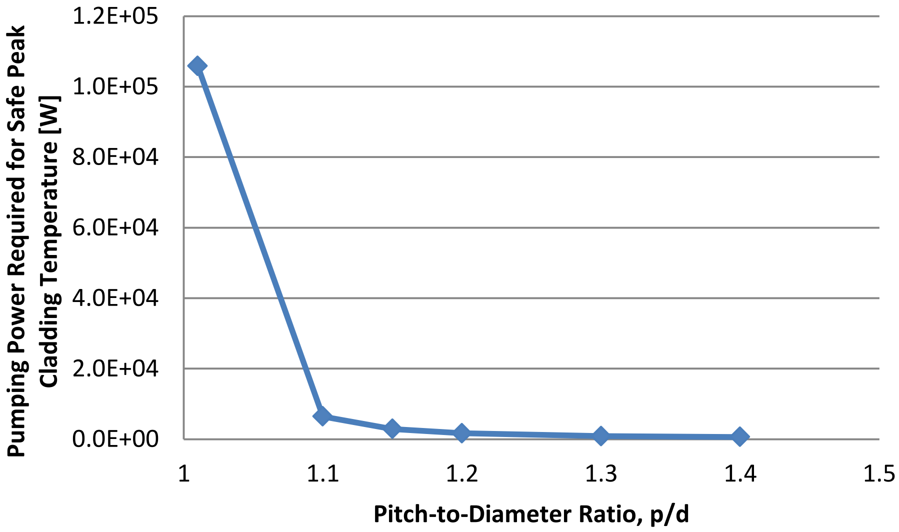

Figure 25. Pumping power required for 30MWth operation when cooled directly by ambient air.

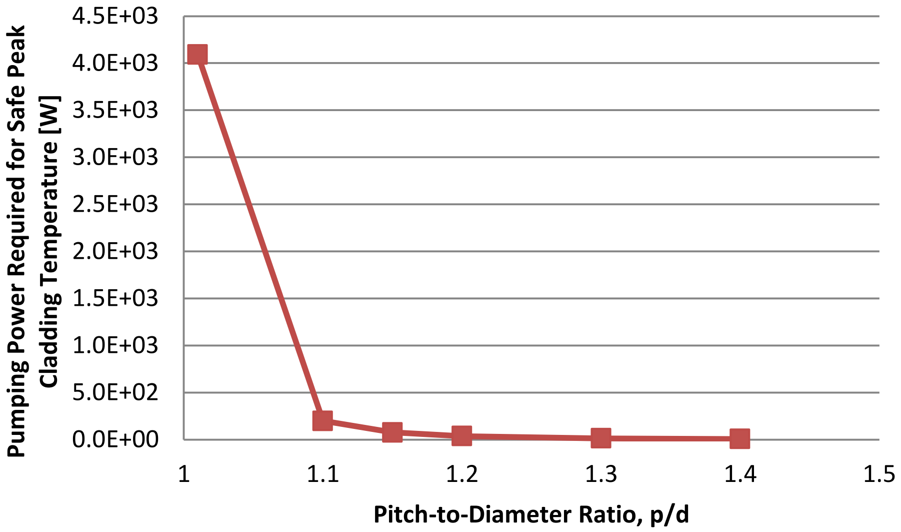

Figure 26. Pumping power required for 1% full power decay heat, following DLOCA, when the core is cooled directly by ambient air.

4.10 Thermodynamic Cycle Performance

The analysis package described in chapter 3 was used to optimize the thermodynamic efficiencies of the open and closed Brayton cycles. This analysis was performed using the case of p/d=1.15, because the DLOCA modeling results suggest that frictional losses in the core increase dramatically as p/d decreases below approximately 1.15, resulting in significant power requirements. The cladding selected for this analysis was SiC. This is because Zircaloy cannot tolerate high fast neutron fluence (as shown in section 4.7), steel corrodes quickly in high temperature air[42], and Inconel has less desirable thermal properties than SiC (as shown in section 4.1).

4.10.1 Open Brayton Cycle

The results of calculating the thermodynamic efficiency of the open Brayton cycle configuration are shown in Figure 27. For each case tested, the compressor intake air was set at 296 K, with a pressure of 1 atmosphere. The thermal power output of the reactor was 30 MW. The mass flow rate was adjusted so as to maintain an achievable coolant velocity as well as the upper limits of the material temperatures for normal operation. The material temperatures considered were the fuel, the cladding, and the turbine blades, but in every case, the peak cladding temperature was the limiting temperature. The upper limit of 16 for the compression ratio (a typical limit for gas turbines[36]) was also considered, but as shown in Figure 27, this is not the limiting factor for this open Brayton cycle model.

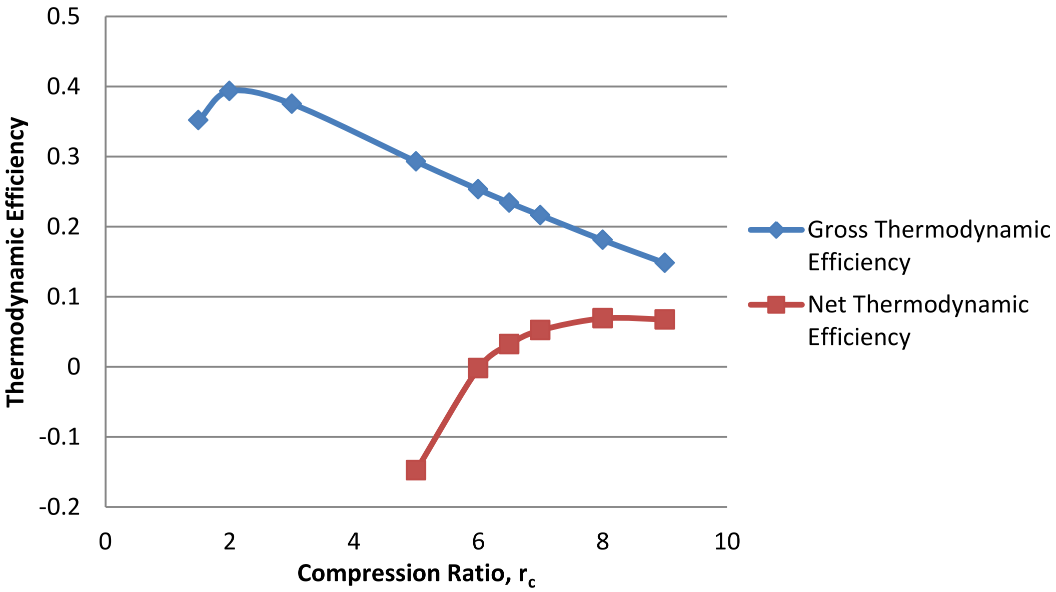

Figure 27. Gross and Net Thermodynamic Efficiencies of the open Brayton cycle.

Notice that the Gross Thermodynamic Efficiency, ζ, peaks at 39.4% when r_c is equal to approximately 2. However, the velocity of the coolant at only 16 atmospheres or less must be very high to maintain the necessary mass flow rate, and the high velocities of the coolant produce friction in the core that requires a great deal of pumping power to overcome. This pumping reduces the Net Thermodynamic Efficiency to a negative value for all compression ratios below approximately 6.

The Net Thermodynamic Efficiency peaks at approximately 6.9% when the compression ratio is 8, but even this is not attainable. In order to have a positive Net Thermodynamic Efficiency with a compression ratio above approximately 7, the compressor outlet temperature would have to be greater than the turbine outlet temperature, which cannot be a physical reality in a recuperated Brayton cycle, because it implies that the recuperator removes heat from the compressed air before it enters the reactor.

For this model, there exists only a very narrow operating range that is at least theoretically possible. At a compression ratio of 6.5, the reactor can achieve a Net Thermodynamic Efficiency of 3.3% with only a small amount of recuperation. This dismal Net Thermodynamic Efficiency is the best the reactor can perform, given the reactor composition and geometry, and the simple open Brayton cycle described in Figure 2. The reactor's thermodynamic cycle in this mode is described by Table 7.

Table 7. Open Brayton Cycle Parameters for Maximum Efficiency

Compression Ratio, r_c	6.5
Coolant Mass Flow Rate, w [kg/s]	100.79
Peak Clad Temperature, $T_{Cl,Max}$ [K] (SiC)	1173.15
Peak Fuel Temperature, $T_{f,Max}$ [K] (UO2)	1543.11
Compressor Outlet / Recuperator Inlet Temp., T_2 [K]	500.73
Recuperator Outlet / Reactor Inlet Temp., T_3 (or $T_{b,in}$) [K]	506.65
Avg. Reactor Outlet / Turbine Inlet Temp., T_4 [K]	774.82
Turbine Outlet / Recuperator Inlet Temp., T_5 [K]	507.27
Exhaust Temperature, T_6 [K] (Open Cycle)	501.39
Average Coolant Velocity, v [m/s]	199.37
Maximum Coolant Velocity, v_{max} [m/s]	240.70
Gross Thermodynamic Efficiency, ζ	0.234
Pumping Power to Overcome Friction, P_{fric} [MW]	6.06
Net Thermodynamic Efficiency, $ζ_{net}$	0.032

4.10.2 Closed Brayton Cycle

The closed Brayton cycle was analyzed assuming a system pressure of 90 atmospheres in the reactor vessel[12]. It was also analyzed for two cases: one where the compressor inlet temperature, T_1, is 296 K, and one where it is 350 K. Again, in every case, the peak cladding temperature is the factor that sets a lower limit for the coolant mass flow rate, and therefore sets an upper limit for the turbine inlet temperature and the thermodynamic efficiency. Unlike the open cycle, the closed cycle model demonstrates that its maximum theoretical Net Thermodynamic Efficiency occurs within the attainable range of the compression ratio. The results of optimizing the efficiency across a range of compression ratios are expressed in Figure 28 for both values of T_1.

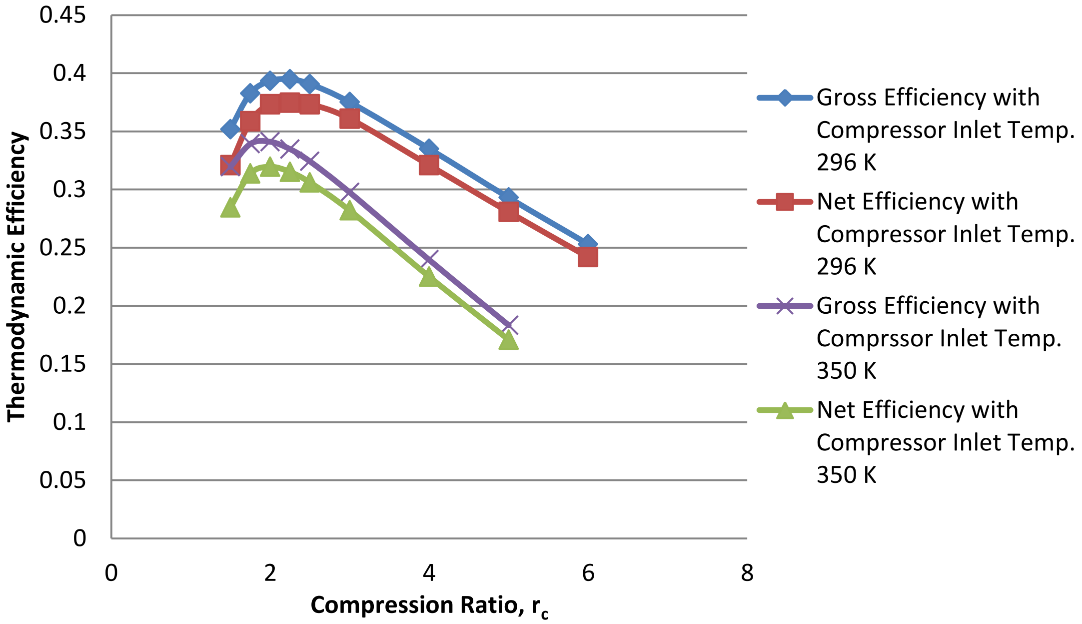

Figure 28. Gross and Net Thermodynamic Efficiencies of the closed Brayton cycle.

When the compressor inlet temperature, T_1, is set at 296 K, the Gross Thermodynamic Efficiency curve of the closed Brayton cycle is identical to that of the open Brayton cycle. The closed cycle's Net Thermodynamic Efficiency, however, closely follows the Gross Thermodynamic Efficiency. This is because of the closed cycle's high system pressure, which increases the density of the air, enabling the necessary mass flow rate to be achieved without the high coolant velocities that characterize the open cycle. Lower coolant velocities mean less friction to overcome. The closed Brayton cycle does require power to operate the heat exchanger, but it is clear from these results that the closed cycle's reduced friction burden far outweighs the open cycle's benefit of omitting the heat exchanger's power requirements. The maximum Gross and Net Thermodynamic Efficiencies of the closed Brayton cycle both occur with a compression ratio of 2.25, and are achieved with the combination of system characteristics listed in Table 8.

Table 8. Closed Brayton Cycle Parameters for Maximum Efficiency where T_1=296 K

Heat Exchanger Outlet / Compressor Inlet Temp., T_1 [K]	296
Heat Exchanger Outlet / Compressor Inlet Pressure [atm]	40
Compression Ratio, r_c	2.25
Coolant Mass Flow Rate, w [kg/s]	145.23
Peak Clad Temperature, $T_{Cl,Max}$ [K] (SiC)	1173.15
Peak Fuel Temperature, $T_{f,Max}$ [K] (UO2)	1535.61
Compressor Outlet / Recuperator Inlet Temp., T_2 [K]	372.72
Recuperator Outlet / Reactor Inlet Temp., T_3 (or $T_{b,in}$) [K]	696.00
Avg. Reactor Outlet / Turbine Inlet Temp., T_4 [K]	882.09
Turbine Outlet / Recuperator Inlet Temp., T_5 [K]	731.93
Recuperator Outlet / Heat Exchanger Inlet Temp., T_6 [K] (Closed Cycle)	408.64
Average Coolant Velocity, v [m/s]	25.580
Maximum Coolant Velocity, v_{max} [m/s]	28.57
Gross Thermodynamic Efficiency, ζ	0.395
Pumping Power to Operate Heat Exchanger, P_{pump} [MW]	0.449
Pumping Power to Overcome Friction, P_{fric} [MW]	0.133
Net Thermodynamic Efficiency, ζ_{net}	0.375

For the case of T_1=350 K, the maximum achievable efficiency is predictably lower than if the compressor receives the coolant at a lower temperature. The characteristics of the reactor for maximum achievable efficiency in this configuration are given in Table 9.

Table 9. Closed Brayton Cycle Parameters for Maximum Efficiency where T_1=350 K

Heat Exchanger Outlet / Compressor Inlet Temp., T_1 [K]	350
Heat Exchanger Outlet / Compressor Inlet Pressure [atm]	40
Compression Ratio, r_c	2
Coolant Mass Flow Rate, w [kg/s]	149.32
Peak Clad Temperature, $T_{Cl,Max}$ [K] (SiC)	1173.15
Peak Fuel Temperature, $T_{f,Max}$ [K] (UO2)	1535.27
Compressor Outlet / Recuperator Inlet Temp., T_2 [K]	440.72
Recuperator Outlet / Reactor Inlet Temp., T_3 (or $T_{b,in}$) [K]	707.91
Avg. Reactor Outlet / Turbine Inlet Temp., T_4 [K]	888.92
Turbine Outlet / Recuperator Inlet Temp., T_5 [K]	737.59
Recuperator Outlet / Heat Exchanger Inlet Temp., T_6 [K] (Closed Cycle)	470.41
Average Coolant Velocity, v [m/s]	26.613
Maximum Coolant Velocity, v_{max} [m/s]	29.60
Gross Thermodynamic Efficiency, ζ	0.335
Pumping Power to Operate Heat Exchanger, P_{pump} [MW]	0.461
Pumping Power to Overcome Friction, P_{fric} [MW]	0.147
Net Thermodynamic Efficiency, ζ_{net}	0.315

4.11 Reactivity Control and Feedback

The simulation of reactivity control in the air-cooled fast reactor is accomplished by the use of control rods and burnable poisons. The control rods are assumed to be inserted from the top of the reactor. The control rod material modeled is Boron Carbide. The control rods are arranged in assemblies with the same dimensions as the fuel assemblies. There are 13 control rod assemblies. One is placed in the center of the core, where the neutron flux is greatest. The remaining 12 are placed in a ring about the center, roughly where the flux is maximum after the central control assembly depresses the flux in the center. The control rods do not have enough reactivity to shut down the reactor reliably at all points in the core lifetime; the BOL core would remain supercritical if the control rods alone were relied upon to control the initial excess reactivity. Therefore, burnable poisons are mixed with the fuel, in order to manage the BOL excess reactivity[28]. The burnable poison composition chosen for simulation in MCNP is the Westinghouse Wet Annular Burnable Absorber (WABA) formulation, which includes Boron, Carbon, Oxygen, and Aluminum[54]. The goal of simulating burnable poisons in the fuel is to ensure the BOL reactivity is manageable, while maximizing the potential burnup of the fuel. Adding burnable poisons can reduce the ultimate burnup, because mixing burnable poisons into the fuel necessarily displaces fuel, reducing the amount of fuel that is loaded into the constant-volume core. This simulation is performed with SiC cladding, and with p/d=1.15.

Figure 29 shows the BOL cold-shut-down neutron multiplication factor for the air-cooled GFR for several weight fractions of burnable poisons admixed in the fuel. In order to compute the BOL cold-shut-down multiplication factor, all material temperatures were set to room temperature, 296 K, while the control rods were fully inserted. It is important and conservative that the simulation be run with all temperatures at room temperature, because as will be shown in the following paragraphs, the materials have a negative temperature coefficient of reactivity, meaning that reactivity is added to the reactor as the materials cool down. Additionally, for each burnable poison weight fraction tested, a MCNP burnup calculation was done with the control rods removed, and the materials near their operating temperatures. This helps to characterize the balance that must be struck between having a large shut-down reactivity margin, and having a long core lifetime. A typical commercial reactor is required to maintain a shutdown margin of 1 to 5% reactivity[55]. Figure 29 shows that this shutdown margin is achievable with approximately 14 to 21 % burnable poison admixture in the fuel, and that this range corresponds inversely to an achievable fuel burnup range of 39 to 68 $\frac{GWd}{tHM}$.

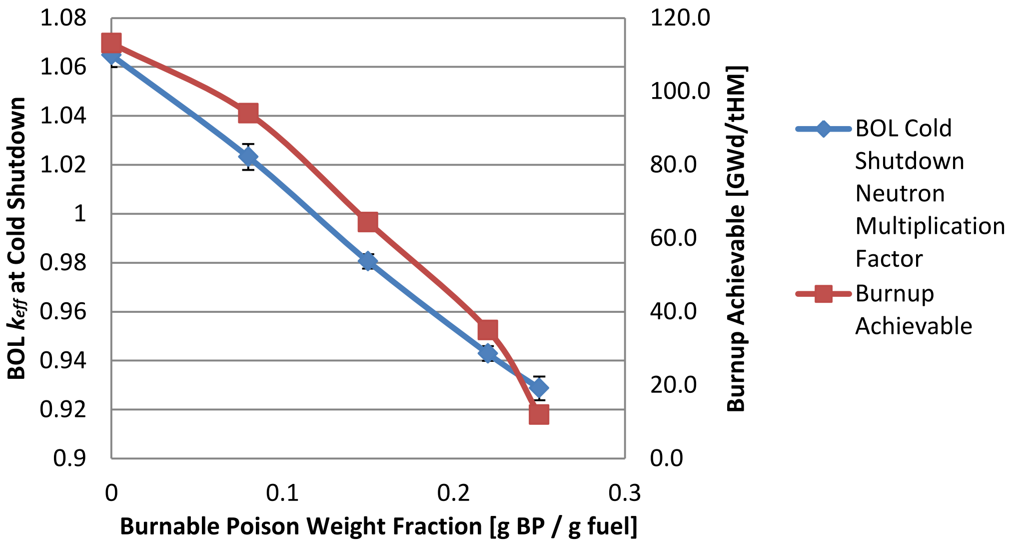

Figure 29. Burnable poison effects on initial reactivity and burnup.

Feedback effects can be characterized by coefficients that describe the reactor's change in reactivity as a function of changes in another parameter in the reactor, such as the temperature of the fuel or coolant, the system pressure, or of the overall power of the reactor[28].

The reactivity feedback due to changes in the fuel temperature is characterized by the fuel temperature coefficient of reactivity, α_F, which is given by Eq. 59[28].

$$\alpha_F = \frac{d\rho}{dT_F} \tag{59}$$

Assuming that the feedback is linear for a certain temperature range allows the equation to be modified as in Eq. 60. This is convenient, because the MCNP input deck can easily be changed to model the reactor with its materials at various temperatures.

$$\alpha_F = \frac{\Delta\rho}{\Delta T_F} \tag{60}$$

Using the value of k_{eff} calculated with the reactor materials at their anticipated operating conditions, where the fuel temperature, T_{F1}, is 1200 K, the initial reactivity is calculated using Eq. 61[28]. These calculations were performed with the control rods fully removed.

$$\rho = \frac{k_{eff}-1}{k_{eff}} \tag{61}$$

By this equation, the BOL total reactivity available at full power is calculated as follows.

$$\rho_1 = \frac{1.16636 - 1}{1.16636} = 0.1426318 \pm 1.71E - 5$$

After running another KCODE calculation, using the same input deck, but with the fuel temperature changed to 293.6 K, k_{eff} was found to be 1.00064 ± 0.00057, which corresponds to

$$\rho_2 = \frac{1.16821 - 1}{1.16821} = 0.1439895 \pm 1.72E - 5$$

Therefore, by Eq. 60,

$$\alpha_F = \frac{0.1439895 - 0.1426318}{293.6\ [K] - 1200\ [K]} = -1.49795337E - 6 \pm 2.682E - 8\ [K^{-1}]$$

A more rigorous estimate of the fuel and moderator feedback effects would include modeling the thermal expansion of the fuel. That would mean increasing the volume of the fuel in the MCNP model to reflect some reference value of the material densities’ responses to temperature changes. If this were included in this model, then the value of α_F would be more strongly negative, since decreasing the density also decreases the macroscopic fission cross section[28]. This is a good reactor safety characteristic.

Additionally, the assumption of linear dependence of reactivity on fuel temperature is conservative at higher temperatures. To generate two additional data points, the MCNP simulation is reiterated with fuel temperatures of 600 K and 900 K. This enables a more accurate characterization of the reactivity feedback effect of fuel temperature, as shown in Figure 30.

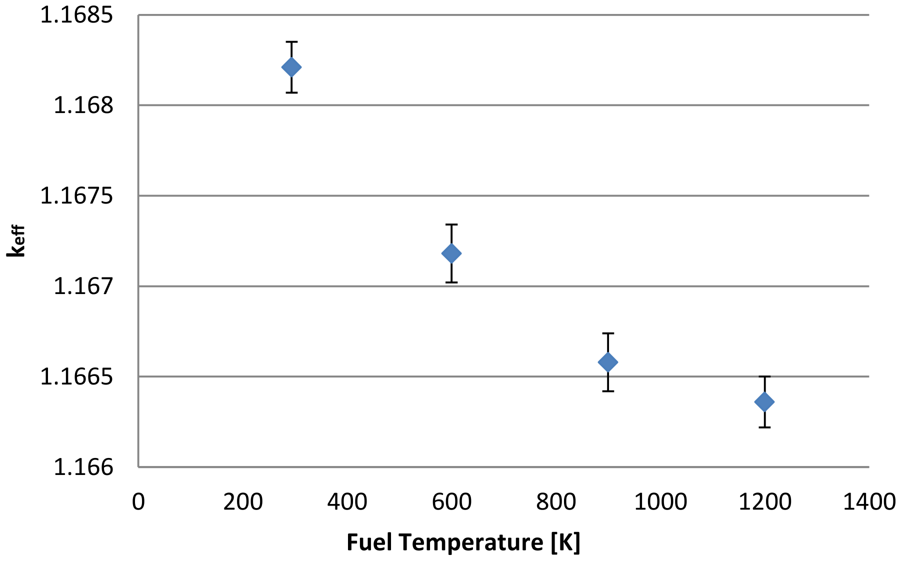

Figure 30. Effect of fuel temperature on reactivity in the AGFR.

The next feedback parameter calculated was the coolant temperature coefficient of reactivity, α_b. Unlike the calculation of α_F, the calculation of α_b accounts for the material's change in density along with its change in temperature, because the bulk coolant's density changes much more dramatically with temperature than does the fuel. For this calculation, the system pressure is held constant, while the coolant's temperature and density change. The average reactivity feedback phenomenon over a temperature range is described by Eq. 62[28], which is similar to Eq. 60,

$$\alpha_b = \frac{\Delta\rho}{\Delta T_b} \tag{62}$$

Applying this equation by inserting values calculated via MCNP yielded the following:

$$\alpha_b = \frac{0.1435423 - 0.1426318}{293.6\ [K] - 1200\ [K]} = -2.971708597E - 6 \pm 1.291E - 7\ [K^{-1}]$$

Like the fuel temperature reactivity feedback, the coolant temperature feedback effect is more accurately characterized as a nonlinear function, as shown in Figure 31.

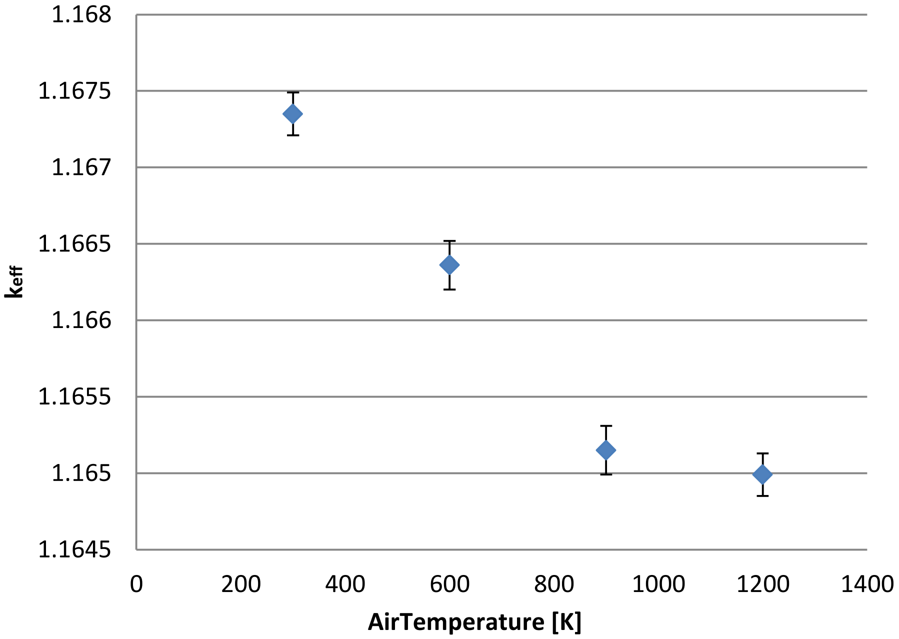

Figure 31. Effect of coolant temperature on reactivity in the AGFR.

Finally, in a gas-cooled reactor, the worst-case DLOCA is one that results in the complete depressurization of the containment vessel. Particularly in the case of the open Brayton cycle, where the coolant could depressurize from up to 9 MPa to 1 atm, there could be a drastic change in reactivity. This could be either a positive or negative feedback effect on the reactivity. Let Eq. 63 define a depressurization or "void" coefficient of reactivity, assuming a linear feedback effect.

$$\alpha_{void} = -\frac{\Delta\rho}{\Delta P} \tag{63}$$

For this simulation of the air-cooled GFR, when the coolant completely depressurizes, but all temperatures remain the same as for normal operation, then the void coefficient is given by:

$$\alpha_{void} = \frac{0.1415572 - 0.1426906}{9.12E6\ [Pa] - 1.01E5\ [Pa]} = -1.25679E - 10 \pm 5.45E - 12\ [Pa^{-1}]$$

Again, the actual feedback effect of depressurization is not linear, as shown by Figure 32, which was generated by varying the density of the coolant in the MCNP model, to correspond to various pressures between the operating pressure and complete depressurization. It is evident from Figure 32 that the feedback is negative from 90 to 3 atmospheres, and positive from 3 to 1 atmosphere. This means that there is more than one feedback effect that depends upon the density of the air (and hence the pressure), and that the feedback effects compete with each other. At approximately 3 atmospheres, one the dominance of a negative coolant density feedback effect gives way to the dominance of a positive coolant density feedback effect. A plausible example would be that the loss of coolant from the reactor initially causes a decrease in neutron downscattering, leading to spectral hardening, lower fuel cross sections, and increased leakage. Then, at approximately 3 atmospheres, the decreasing rate of neutron absorption in the air causes the fuel to see a greater neutron flux, which increases the fission rate despite the negative feedback effects.

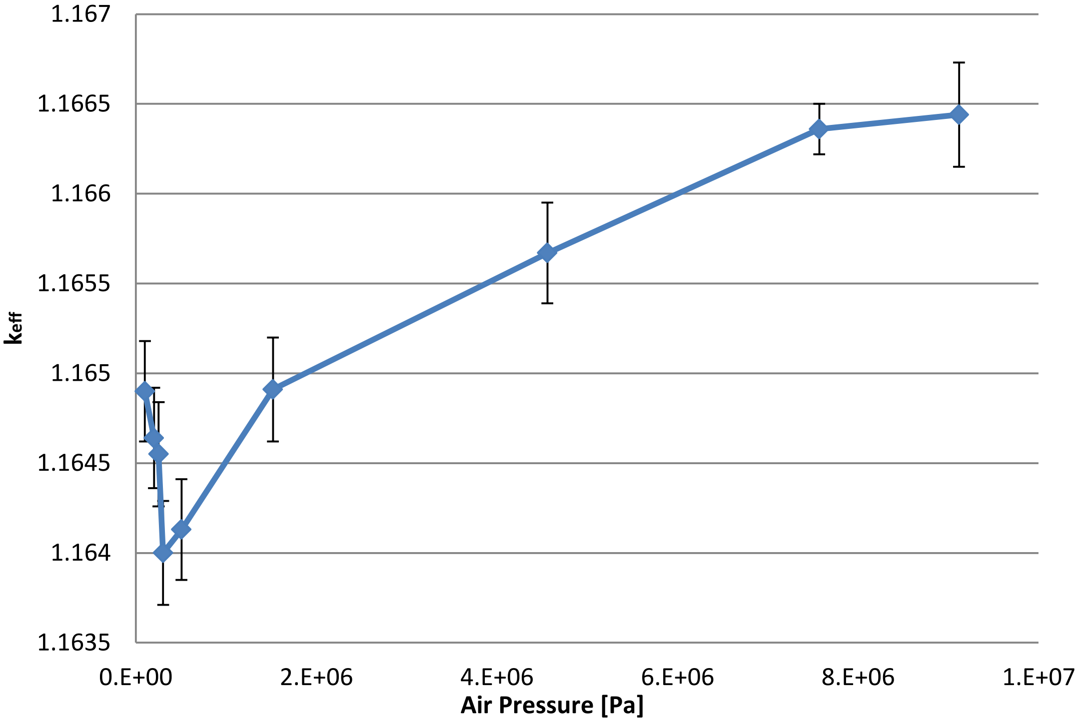

Figure 32. Effect of coolant pressure on reactivity in the AGFR.

The implications of these reactivity coefficients are good in that the values are all slightly negative, meaning that the reactor tends to reduce its power level if temperatures increase or if coolant pressure decreases.

4.12 Post-Irradiation Considerations

When MCNPX is used to perform fuel depletion calculations, it calculates the nuclide inventory based upon the neutron interaction rates and decay rates of the nuclides that comprise the fuel. Table 10 presents the post-irradiation nuclide inventory of the air-cooled GFR modeled here and that of PWR fuel from the Robinson Nuclear Plant[56] in Hartsville, SC.

Table 10. Summary of Radionuclide Inventories in Used Fuel

Nuclide Group	**AGFR 75.3 GWd / tHM**	**AGFR 120 GWd / tHM**	**AGFR 75.3 GWd / tHM + 8 yr decay**	**AGFR 120 GWd / tHM + 8 yr decay**	**PWR 38.6 GWd / tHM + 22 yr decay**	**PWR 72 GWd / tHM + 8 yr decay**
Total TRU	3.20E+00	3.64E+00	8.45E-04	1.96E-03	5.57E-02	1.80E-01
Total MA	3.20E+00	3.64E+00	2.62E-06	8.89E-06	5.04E-03	3.62E-02
Total Pu	8.73E-04	2.19E-03	8.42E-04	1.95E-03	5.06E-02	1.44E-01
Total Actinides	6.60E+00	7.59E+00	8.49E-04	1.97E-03	5.57E-02	1.80E-01
Total Non-Actinides	2.00E-01	5.08E+00	1.68E-01	2.58E-01	2.20E-01	4.46E-01
Total Activity	6.80E+00	1.27E+01	1.69E-01	2.60E-01	2.75E-01	6.26E-01

A complete listing of the data used to generate Table 10 is found in Table 12, located in Appendix A. The first security-related observation from the material presented in Table 10 is that the air-cooled GFR (AGFR) requires such a high initial fissile concentration that the fuel constitutes weapons grade material throughout its lifetime. In this respect, PWR fuel is clearly a more desirable waste product than the AGFR fuel. Additionally, the AGFR, when fueled with HEU, provides no "self-shielding" benefits. The spent fuel of the AGFR is less radioactive in every calculable way, as shown in Figure 33. This is good from an environmental standpoint, but from a security standpoint, it means that the AGFR spent fuel lacks desirable radiological traits, in comparison with the PWR spent fuel. Its radioactivity does not provide as great a deterrent for theft or handling for weapons manufacturing.

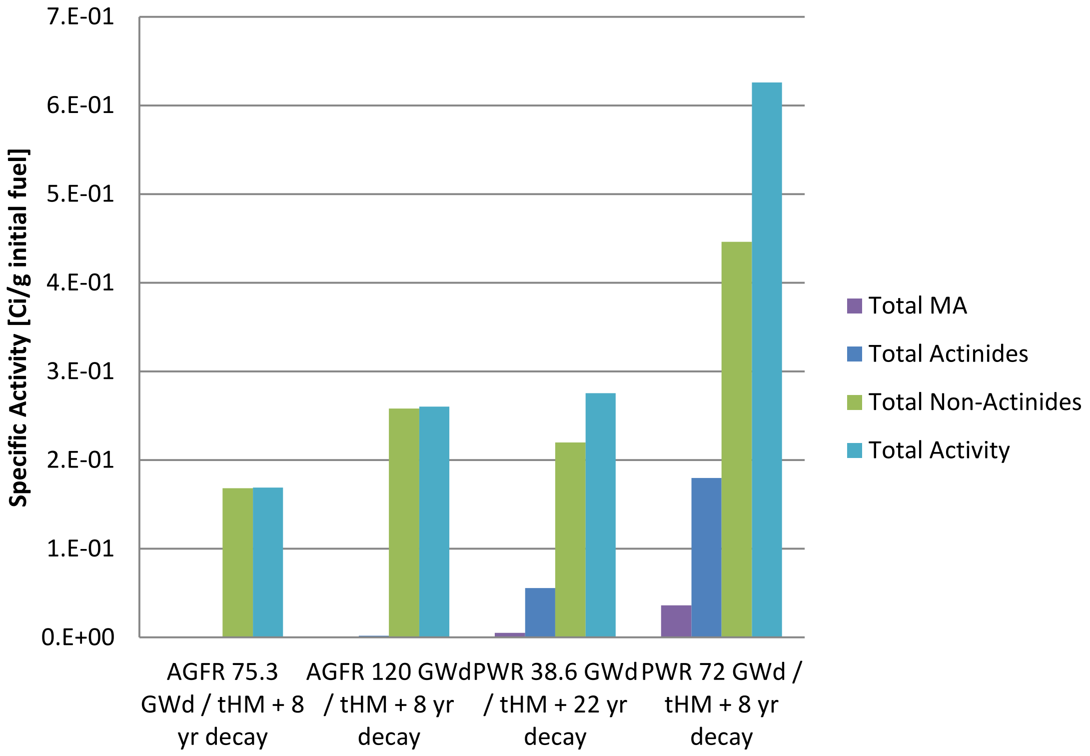

Figure 33. Comparison of specific activities of used fuel from the air-cooled GFR and a sample PWR.

Placing HEU on a mobile platform for expeditionary use does pose a security concern pertaining to the potential theft of the material. This concern is not prohibitive, but it requires that the greatest security emphasis be placed on loss prevention measures.

Extensive optimization should also be done in order to reduce the necessary fissile enrichment without unduly reducing the power density. Despite its modularity and transportability, this reactor does not have unlimited mobility, and it could easily be identified and tracked in the event that the entire platform is stolen. Examples of small and/or transportable reactors fueled by highly enriched uranium (HEU) include naval reactors as well as over 100 research reactors worldwide[57].

4.13 Radiation and Shielding

It is important that this design include an estimate of the weight and volume of the reactor's shielding, because it has a profound impact on the transportability of the system. Before calculating the shielding, the reactor has been modeled as being nearly infinitely reflected with steel. The primary types of radiation produced in a reactor that need to be shielded are neutrons and photons[28]. Since neutrons are best attenuated by materials with low molar masses, and photons are attenuated by materials with high molar masses, a layer of each type of material is needed[28]. A typical material for the shielding of neutrons is water, while lead is a typical choice for the shielding of photons. These are the two material types chosen for this design. Water is chosen, because it can easily be transported separately from the reactor system itself. To begin to estimate the size of the shielding required, an initial simulation is conducted using MCNP. The reactor is modeled with a 30 cm cylindrical jacket of water surrounding the steel vessel, followed by a 30 cm jacket of lead surrounding the water. Tally volumes are established in radial increments within the shielding about the mid-plane of the core. MCNP calculates the fluxes of neutrons and photons within the tally volumes. The fluxes are then weighted and converted to dose rates using the ANSI/ANS 6.1.1-1977 dose functions for neutrons and photons[25]. The results of this simulation are shown in Figure 34.

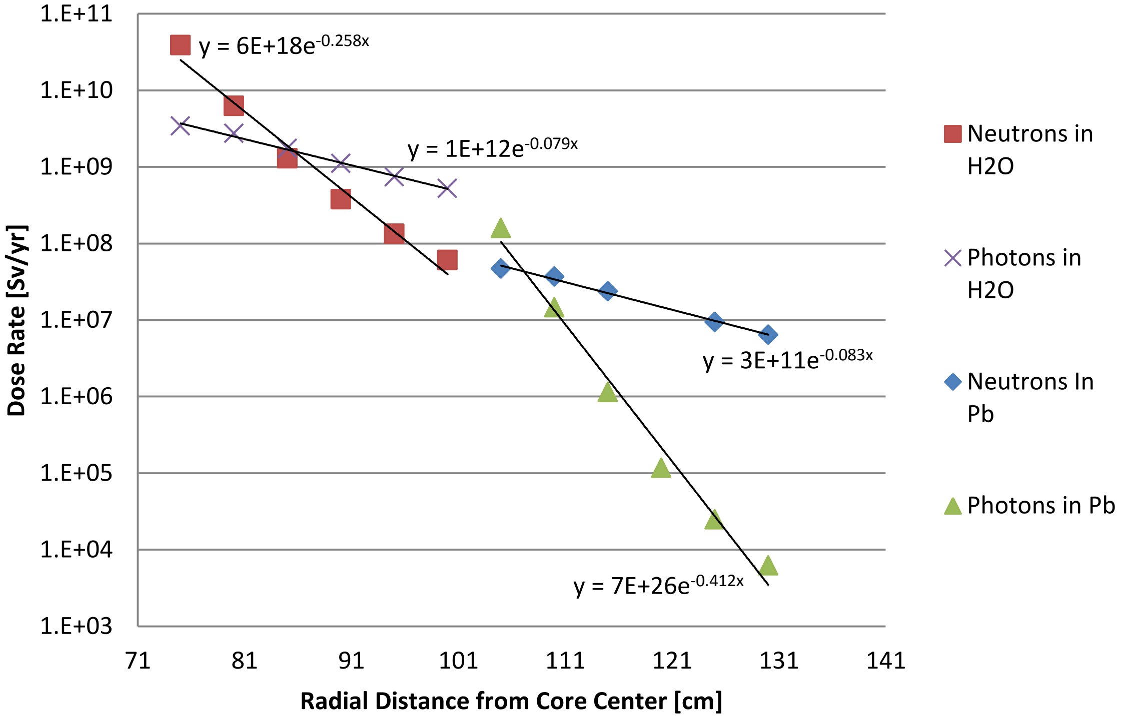

Figure 34. Dose rates due to neutrons and photons within 30 cm of water and 30 cm of lead shielding.

As expected, this figure shows that the water attenuates the neutrons more rapidly than photons, while lead attenuates photons more rapidly than neutrons. Notice also that the dose rates at the outside of the lead shielding remain much higher than the statutory limit of 0.05 $\frac{Sv}{yr}$. For simplicity, this study will identify the amount of water shielding required to reduce the neutron dose rate to 0.05 $\frac{Sv}{yr}$, and the lead shielding required to reduce the photon dose rate to 0.05 $\frac{Sv}{yr}$. Functions are fitted to the data points in order to be extrapolated to the distance required. The function associated with neutron attenuation in water extrapolates to 0.05 $\frac{Sv}{yr}$ at a radial distance of 179.2 cm, which corresponds to 108 cm of water shielding. The function associated with photon attenuation in lead extrapolates to 0.05 $\frac{Sv}{yr}$ at a radial distance of 164.1 cm, which corresponds to 63.2 cm of lead shielding. These values are then used in a second iteration of the shielding simulation. Figure 35 shows the results of the second iteration.

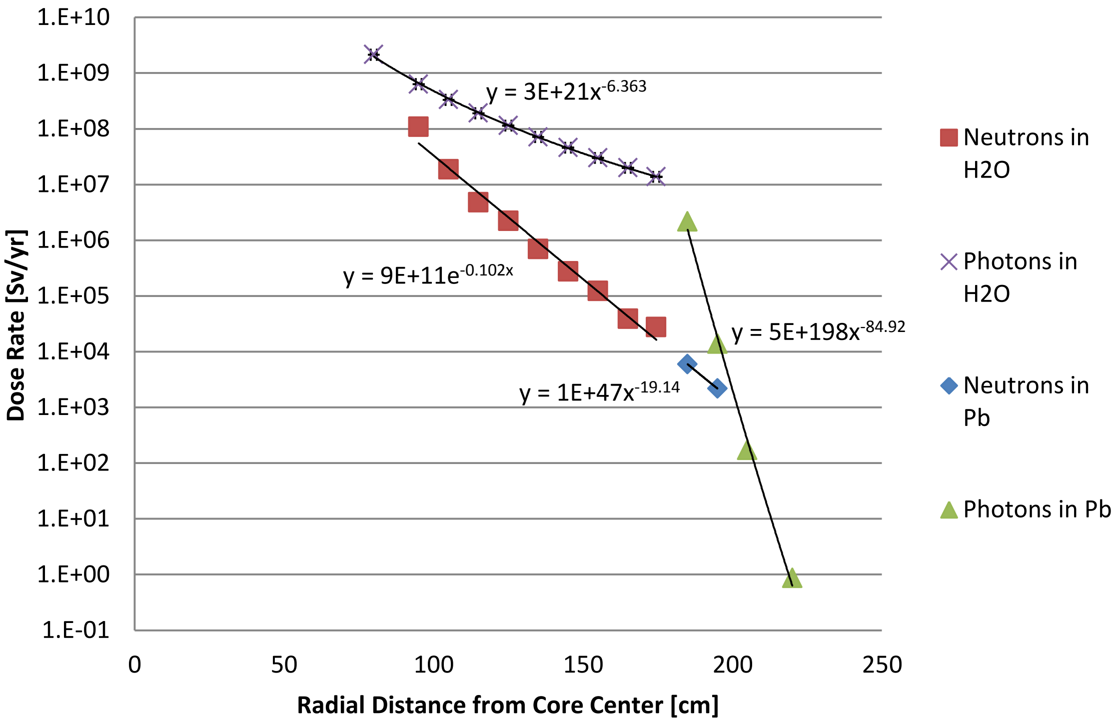

Figure 35. Dose rates due to neutrons and photons within 108 cm of water and 63.2 cm of lead shielding.

The second iteration of the shielding simulation resulted in an updated prediction of 239 cm of water, and 51 cm of lead being necessary to reduce the dose rate contribution to 0.05 $\frac{Sv}{yr}$ each for neutrons and photons. These values are then used in yet a third simulation, since the second simulation fails to predict that it had sufficient shielding to reach 0.05 $\frac{Sv}{yr}$ for neutrons and photons. Figure 36 shows the results of the third iteration.

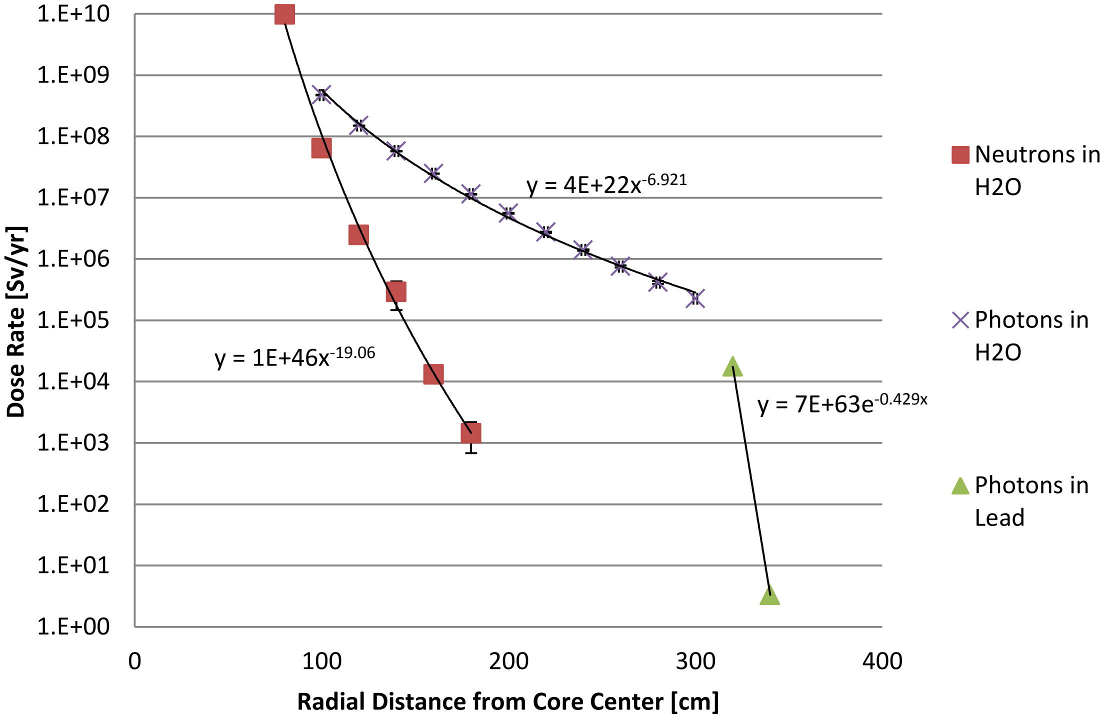

Figure 36. Dose rates due to neutrons and photons within 239 cm of water and 51 cm of lead shielding.

Figure 36 predicts that the dose rate due to neutrons falls to 0.05 $\frac{Sv}{yr}$ within 232.2 cm of water shielding, which means that third simulation predicts that it does have sufficient neutron shielding with 239 cm. Figure 36 also predicts that the photon dose rate is reduced to 0.05 $\frac{Sv}{yr}$ within 39.7 cm. The values to be reported as the design recommendation for this study are 239 cm of water and 39.7 cm of lead.

In order to estimate the necessary shielding thickness in the axial direction, a neutron and photon tally was conducted just below the bottom of the steel vessel. The dose rate outside the bottom of the steel vessel was then compared to the dose rate outside the vessel in the radial direction. The neutron dose rate in the radial direction was $2.07E10 \pm 7.26E6 \frac{Sv}{yr}$, while the neutron dose rate at the bottom of the vessel was $1.45E9 \pm 2.90E7 \frac{Sv}{yr}$. The photon dose rate in the radial direction was $3.05E9 \pm 5.48E6 \frac{Sv}{yr}$, while the photon dose rate at the bottom of the vessel was $5.38E8 \pm 3.98E6 \frac{Sv}{yr}$. If the shielding requirements are proportional to the dose rate, then the water shielding in the axial direction must be at least 7.02 % as thick as in the radial direction, and the axial lead shielding must be at least 17.7 % as thick as in the radial direction. Therefore, 16.78 cm of water and 7.03 cm of lead are needed on top and bottom of the reactor to attenuate neutrons and photons in the axial directions.

4.14 Transportability

Ideally, the entire reactor system (core, containment, shielding, plumbing, turbomachinery, and heat exchanger) would be light and compact enough to fit on a single vehicle, and the reactor could be operated without having to be removed from the vehicle. However, since the goal of this design is to provide temporary power to a remote location, such a reactor concept may still be considered viable if multiple vehicles are required for transportation, and if on-site assembly and disassembly are required.

The reactor configuration analyzed in this study is contained inside a steel pressure vessel that also provides 30 cm of neutron reflection in the radial direction. The vessel is 142 cm in diameter, and 295 cm tall. This thesis had stipulated that the unit must be less than 430 cm tall in order to accommodate standard bridge clearances heights in the United States. The vessel, along with all fuel and structural materials within, is calculated to weigh 31.5 tons. Therefore, the vessel alone is well within both the technical and statutory limits for transportation by a large commercial semi-trailer. While each U.S. state has its own laws governing heavy shipping, it is possible for the turbomachine to accompany the reactor vessel on the same trailer[58]. A turbomachine of comparable power output with multistage compressors and turbines can have a shaft length of just a few meters[59]. Siemens advertises a 7.9 MWe gas turbine in which the compressor-turbine-generator package is 11.25 m in length, 3.5 m tall, 2.85 m wide, and weighs 85 tons[60]. Because of the high density of the reactor and turbomachine materials, the unit would easily fit within permissible U.S. oversize shipping dimensions, but the cargo weight of 116.5 tons, while also permissible, would subject the unit to strict technical and statutory restrictions regarding the number and rating of trailer axles required for shipping by road[58].

An air-to-air heat exchanger capable of cooling 104 $\frac{kg}{s}$ of primary coolant from 495.56 K to 296 K would have a large volume, and may require its own vehicle for shipment. Examples of heat exchangers of this capability are designed to occupy the space of a standard shipping container[38,61].

The diameter of the reactor system including the 239 cm water shielding layer, but not the lead, is 620 cm. To make transportation of the water shielding easier, in terms of weight and shipping width, the containment for the shielding water can be shipped separately. The 94.5 tons, or 21,446 gallons, of water to fill the shielding can also be carried by as few as two vehicles separately from the reactor.

The lead shielding, which is 39.7 cm thick, makes the entire reactor system 7 m in diameter. The weight of this lead shielding, however, will be 367.6 tons. This lead shielding, therefore, would need to be shipped in sections, and assembled on site.

The total weight of the system is estimated to be 578.6 tons, which includes the reactor vessel, fuel, cladding, shielding, and turbomachine assembly. The convoy carrying the main system components would need to be approximately 10 vehicles: one for the reactor, one for the compressor-turbine-generator assembly, one for the heat exchanger, two tankers for the shielding water, at least four[58] vehicles to transport lead-shielding sections, plus a crane and other material-handling equipment to assemble the system. This does not include ancillary equipment such as tools, piping, wiring, crew accommodations, emergency cooling generators (minimum 23.9 kW capacity, as calculated in section 4.9), or the mission-related equipment to be powered by the reactor system.

5. DESIGN SUMMARY

The most efficient AGFR design compiled in this thesis has a net thermodynamic efficiency of 37.5 %. The AGFR is composed of just under a ton of UOX fuel, enriched to 50% U235 in order to support a fast spectrum. The cladding selected for the design is SiC, in order to support high neutron fluences, high temperatures, and corrosion resistance. The reactor is nearly infinitely reflected with a steel vessel, surrounded by a neutron shielding tank, which can be filled with water. Additional lead shielding for gamma radiation is placed outside the water shielding.

The reactor unit is coupled to a closed, recuperated, direct Brayton cycle, the details of which are shown in Figures 37 and 38.

The reactor is shielded with 239 cm of water in the radial direction, and 39.7 cm of lead in the radial direction. It is shielded with 16.78 cm of water and 7.03 cm of lead on the top and bottom of the vessel.

System characteristics for the reactor in its optimal operating mode are listed in Table 11.

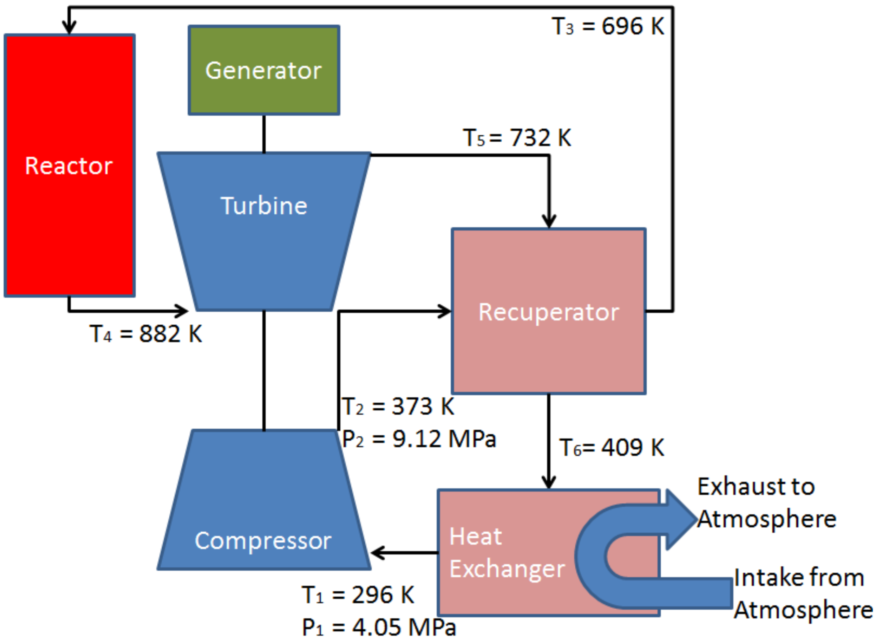

Figure 37. Air-cooled Gas Fast Reactor’s Brayton cycle diagram.

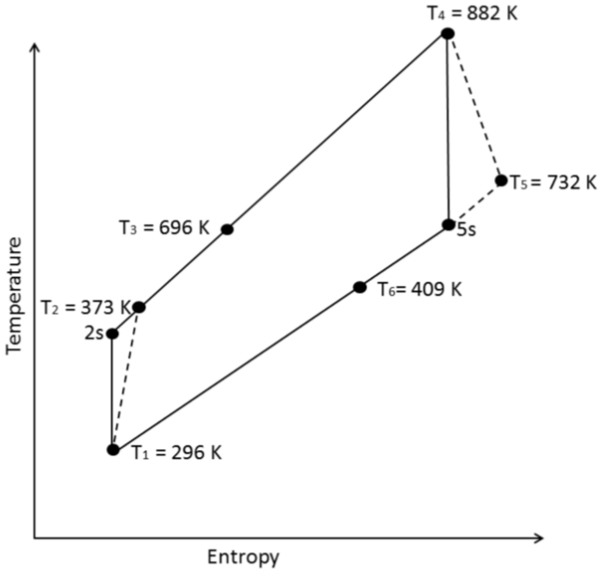

Figure 38. Air-cooled Gas Fast Reactor’s Brayton cycle T-s diagram.

Table 11. Air-Cooled Fast Reactor Parameters for Maximum Efficiency

Air-Cooled Fast Reactor Characteristic	Value
Active Core Height, H [m]	0.5
Core Thermal Power, *Q* [MW]	30
UOX Fuel U235 Enrichment [Weight Fraction of Uranium]	0.5
Total Number of Control Rods in Core	481
Total Number of Fuel Rods in Core	7266
Radius Inscribing Core [m]	0.409
Mass of Fuel in Core [kg]	991
Pitch-to-Diameter Ratio, p/d	1.15
Core Power Density [W/cm^3]	139
Hot Channel Factor $F_{q,FC}$	1.552
Mass Flow Rate of Coolant (Active Core Total), w [kg/s]	145
Reynolds Number, Re	112311
Heat Exchanger Outlet / Compressor Inlet Temp., T_1 [K]	296
Heat Exchanger Outlet / Compressor Inlet Pressure [atm]	40
Compression Ratio, r_c	2.25
Primary Coolant Mass Flow Rate, w [kg/s]	145.23
Peak Clad Temperature, $T_{Cl,Max}$ [K] (SiC)	1173.15
Peak Fuel Temperature, $T_{f,Max}$ [K] (UO2)	1535.61
Compressor Outlet / Recuperator Inlet Temp., T_2 [K]	372.72
Recuperator Outlet / Reactor Inlet Temp., T_3 (or $T_{b,in}$) [K]	696.00
Average Reactor Outlet / Turbine Inlet Temp., T_4 [K]	882.09
Turbine Outlet / Recuperator Inlet Temp., T_5 [K]	731.93
Recuperator Outlet / Heat Exchanger Inlet Temp., T_6 [K] (Closed Cycle)	408.64
Average Coolant Velocity, v [m/s]	25.580
Maximum Coolant Velocity, v_{max} [m/s]	28.57
Gross Thermodynamic Efficiency, ζ	0.395
Pumping Power to Operate Heat Exchanger, P_{pump} [MW]	0.449
Pumping Power to Overcome Friction, P_{fric} [MW]	0.133
Net Thermodynamic Efficiency, ζ_{net}	0.375
BOL k_{eff} at Cold Shutdown	0.950
Burnup Achievable [GWd/tHM]	39
Maximum Core Lifetime [days]	907
Mass of Reactor Including Steel Vessel / Reflector [kg]	31529
Mass of Shielding [kg]	462113
Estimated mass of power plant components [kg]	85000
Height of Reactor Unit, Including Shielding [m]	3.43

6. CONCLUSIONS

To complete this thesis, it must be answered whether the air-cooled fast reactor design concept remains feasible and suitable for the purpose of providing temporary power generation at remote locations, given the results of the simulations and calculations conducted in this thesis.

Neutronics simulations confirm that an unmoderated core containing less than one ton of HEU can produce 30 MW of thermal power for up to 907 days, reaching a burnup of 39 $\frac{GWd}{tHM}$, while maintaining a 5% shutdown reactivity margin. It can also be concluded that the reactor is controllable at all points in its lifetime, using both control rods and burnable poisons. Furthermore, it has built-in negative reactivity feedback parameters.

Modeling of the core thermal hydraulics indicates that the core can be cooled in the event of a DLOCA with a mass flow rate of 145 $\frac{kg}{s}$ of air entering a compressor at 296 K. This would maintain a steady-state peak cladding temperature of 1173 K. If the cladding material is SiC, a 600 K safety margin for transients remains. Still, if no heat were removed following the DLOCA and SCRAM, the core temperature would rise by an average of 600 K within minutes. During a DLOCA, with a SCRAM, the core could be cooled directly by unpressurized air at 296 K if approximately 23.9 kW of pumping power remains available. This requirement drops to approximately 75.5 W after 2.4 hours. This is a highly conservative estimate because it neglects heat transfer to the reactor vessel and the cooling channels in the control rod assemblies and outside the active core, and also contains the unrealistic assumption that no engineered safety mechanisms are available to assist with core cooling via conduction or liquid convection.

The possibility of an open-cycle operating mode was discussed. Calculations were performed to determine whether the production of Argon-41 would lead to a prohibitive dose. While the dose due to Argon-41 alone would likely be a large fraction of the statutory occupational dose of $0.05\ \frac{Sv}{yr}$, it is not likely to be a harmful dose. To operate in this mode, however, would require the development of fuel elements that retain their fission products reliably enough that there is little risk of them entering the primary coolant. Argon-41 also builds up in the closed cycle, essentially in the same quantities as if the exhaust cloud from the open cycle were retained and recycled. Therefore, while the closed loop is less likely to result in any significant environmental impact, it may be necessary to shield the primary coolant loop.

Regarding the choice of an open or closed Brayton cycle, the utility of the open cycle operating mode was overestimated at the beginning of this thesis, because the calculations in section 4.10 lead to the conclusion that the closed Brayton cycle is thermodynamically superior to the open cycle, because the benefits of a pressurized system outweigh the thermal benefits of eliminating the heat exchanger. The closed Brayton cycle has an additional thermodynamic advantage over the open cycle, which is that the open cycle's Argon-activated exhaust must be dissipated, while the closed cycle may be able to facilitate heating applications. Assuming 95% efficiency of pumps and 90% efficiency of all other components, a closed, direct Brayton cycle coupled to this reactor could operate at a system pressure of 90 atm and achieve a maximum Net Thermodynamic Efficiency of 37.5%.

Because this system uses HEU as its fuel, its post-irradiation specific activity is lower than that of used PWR fuel of similar burnup. While it may be tempting to consider this an indication of environmental friendliness, note that the used fast reactor fuel remains HEU, and that lower radioactivity also makes this material easier to steal, transport, smuggle undetected, and fashion into a weapon. For this reason, the design concept proposed here would rely heavily upon loss-prevention, as opposed to self-shielding. Other options would be to fully optimize the design in order to reduce the necessary enrichment, and to ensure that the used fuel contains more nuclides that provide the desired self-shielding effect. To reduce the enrichment of the fuel to LEU levels would likely be possible, but it would add several tons of fuel to the core, increasing the mass and volume of reflector and shielding material as well. Furthermore, it would be difficult to achieve burnup similar to that achieved in these simulations. Additional studies are needed on the security and proliferation aspects of this core concept.

Transportation of the system to and from a mission site can be accomplished by truck, if the 578.6 ton system is shipped in at least ten “superheavy”[58] tractor-trailer loads, over half of which are to accommodate shielding for neutrons and photons. While the reactor system described in this thesis would require intense efforts to transport, install, and retrieve, once installed, it could operate with little regular logistical support. The system would be capable of providing 11.25 MW of electrical power, plus heating, for a mission lasting up to 907 full-power-days, without refueling, without consuming water from local sources, and without the maintenance of an exotic coolant supply.

REFERENCES

1. IAEA, *Status of Small and Medium Sized Reactor Designs*, 1 ed. (International Atomic Energy Agency, Vienna, Austria, 2012).

2. N. E. TODREAS, and M. S. KAZIMI, *Nuclear Systems*, 2 ed. (CRC Press, Boca Raton, FL, 2012).

3. A. E. WALTAR, and A. REYNOLDS, *Fast Spectrum Reactors*, 2 ed. (Springer Science+Business Media, New York, 2012).

4. J. G. COLLIER, and J. J. THOME, *Convective Boiling and Condensation*, 3 ed. (Oxford University Press, Oxford, UK, 2001).

5. R. LAUBSCHER, and R. T. DOBSON, "Theoretical and experimental modelling of a heat pipe heat exchanger for high temperature nuclear reactor technology," *Applied Thermal Engineering*, 61, 259-267 (2013).

6. E. GREENSPAN, *Solid-Core Heat-Pipe Nuclear Battery Type Reactor*, 1 ed. (University of California, Berkeley, CA, 2008).

7. C. R. F. AZEVEDO, "Selection of fuel cladding material for nuclear fission reactors," *Engineering Failure Analysis*, 18, 1943-1962 (2011).

8. C. DURIEZ, T. DUPONT, B. SCHMET, and F. ENOCH, "Zircaloy-4 and M5® high temperature oxidation and nitriding in air," *Journal of Nuclear Materials*, 380, 30-45 (2008).

9. G. C. ALLEN, J. M. DYKE, S. J. HARRIS, and A. MORRIS, "The oxidation of Inconel-690 alloy at 600 K in air," *Applied Surface Science*, 31, 220-238 (1988).

10. K. GUERFI, S. LAGERGE, M. J. MEZIANI, Y. NEDELLEC, and G. CHAUVETEAU, "Influence of the oxidation on the surface properties of silicon carbide," *Thermochimica Acta*, 434, 140-149 (2005).

11. C. BASSI, P. AZRIA, and M. BALMAIN, "Level 1 probabilistic safety assessment to support the design of the CEA 2400MWth gas-cooled fast reactor," *Nuclear Engineering and Design*, 240, 3758-3780 (2010).

12. G. MELESE-D'HOSPITAL, and R. H. SIMON, "Status of Gas-Cooled Fast Breeder Reactor Programs," *Nuclear Engineering and Design*, 40, 5-12 (1977).

13. T. Q. FOLEY, and T. W. KNIGHT, "Fuel cycle analysis of GFR using advanced fuels," *Progress in Nuclear Energy*, 51, 109-123 (2009).

14. A. K. NAYAK, and R. K. SINHA, "Role of passive systems in advanced reactors," *Progress in Nuclear Energy*, 49, 486-498 (2007).

15. M. A. POPE, J. I. LEE, P. HEJZLAR, and M. J. DRISCOLL, "Thermal hydraulic challenges of Gas Cooled Fast Reactors with passive safety features," *Nuclear Engineering and Design*, 239, 840-854 (2009).

16. F. CARRE, P. YVON, P. ANZIEU, N. CHAUVIN, and J.-Y. MALO, "Update of the French R&D strategy on gas-cooled reactors," *Nuclear Engineering and Design*, 240, 2401-2408 (2010).

17. Korea Atomic Energy Research Institute, "Table of Nuclides"; available on the Internet at http://atom.kaeri.re.kr; accessed March 17, 2014.

18. C. SUTOUR, C. STUMPF, J. P. KOSINSKI, A. SURGET, G. HERVOUËT, C. YARDIN, T. MADEC, and A. GOSSET, "Determination of the argon concentration in ambient dry air for the calculation of air density," *Metrologia*, 44, 448-452 (2007).

19. P. HEJZLAR, N. E. TODREAS, E. SHWAGERAUS, A. NIKIFOROVA, R. PETROSKI, and M. J. DRISCOLL, "Cross-comparison of fast reactor concepts with various coolants," *Nuclear Engineering and Design*, 239, 2672-2691 (2009).

20. N. TAUVERON, M. SAEZ, M. MARCHAND, T. CHATAING, G. GEFFRAYE, and C. BASSI, "Transient thermal–hydraulic simulations of direct cycle gas cooled reactors," *Nuclear Engineering and Design*, 235, 2527-2545 (2005).

21. C. F. MCDONALD, "Helium turbomachinery operating experience from gas turbine power plants and test facilities," *Applied Thermal Engineering*, 44, 108-142 (2012).

22. M. J. MORAN, and H. N. SHAPIRO, *Fundamentals of Engineering Thermodynamics*, 5 ed. (John Wiley & Sons, Inc., Hoboken, NJ, 2004).

23. C. H. OH, and E. S. KIM, "Conceptual study on air ingress mitigation for VHTRs," *Nuclear Engineering and Design*, 250, 448-464 (2012).

24. X-5 Monte Carlo Team, *MCNP--A General Monte Carlo N-Particle Transport Code, Version 5*, 1 ed. (X-5 Monte Carlo Team, Los Alamos National Security, LLC, Los Alamos, NM, 2008).

25. D. B. PELOWITZ, *MCNPX User's Manual*, 2.7.0 ed. (Los Alamos National Security, LLC, Los Alamos, NM, 2011).

26. J. L. KLOOSTERMAN, "Design Criteria for the HTR Core"; available on the Internet at http://www.janleenkloosterman.nl/reports/vhtr_course_slides_200811.pdf; accessed December 2, 2013.

27. W. J. STEIN, and T. R. NEUMAN, "Mitigation Strategies for Design Exceptions," Report number FHWA-SA-07-011, U.S. Department of Transportation (Federal Highway Administration, Office of Safety, Washington, D.C., 2007).

28. J. R. LAMARSH, and A. J. BARATTA, *Introduction to Nuclear Engineering*, 3 ed. (Prentice Hall, Inc., Upper Saddle River, NJ, 2001).

29. K. KADOYA, N. MATSUNAGA, and A. NAGASHIMA, "Viscosity and Thermal Conductivity of Dry Air in the Gaseous Phase," *Journal of Physical and Chemical Reference Data*, 14, 947-970 (1985).

30. D. A. KOUREMENOS, and K. A. ANTONOPOULOS, "Sound velocity and isentropic exponents of real air on its compressibility chart," *International Journal of Heat and Fluid Flow*, 12, 137-141 (1991).

31. D. K. EDWARDS, V. E. DENNY, and A. F. MILLS, *Transfer Processes*, 2 ed. (Hold, Rinehart, Winston, Inc., New York, 1973).

32. B. MIHAILA, M. STAN, and J. CRAPPS, "Impact of thermal conductivity models on the coupling of heat transport and oxygen diffusion in UO2 nuclear fuel elements," *Journal of Nuclear Materials*, 430, 221-228 (2012).

33. P. YARSKY, "Core Design and Reactor Physics of a Breed and Burn Gas-cooled Fast Reactor," *Department of Nuclear Engineering*, (Massachusetts Institute of Technology, Cambridge, MA, 2005).

34. R. NAVE, Department of Physics and Astronomy, "Speed of Sound in Air"; available on the Internet at http://hyperphysics.phy-astr.gsu.edu/hbase/sound/souspe.html; accessed January 22, 2014.

35. K. FUKUDA, J. KENDALL, and J. KUPITZ, *Current status and future development of modular high temperature gas cooled reactor technology*, 1 ed. (IAEA, Vienna, Austria, 2001).

36. Y. A. CENGEL, and M. A. BOLES, *Thermodynamics: An Engineering Approach*, 7 ed. (McGraw-Hill, New York, 2011).

37. M. P. LABAR, "Status of the GT-MHR for Electricity Production," *Proc. World Nuclear Association Annual Symposium* (London, UK, 3-5 September, 2003).

38. Greenheck Fan Corporation, "Greenheck: Building Value in Air"; available on the Internet at http://www.greenheck.com/media/pdf/AllProducts_catalog.pdf; accessed March 3, 2014.

39. L. L. SNEAD, T. NOZAWA, Y. KATOH, T.-S. BYUN, S. KONDO, and D. A. PETTI, "Handbook of SiC properties for fuel performance modeling," *Journal of Nuclear Materials*, 371, 329-377 (2007).

40. R. L. KLUEH, and A. T. NELSON, "Ferritic/martensitic steels for next-generation reactors," *Journal of Nuclear Materials*, 371, 37-52 (2007).

41. V. P. BOBKOV, L. R. FOKIN, E. E. PETROV, V. V. POPOV, V. N. RUMIANTSEV, and A. I. SAVVATIMSKY, *Thermophysical Properties of Materials for Nuclear Engineering: A Tutorial and Collection of Data*, 1 ed. (International Atomic Energy Agency, Vienna, Austria, 2008).

42. J. A. JUNG, S. H. KIM, S. H. SHIN, I. C. BANG, and J. H. KIM, "Feasibility study of fuel cladding performance for application in ultra-long cycle fast reactor," *Journal of Nuclear Materials*, 440, 596-605 (2013).

43. D. W. SHOESMITH, and D. ZAGIDULIN, "The corrosion of zirconium under deep geologic repository conditions," *Journal of Nuclear Materials*, 418, 292-306 (2011).

44. J. J. SIENICKI, A. V. MOISSEYTSEV, P. A. PFEIFFER, W. S. YANG, M. A. SMITH, S. J. KIM, Y. D. BODNAR, D. C. WADE, and L. L. LEIBOWITZ, "SSTAR Lead-Cooled, Small Modular Fast Reactor with Nitride Fuel," *Proc. Workshop on Advanced Reactors with Innovative Fuels* (Oak Ridge, TN, February 16-18, 2005).

45. Y. ETOH, and S. SHIMADA, "Neutron irradiation effects on intermetallic precipitates in Zircaloy as a function of fluence," *Journal of Nuclear Materials*, 200, 59-69 (1993).

46. J. ORTIZ-VILLAFUERTE, *Towards a Cleaner Planet*, 1 ed. (Springer, Berlin, Germany, 2007).

47. R. W. POWELL, D. T. PETERSON, M. K. ZIMMERSCHIED, and J. F. BATES, "Swelling of several commercial alloys following high fluence neutron irradiation," *Journal of Nuclear Materials*, 104, 969-973 (1981).

48. C. A. BALDWIN, and M. J. KANIA, "Fission product retention in TRISO coated UO2 particle fuels subjected to HTR simulated core heating tests," *International Nuclear Information System*, 33, (1990).

49. J. W. AANENSON, "Savannah River Site Environmental Dose Reconstruction Project " Report number 1-CDC-SRS-1999-Final, Center for Disease Control (Center for Disease Control, Neeses, SC, 2001).

50. A. N. FEDOROV, "Investigation and improvement of cryogenic adsorption purification of argon from oxygen," *Gas Separation & Purification*, 9, 137-145 (1995).

51. C. D. BERGER, Integrated Environmental Management, Inc., "Specific Activities"; available on the Internet at http://www.iem-inc.com/toolspa.html; accessed September 9, 2013.

52. U.S. Nuclear Regulatory Commission, "Occupational Dose Limits"; available on the Internet at http://www.nrc.gov/reading-rm/doc-collections/cfr/part020/part020-1201.html; accessed January 19, 2014.

53. ATOMIC ENERGY CONTROL BOARD, *Radioactive Release Data from Canadian Nuclear Generating Stations 1972 to 1986*, 2 ed. (Radiation Protection Division, Ottowa, Canada, 1986).

54. A. GALPERIN, P. GRIMM, and V. RAIZES, "Modelling and verification of the PWR burnable poison designs by ELCOS code system," *Annals of Nuclear Energy*, 22, 317-325 (1995).

55. DOE, "Nuclear Physics and Reactor Theory," Report number DOE-HDBK-1019/2-93, Department of Energy (Department of Energy, Washington, D.C., 1993).

56. R. E. NAEGELI, *Calculation of the Radionuclides in PWR Spent Fuel Samples for SFR Experiment Planning*, 1 ed. (Sandia National Laboratories, Albuquerque, NM, 2004).

57. IAEA, *Nuclear Research Reactors in the World*, 3 ed. (International Atomic Energy Agency, Vienna, Austria, 2000).

58. Texas Department of Motor Vehicles., "Texas Department of Motor Vehicles"; available on the Internet at http://txdmv.gov/; accessed February 22, 2014.

59. M. S. EL-GENK, and J. M. TOURNIER, "Effects of working fluid and shaft rotation speed on the performance of HTR plants and the size of CBC turbo-machine," *Nuclear Engineering and Design*, 239, 1811-1827 (2009).

60. B. M. IGOE, C. ENGELBERT, K. SCOTT, S. CHARLTON, and T. MAPLESTON, "Design and Early Development of the SGT-300 Twin Shaft Gas Turbine," *Proc. 19th Symposium of the Industrial Application of Gas Turbines Committee* (Banff, Alberta, Canada, October 17, 2011).

61. Pre-heat, Inc., "Pre-heat, Inc.: Industrial Air to Air Heat Exchangers"; available on the Internet at http://www.pre-heat.com/index.html; accessed February 22, 2014.

62. N. SOPPERA, Nuclear Energy Agency, "Java-based Nuclear Data Information System"; available on the Internet at http://www.oecd-nea.org/janis/; accessed March 16, 2014.

APPENDIX A

Table 12 contains the detailed post-irradiation nuclide inventories that were summarized in Table 10. Quantities are in units of Ci/g, Curies per gram of fuel.

Table 12. Radionuclide Inventories in Used Fuel

Nuclide Identifier	**Nuclide**	**AGFR 75.3 GWd / tHM**	**AGFR 120 GWd / tHM**	**AGFR 75.3 GWd / tHM + 8 yr decay**	**AGFR 120 GWd / tHM + 8 yr decay**	**PWR 38.6 GWd / tHM + 22 yr decay**	**PWR 72 GWd / tHM + 8 yr decay**
98252	Cf252	0.00E+00	6.08E-27	0.00E+00	7.48E-28	0.00E+00	1.25E-08
98251	Cf251	1.27E-31	9.55E-27	1.26E-31	9.49E-27	0.00E+00	1.87E-10
98250	Cf250	7.42E-30	1.60E-22	4.87E-30	1.05E-22	0.00E+00	1.61E-08
98249	Cf249	6.23E-31	2.14E-22	6.20E-31	5.65E-22	0.00E+00	4.41E-09
97249	Bk249	0.00E+00	1.44E-19	0.00E+00	2.58E-22	0.00E+00	2.37E-09
97248	Bk248	0.00E+00	1.16E-24	0.00E+00	0.00E+00	0.00E+00	0.00E+00
97247	Bk247	0.00E+00	2.67E-30	0.00E+00	2.66E-30	0.00E+00	0.00E+00
96248	Cm248	1.51E-25	3.30E-22	1.18E-24	3.30E-22	0.00E+00	2.36E-10
96247	Cm247	2.50E-24	1.28E-21	9.28E-24	1.28E-21	0.00E+00	3.18E-11
96246	Cm246	8.12E-18	9.44E-16	1.20E-17	9.43E-16	1.04E-07	4.08E-06
96245	Cm245	1.25E-15	7.34E-14	2.10E-15	7.33E-14	3.42E-07	6.10E-06
96244	Cm244	7.31E-11	2.64E-09	7.18E-11	1.94E-09	1.94E-03	3.30E-02
96243	Cm243	9.90E-11	1.93E-09	1.18E-10	1.59E-09	1.25E-05	3.15E-04
96242	Cm242	2.03E-06	2.12E-05	2.27E-09	2.06E-08	5.37E-06	3.32E-05
96241	Cm241	7.60E-13	1.03E-11	0.00E+00	0.00E+00	0.00E+00	3.18E-32
95244	Am244	1.66E-09	4.06E-08	0.00E+00	0.00E+00	0.00E+00	0.00E+00
95243	Am243	1.44E-11	2.24E-10	1.65E-11	2.24E-10	3.20E-05	1.33E-04
95242	Am242	2.03E-09	2.58E-08	2.74E-09	2.48E-08	6.49E-06	3.87E-05
95241	Am241	3.26E-07	2.24E-06	2.37E-06	8.32E-06	3.01E-03	2.57E-03
95240	Am240	6.44E-10	6.63E-09	0.00E+00	0.00E+00	0.00E+00	0.00E+00
94245	Pu245	8.84E-16	3.20E-14	0.00E+00	0.00E+00	0.00E+00	0.00E+00
94244	Pu244	5.53E-21	1.21E-19	6.55E-21	1.21E-19	0.00E+00	0.00E+00
94243	Pu243	1.35E-07	1.20E-06	9.28E-24	1.28E-21	5.81E-13	3.18E-11
94242	Pu242	4.36E-11	3.47E-10	5.69E-11	3.47E-10	2.61E-06	6.09E-06

Table 12 (continued). Radionuclide Inventories in Used Fuel

Nuclide Identifier	Nuclide	AGFR 75.3 GWd / tHM	AGFR 120 GWd / tHM	AGFR 75.3 GWd / tHM + 8 yr decay	AGFR 120 GWd / tHM + 8 yr decay	PWR 38.6 GWd / tHM + 22 yr decay	PWR 72 GWd / tHM + 8 yr decay
94241	Pu241	1.53E-04	5.79E-04	1.26E-04	3.94E-04	4.71E-02	1.29E-01
94240	Pu240	2.41E-05	6.52E-05	2.42E-05	6.52E-05	5.24E-04	6.64E-04
94239	Pu239	4.69E-04	7.37E-04	4.72E-04	7.38E-04	2.93E-04	3.25E-04
94238	Pu238	2.26E-04	8.03E-04	2.20E-04	7.56E-04	2.74E-03	1.40E-02
94237	Pu237	1.83E-06	2.91E-06	3.12E-26	1.01E-25	0.00E+00	5.57E-25
94236	Pu236	1.71E-07	5.30E-07	2.65E-08	7.86E-08	2.47E-09	2.43E-07
93239	Np239	3.19E+00	3.61E+00	1.65E-11	2.24E-10	3.20E-05	1.33E-04
93238	Np238	1.29E-02	3.33E-02	1.23E-11	1.12E-10	2.93E-08	1.94E-07
93237	Np237	2.29E-07	5.15E-07	2.38E-07	5.18E-07	3.37E-07	5.27E-07
93236	Np236	1.07E-10	4.16E-10	1.23E-10	4.16E-10	0.00E+00	0.00E+00
93235	Np235	2.08E-08	7.02E-09	2.97E-11	4.24E-11	1.71E-14	8.09E-11
92240	U240	3.01E-16	1.23E-19	6.54E-21	1.21E-19	0.00E+00	7.92E-12
92239	U239	3.19E+00	3.61E+00	0.00E+00	0.00E+00	0.00E+00	0.00E+00
92238	U238	1.45E-07	1.42E-07	1.45E-07	1.42E-07	2.78E-07	2.68E-07
92237	U237	2.07E-01	3.41E-01	3.01E-09	9.42E-09	1.13E-06	3.16E-06
92236	U236	8.76E-07	1.37E-06	8.80E-07	1.37E-06	2.41E-07	2.15E-07
92235	U235	7.74E-07	6.75E-07	7.74E-07	6.75E-07	1.12E-08	1.72E-09
92234	U234	6.14E-07	9.67E-07	6.43E-07	9.84E-07	9.74E-07	8.40E-07
92233	U233	8.93E-10	1.08E-09	9.92E-10	1.10E-09	0.00E+00	3.80E-11
92232	U232	7.45E-09	2.03E-08	1.14E-08	3.66E-08	2.21E-08	1.27E-07
92231	U231	5.75E-13	8.64E-13	0.00E+00	0.00E+00	0.00E+00	0.00E+00
92230	U230	8.39E-12	1.60E-11	0.00E+00	0.00E+00	0.00E+00	0.00E+00
92229	U229	1.38E-17	3.92E-17	0.00E+00	0.00E+00	0.00E+00	0.00E+00
91233	Pa233	6.30E-07	9.05E-07	2.38E-07	5.18E-07	3.37E-07	5.27E-07
91232	Pa232	9.71E-08	1.59E-07	0.00E+00	0.00E+00	0.00E+00	0.00E+00
91231	Pa231	1.21E-10	1.72E-10	2.50E-10	2.86E-10	0.00E+00	4.49E-11
91230	Pa230	8.95E-11	1.70E-10	0.00E+00	0.00E+00	0.00E+00	0.00E+00
91229	Pa229	7.03E-13	6.22E-14	0.00E+00	0.00E+00	0.00E+00	0.00E+00
90234	Th234	3.02E-07	2.71E-07	1.45E-07	1.42E-07	2.78E-07	2.68E-07
90233	Th233	1.29E-07	2.17E-07	0.00E+00	0.00E+00	0.00E+00	0.00E+00
90232	Th232	6.73E-16	1.12E-15	9.87E-16	1.66E-15	0.00E+00	0.00E+00
90231	Th231	9.53E-07	8.42E-07	7.74E-07	6.75E-07	1.12E-08	1.72E-09

Table 12 (continued). Radionuclide Inventories in Used Fuel

Nuclide Identifier	Nuclide	AGFR 75.3 GWd / tHM	AGFR 120 GWd / tHM	AGFR 75.3 GWd / tHM + 8 yr decay	AGFR 120 GWd / tHM + 8 yr decay	PWR 38.6 GWd / tHM + 22 yr decay	PWR 72 GWd / tHM + 8 yr decay
90230	Th230	1.72E-11	4.36E-11	6.48E-11	1.15E-10	0.00E+00	1.06E-10
90229	Th229	1.75E-13	6.63E-13	9.75E-13	1.43E-12	0.00E+00	0.00E+00
90228	Th228	3.00E-09	1.04E-08	1.01E-08	3.30E-08	0.00E+00	1.16E-07
90227	Th227	1.09E-11	2.54E-11	4.94E-11	7.00E-11	0.00E+00	0.00E+00
89228	Ac228	1.02E-12	2.55E-12	6.43E-16	1.32E-15	0.00E+00	0.00E+00
89227	Ac227	1.11E-11	2.52E-11	5.05E-11	7.15E-11	0.00E+00	0.00E+00
89226	Ac226	3.18E-14	8.38E-14	0.00E+00	0.00E+00	0.00E+00	0.00E+00
89225	Ac225	2.45E-13	9.80E-13	9.64E-13	1.41E-12	0.00E+00	0.00E+00
88227	Ra227	1.11E-13	6.26E-13	0.00E+00	0.00E+00	0.00E+00	0.00E+00
88226	Ra226	1.50E-14	6.05E-14	1.58E-13	3.35E-13	0.00E+00	0.00E+00
88225	Ra225	2.50E-13	9.89E-13	9.67E-13	1.42E-12	0.00E+00	0.00E+00
88224	Ra224	2.88E-09	9.92E-09	1.01E-08	3.29E-08	0.00E+00	1.16E-07
84210	Po210	4.33E-19	5.85E-18	9.12E-19	4.17E-18	2.35E-25	0.00E+00
84209	Po209	4.71E-26	9.87E-25	4.73E-26	9.35E-25	0.00E+00	0.00E+00
83210	Bi210m	5.96E-19	7.69E-18	9.59E-19	4.34E-18	4.86E-16	4.04E-14
83209	Bi209	7.29E-34	9.45E-33	5.67E-34	9.45E-33	0.00E+00	0.00E+00
83208	Bi208	3.22E-25	8.78E-24	3.05E-25	8.78E-24	0.00E+00	6.55E-14
82210	Pb210	1.74E-19	1.34E-18	9.60E-19	4.35E-18	0.00E+00	0.00E+00
82209	Pb209	8.25E-15	8.13E-14	2.25E-22	8.86E-22	0.00E+00	0.00E+00
82208	Pb208	0.00E+00	0.00E+00	0.00E+00	0.00E+00	0.00E+00	0.00E+00
82207	Pb207	0.00E+00	0.00E+00	0.00E+00	0.00E+00	0.00E+00	0.00E+00
81205	Tl205	0.00E+00	0.00E+00	0.00E+00	0.00E+00	0.00E+00	0.00E+00
80204	Tl204	0.00E+00	0.00E+00	0.00E+00	0.00E+00	0.00E+00	0.00E+00
64154	Eu154	0.00E+00	0.00E+00	0.00E+00	0.00E+00	1.18E-03	1.48E-02
61147	Pm147	0.00E+00	0.00E+00	0.00E+00	0.00E+00	4.83E-04	9.72E-03
60145	Nd145	6.43E-17	1.01E-16	6.44E-17	1.01E-16	0.00E+00	0.00E+00
60143	Nd143	0.00E+00	0.00E+00	0.00E+00	0.00E+00	0.00E+00	0.00E+00
59141	Pr141	0.00E+00	0.00E+00	0.00E+00	0.00E+00	0.00E+00	0.00E+00
58141	Ce141	0.00E+00	1.42E+00	1.03E-13	2.87E-13	0.00E+00	6.57E-28
58140	Ce140	0.00E+00	0.00E+00	0.00E+00	0.00E+00	0.00E+00	0.00E+00
58139	Ce139	0.00E+00	1.34E-04	2.74E-11	5.53E-11	5.75E-25	0.00E+00
58138	Ce138	0.00E+00	0.00E+00	0.00E+00	0.00E+00	0.00E+00	0.00E+00

Table 12 (continued). Radionuclide Inventories in Used Fuel

Nuclide Identifier	Nuclide	AGFR 75.3 GWd / tHM	AGFR 120 GWd / tHM	AGFR 75.3 GWd / tHM + 8 yr decay	AGFR 120 GWd / tHM + 8 yr decay	PWR 38.6 GWd / tHM + 22 yr decay	PWR 72 GWd / tHM + 8 yr decay
57139	La139	0.00E+00	0.00E+00	0.00E+00	0.00E+00	0.00E+00	0.00E+00
57138	La138	0.00E+00	2.68E-15	1.03E-15	2.68E-15	0.00E+00	0.00E+00
56138	Pr138	0.00E+00	0.00E+00	0.00E+00	0.00E+00	0.00E+00	0.00E+00
56137	Ba137m	0.00E+00	0.00E+00	0.00E+00	0.00E+00	6.34E-02	1.28E-01
56136	Ba136	0.00E+00	0.00E+00	0.00E+00	0.00E+00	0.00E+00	0.00E+00
55137	Cs137	2.00E-01	3.06E-01	1.66E-01	2.54E-01	6.71E-02	1.36E-01
55136	Cs136	0.00E+00	3.83E-02	1.47E-15	4.04E-15	0.00E+00	0.00E+00
55135	Cs135	0.00E+00	4.75E-06	3.00E-06	4.75E-06	3.68E-07	8.28E-07
55134	Cs134	0.00E+00	5.68E-02	1.75E-03	3.87E-03	1.06E-04	2.05E-02
55133	Cs133	0.00E+00	0.00E+00	0.00E+00	0.00E+00	0.00E+00	0.00E+00
54135	Xe135	0.00E+00	1.63E+00	1.27E-13	3.47E-13	0.00E+00	0.00E+00
54134	Xe134	0.00E+00	0.00E+00	0.00E+00	0.00E+00	0.00E+00	0.00E+00
54133	Xe133	0.00E+00	1.63E+00	1.15E-13	3.11E-13	0.00E+00	0.00E+00
54131	Xe131	0.00E+00	0.00E+00	0.00E+00	0.00E+00	0.00E+00	0.00E+00
44101	Ru101	0.00E+00	0.00E+00	0.00E+00	0.00E+00	0.00E+00	0.00E+00
43099	Tc99	2.85E-05	4.47E-05	2.86E-05	4.48E-05	1.36E-05	2.03E-05
42095	Mo95	0.00E+00	0.00E+00	0.00E+00	0.00E+00	0.00E+00	0.00E+00
40093	Zr93	4.14E-06	6.57E-06	4.15E-06	6.57E-06	1.18E-06	2.90E-06
39090	Y90	0.00E+00	0.00E+00	0.00E+00	0.00E+00	4.38E-02	6.84E-02
38090	Sr90	0.00E+00	0.00E+00	0.00E+00	0.00E+00	4.38E-02	6.84E-02
10020	Ne20	0.00E+00	0.00E+00	0.00E+00	0.00E+00	0.00E+00	0.00E+00
9019	F19	0.00E+00	0.00E+00	0.00E+00	0.00E+00	0.00E+00	0.00E+00
9018	F18	1.50E-22	6.56E-22	0.00E+00	0.00E+00	0.00E+00	0.00E+00
8018	O18	0.00E+00	0.00E+00	0.00E+00	0.00E+00	0.00E+00	0.00E+00
8017	O17	0.00E+00	0.00E+00	0.00E+00	0.00E+00	0.00E+00	0.00E+00
8016	O16	0.00E+00	0.00E+00	0.00E+00	0.00E+00	0.00E+00	0.00E+00
7016	N16	3.13E-04	5.73E-04	0.00E+00	0.00E+00	0.00E+00	0.00E+00
7015	N15	0.00E+00	0.00E+00	0.00E+00	0.00E+00	0.00E+00	0.00E+00
7014	N14	0.00E+00	0.00E+00	0.00E+00	0.00E+00	0.00E+00	0.00E+00
6013	C13	0.00E+00	0.00E+00	0.00E+00	0.00E+00	0.00E+00	0.00E+00
6012	C12	0.00E+00	0.00E+00	0.00E+00	0.00E+00	0.00E+00	0.00E+00

Table 12 (continued). Radionuclide Inventories in Used Fuel

Nuclide Group	AGFR 75.3 GWd / tHM	AGFR 120 GWd / tHM	AGFR 75.3 GWd / tHM + 8 yr decay	AGFR 120 GWd / tHM + 8 yr decay	PWR 38.6 GWd / tHM + 22 yr decay	PWR 72 GWd / tHM + 8 yr decay
Total TRU	**3.20E+0**	**3.64E+0**	**8.45E-4**	**1.96E-03**	**5.57E-02**	**1.80E-01**
Total MA	**3.20E+0**	**3.64E+0**	**2.62E-6**	**8.89E-06**	**5.04E-03**	**3.62E-02**
Total Pu	**8.73E-4**	**2.19E-3**	**8.42E-4**	**1.95E-03**	**5.06E-02**	**1.44E-01**
Total Actinides	**6.60E+0**	**7.59E+0**	**8.49E-4**	**1.97E-03**	**5.57E-02**	**1.80E-01**
Total Non-Actinides	**2.00E-1**	**5.08E+0**	**1.68E-1**	**2.58E-01**	**2.20E-01**	**4.46E-01**
Total Activity	**6.80E+0**	**1.27E+1**	**1.69E-1**	**2.60E-01**	**2.75E-01**	**6.26E-01**

APPENDIX B

The purpose of this appendix is to explain the features of the AGFR spectrum that may appear to be anomalous or discontinuous. As stated in section 4.4, resonances in the cross section of Oxygen-16 cause depressions in the neutron energy spectrum within the reactor. Figure 39 gives clear evidence of this. This figure compares the AGFR spectrum to the total cross section of Oxygen-16 for neutron energies between 0.1 MeV and 10 MeV. The AGFR spectrum was obtained via a simulation using MCNP, while the Oxygen-16 cross section is taken from Evaluated Nuclear Data File (ENDF) version B-VII.0 as tabulated in the Java-based Nuclear Information System (JANIS)[62]. Notice that the prominent O-16 cross section resonance near 0.4 MeV causes the preferential removal of neutrons from the spectrum at precisely that same energy. Also, though not as well defined, resonances from approximately 1 MeV to 4 MeV cause depressions in the flux in that energy range.

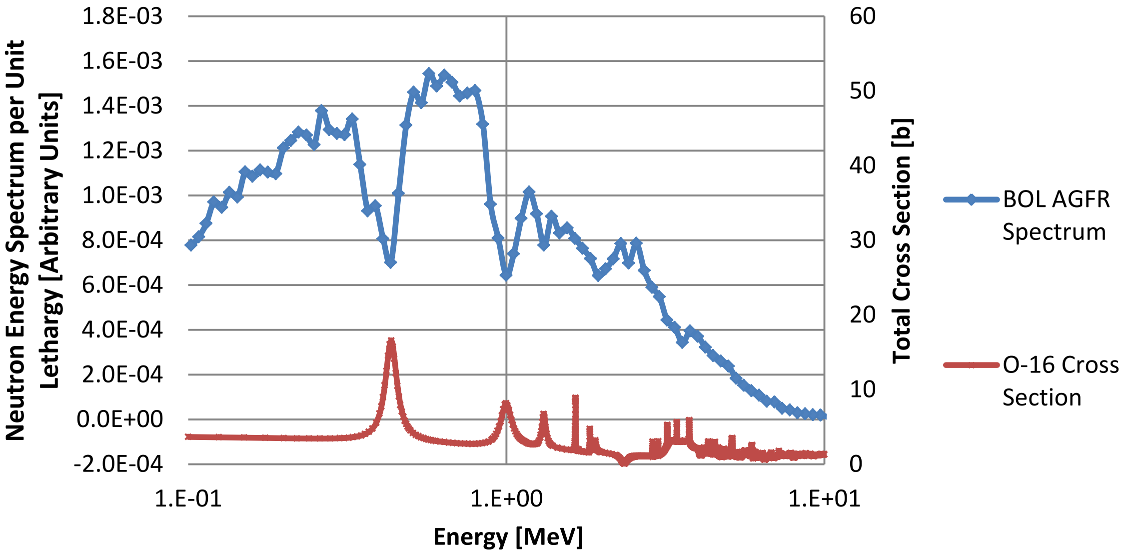

Figure 39. Correlation of O-16 resonances and AGFR spectral depressions.